DISSERTATION

THE INFLUENCE OF CLIMATE ON TERRESTRIAL CO2 FLUXES

Submitted by

Kevin Michael Schaefer

Department of Atmospheric Science

In partial fulfillment of the requirements

for the degree of Doctor of Philosophy

Colorado State University

Fort Collins, Colorado

Summer 2004

ProQuest Information and Learning Company
300 North Zeeb Road
P.O. Box 1346
Ann Arbor, MI 48106-1346

COLORADO STATE UNIVERSITY

June 1, 2004

WE HEREBY RECOMMEND THE DISSERTATION PREPARED UNDER OUR SUPERVISION BY KEVIN MICHAEL SCHAEFER ENTITLED THE INFLUENCE OF CLIMATE ON TERRESTRIAL CO2 FLUXES BE ACCEPTED AS FULFILLING IN PART REQUIREMENTS FOR THE DEGREE OF DOCTOR OF PHILOSOPHY.

Committee on Graduate Work

Advisor

Department Head

ABSTRACT OF DISSERTATION

THE INFLUENCE OF CLIMATE ON TERRESTRIAL CO_2 FLUXES

The concentration of CO_2 in the atmosphere ($[CO_2]$) is increasing at only about half the rate expected based on fossil fuel emissions. This "missing sink" is highly variable due primarily to the effects of climate variability on terrestrial CO_2 fluxes in the northern hemisphere. Using a series of model simulations, we studied how climate influences inter-annual variability and long-term trends in terrestrial CO_2 fluxes. We modeled Net Ecosystem Exchange (NEE) of CO_2 from 1958-2002 (45 years) using the Simple Biosphere model, Version 2 (SiB2). As input weather, we used the National Centers for Environmental Prediction (NCEP) reanalysis and the European Centre for Medium-range Weather Forecasts (ECMWF) Reanalysis. To define the Leaf Area Index, we used the Fourier-Adjustment, Solar zenith angle corrected, Interpolated Reconstructed (FASIR) Normalized Difference Vegetation Index (NDVI) dataset. We used correlations, trends, and other statistical techniques to isolate the relationships between NEE and climate.

The simulated NEE reproduces the salient features and magnitude of the measured global CO_2 growth rate. The northern hemisphere shows a pattern of alternating positive and negative NEE anomalies that cancel such that the tropics dominate the global simulated NEE inter-annual variability.

Climate influences on NEE have strong regional differences with precipitation dominating in the tropics and temperature in the extra-tropics. In tropical regions with drier soils, precipitation control of photosynthesis (i.e., drought stress) dominates. By contrast, in moist soils, precipitation control of respiration dominates. Due to

cancellation and competing effects, no single climate variable controls global or regional NEE inter-annual variability. Globally, precipitation accounts for 44% of NEE variability; followed by Leaf Area Index (23%), soil carbon (12%), and temperature (16%). The influence of ENSO is consistent with that expected for shifting precipitation patterns in the tropics.

The AO strongly influences autumn, winter, and spring NEE through its influence on temperature. Soil retains the AO temperature signal for many months, influencing respiration fluxes well into spring. Seasonally asymmetric NEE trends influence the seasonal amplitude of atmospheric CO_2 concentration. Positive AO polarity in winter advances the date of leaf out, increasing the spring drawdown of atmospheric CO_2. Positive AO polarity in winter increases temperature and respiration, increasing the winter buildup of atmospheric CO_2. The influence of the AO on summer NEE is minimal except for North America in August.

The trend in the winter AO partially explains observed trends towards warmer winters and earlier springs. The timing of spring correlates with the AO where the AO influences temperature (Eurasia and southeast United States). Modeled trends in leaf out, snowmelt, and soil thaw are consistent with observations. The AO shows a statistically significant influence on spring trends in the eastern United States and northern Europe. Seasonally asymmetric trends in NEE can partially explain the observed trend towards larger seasonal amplitudes in [CO_2]. The components of the land surface with climate memory (plant buds, snow pack, and soil temperature) integrate the noisy AO input over time to control the transition from winter to spring.

In summary, climatic memory is very important in the study of seasonal dynamics and that the winter AO influences the transition from winter to spring.

Kevin Michael Schaefer
Department of Atmospheric Science
Colorado State University
Fort Collins, CO 80523
Summer 2004

Acknowledgements

I would not have been able to complete this research and obtain an advanced degree without the love, support, and sacrifice of my wife, Susan Maroney. I thank my advisor Scott Denning for keeping me focused. I thank my committee members for their sound advice. I thank all the members of my research group, who at various times provided help, technical support, data, and encouragement as needed. We thank the National Oceanic and Atmospheric Administration, Climate Monitoring and Diagnostics Laboratory, Boulder, Colorado for supplying observations of CO_2 concentration. We thank David Thompson of the Atmospherics Sciences Department, Colorado State University for valuable advice and insight regarding our analysis of the Arctic Oscillation. Lastly, I thank my son Jason, who just doesn't care whether Dad has a graduate degree or not.

This research was funded by NASA under NASA Grant NCC5-621 Supplement 1, through the University of California at Berkeley under NASA grant SA2805-23941, through the University of California at Santa Barbara under NASA Cooperative Agreement NCC5-302, the Earth System Science Workbench (ESSW): a scalable infrastructure for Earth Science Information Partners (ESIPs). Partial funding was also provided through the Monfort Professor Award from CSU.

Table of Contents

1. Introduction

The observed atmospheric CO_2 growth rate over the past 50 years is only about half that expected based on fossil fuel emissions. Modeling, isotope, and inversion studies place much of this "missing sink" in the northern hemisphere terrestrial biosphere, but its spatial distribution and the mechanisms that drive it are not well known. Predicting future climate requires a deep understanding of how the atmospheric CO_2 concentration will respond under various climate change scenarios, which, in turn, requires an understanding of the mechanisms that drive the missing sink.

The atmospheric CO_2 growth rate shows a great deal of inter-annual variability [*Conway et al.,* 1994; *LLoyd*, 1999; *Rayner and Law*, 1999; *Tans and Wallace*, 1999; *Bousquet et al.,* 2000; *Fung*, 2000]. The ocean fluxes show relatively low variability [*Rayner and Law*, 1999; *Le Quéré et al.,* 2000], so the growth rate variability is attributed primarily to changes in the terrestrial sink [*Sarmiento*, 1993; *Conway et al.,* 1994; *Trolier et al.,* 1996; *Kaduk and Heimann*, 1997; *LLoyd*, 1999; *Houghton et al.,* 1998; *Tans and Wallace*, 1999; *Houghton*, 2000; *Prince et al.,* 2000]. Climate, land use change, natural disturbance, CO_2 fertilization, and nitrogen deposition also influence terrestrial CO_2 fluxes [*Conway et al.,* 1994; *Bousquet et al.,* 2000; *Fung*, 2000; *Houghton*, 2000], but climate contributes most to inter-annual variability [*Houghton*, 2000].

We need to understand how climate variability affects terrestrial CO_2 fluxes so that we can isolate the location and mechanisms behind the missing sink. In addition, the growth rate variability provides clues about how the biosphere might respond under various climate change scenarios. Studying how climate influences terrestrial CO_2 fluxes will allow us to test the performance of predictive models under various climate conditions. Lastly, we need accurate estimates of seasonal and inter-annual variability in CO_2 fluxes to serve as background for data assimilation and transport inversion studies designed to isolate the location and mechanisms behind the missing sink. Until we can successfully reproduce past variability in the missing sink, the uncertainty in predicting a future response will remain high.

Lacking direct measurements of net global CO_2 fluxes, the scientific community estimates net terrestrial fluxes from satellite data, inversions, and models. Satellite data, e.g., the Normalized Difference Vegetation Index (NDVI), is used to estimate the Leaf Area Index (LAI), which, in combination with a model, is used to estimate global net primary production [e.g., *Goetz et al.,* 2000 and *Ichii et al.,* 2001]. NDVI does not contain direct information about respiration, and so we cannot use it alone to estimate net terrestrial fluxes. Inversions can estimate net fluxes for large, continental scale regions, but cannot isolate the exact causes of variability [e.g., *Bousquet et al.,* 2000]. Terrestrial carbon models range from highly mechanistic biogeochemical process models to statistical regression and bookkeeping models. Biogeochemistry models track the amount of carbon in various biological pools [e.g., *Ichii et al.,* 2001], but vary widely in the number of pools and how explicitly they represent photosynthesis and respiration processes.

My research focused on how climate influences inter-annual variability net terrestrial CO_2 fluxes. We neglected the influence of CO_2 fertilization and nitrogen deposition because they show little inter-annual variability [*Houghton*, 2000]. CO_2 fertilization and nitrogen deposition probably influence long-term trends in the terrestrial carbon sink, but we are studying the inter-annual variability rather than the magnitude of the terrestrial sink. We also neglected variability due to fossil fuel emissions, which was small compared to other factors [*Houghton*, 2000]. Due to time constraints, we did not consider variability in ocean uptake. CO_2 fluxes resulting from land use change, such as deforestation, are spread over several years, resulting in a relatively low influence on inter-annual variability in terrestrial CO_2 fluxes [*Houghton*, 2000]. Variability of large-scale disturbances, such as fires, influences inter-annual variability in terrestrial CO_2 fluxes, but are also related to variability in climate [*Houghton*, 2000]. Although we did not explicitly isolate the effects of land use change and disturbances, we did not completely neglect them. The global NDVI dataset used as input to our model includes the effects of land use change and disturbances.

This dissertation is based on two papers written for journal publication. Chapter 2 (Methods) describes the models, data, and statistical techniques common to both papers. Chapter 3, *the effect of climate on inter-annual variability of terrestrial CO_2 fluxes*, has already been published [*Schaefer et al.*, 2002]. Chapter 4, *the winter Arctic Oscillation, the timing of spring, and carbon fluxes in the northern hemisphere*, will be submitted to Global Biogeochemical Cycles. Both chapters include descriptions of models and techniques unique to each paper.

I posed several specific hypotheses related to the relationship between climate and NEE and tested them against the model output using various statistical techniques. These long, global simulations (ranging from 1 to 45 years) can help answer many questions about the interaction between climate and terrestrial CO_2 fluxes. I focused on regional climate influences, with a strong emphasis on the northern hemisphere because that is the suspected location of the missing sink.

2. Hypotheses

Hypothesis 1: the climate influence on NEE has strong regional differences.

We hypothesize that climate influences on NEE have strong regional differences. Past studies suggest temperature and precipitation can explain NEE inter-annual variability, but disagree on the exact mechanism [e.g., *Kaduk and Heimann*, 1997; *LLoyd*, 1999; *Dickinson*, 2000; *Houghton*, 2000]. Respiration dominates flux inter-annual variability in some areas [*Houghton*, 2000] and photosynthesis in others [*Kaduk and Heimann*, 1997]. How available light and humidity influence inter-annual variability in CO_2 fluxes are not well known. To test our hypothesis, we will create specialized model diagnostics (described below) that will allow us to statistically quantify how strongly each climate factor influences NEE inter-annual variability.

Hypothesis 2: ENSO influences NEE in the tropics

We hypothesize that the El Niño-Southern Oscillation (ENSO) influences NEE in the tropics. ENSO is the dominant mode of climate variability in the tropical regions and should account for some of the inter-annual variability in NEE. To test our hypothesis, we will represent ENSO using the Southern Oscillation Index (SOI) based on the sea level pressure difference between Tahiti and Darwin. We will then use correlations and regressions to relate the ENSO to our modeled NEE, respiration, and GPP.

Hypothesis 3: the AO influences NEE in the high northern latitudes

The Arctic Oscillation (AO) is the dominant atmospheric circulation mode in the northern hemisphere in winter [*Thompson et al.,* 2000]. The AO is a zonally symmetric seesaw in atmospheric mass between the Arctic and mid-latitudes centered on 45N

[*Thompson and Wallace*, 2000]. Positive AO polarity has less mass and lower pressure in the Arctic and more mass and higher pressure at 45N. Positive AO polarity is characterized by westerly geostrophic surface winds along 55N latitude [*Thompson and Wallace*, 2001]. This geostrophic balance results in a north-south dipole in the strength of the zonal wind between 25°N and 60°N [*Thompson and Wallace*, 2000]. Positive AO polarity has stronger westerly winds (positive anomalies) north of 45°N and weaker winds (negative anomalies) south of 45°N [*Thompson and Wallace*, 2000; *Thompson and Wallace*, 2001]. The variance in zonal mean wind due to the AO peaks between 25-35N and 55-60N latitude [*Thompson and Wallace*, 2000]. The AO exists all year round, but is strongest and most variable in winter, when radiative cooling over the pole is greatest and the polar vortex is strongest. In March, the AO weakens as increased convection over land breaks down the polar vortex. Since the 1950s, the winter AO has tended towards positive polarity [*Thompson et al.,* 2000], indicating a gradual strengthening of the wintertime polar vortex [*Serreze et al.,* 2000].

To represent the AO, we used an index based on the first principle component of sea level pressure from the National Centers for Environmental Prediction (NCEP) reanalysis [*Thompson and Wallace*, 2000]. Because they are highly correlated, we will use this AO index to also represent the North Atlantic Oscillation (NAO). To visualize the influence of the AO on climate, we correlated the AO index and the NCEP surface air temperature and precipitation for winter and early spring (January-February-March or JFM) for 1958-2002 (Figure 1). Smoother zonal flow associated with positive AO polarity favors advection of warm, moist oceanic air deep into continental interiors, resulting in higher temperatures and increased precipitation [*Thompson and Wallace*, 2000]. Warm air advection reduces precipitation in Eurasia south of 55° N latitudes, resulting in negative precipitation correlations. Positive AO polarity also decreases the number of cold air outbreaks, resulting in positive temperature anomalies in central North America [*Thompson and Wallace*, 2001]. Alaska and Northeast Canada show negative temperature and precipitation correlations, consistent with cold, dry airflow from the Arctic expected for positive AO polarity [*Thompson and Wallace*, 2000]. The AO randomly switches polarity with a characteristic synoptic time scale of 7-10 days.

(a) Temperature

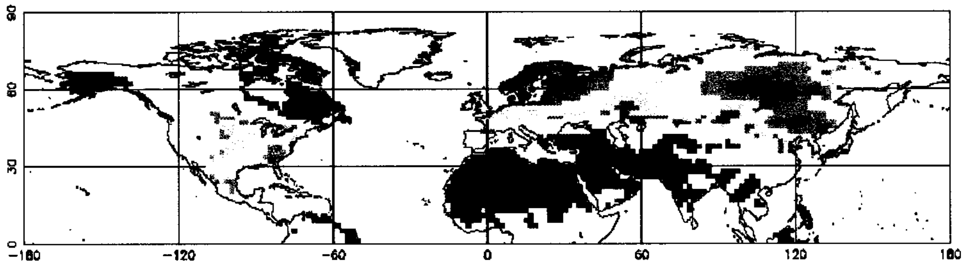

(b) Precipitation

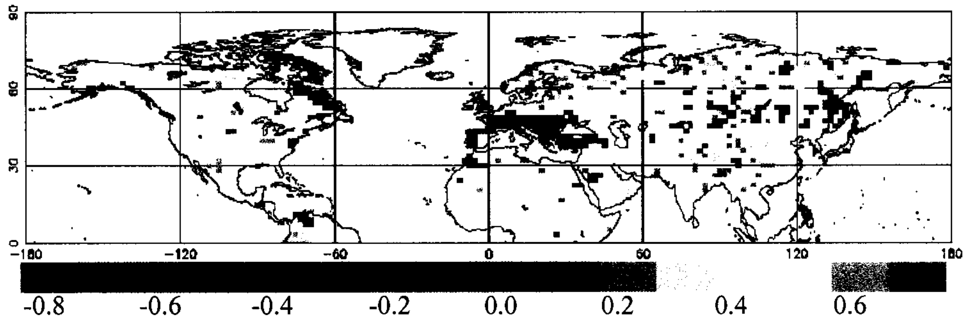

Figure 1. Advection of warm, moist oceanic air deep into continental interiors result in positive correlations for January-February-March (JFM) between the Arctic Oscillation (AO) index and surface air temperature (a) and precipitation (b) from the NCEP reanalysis. Correlations failing the T-test at 95% significance are omitted.

We hypothesize that the Arctic Oscillation (AO) influences NEE variability in the high northern latitudes. To test our hypothesis, we correlated and regressed the AO index to our modeled NEE, respiration, and GPP. We assessed the influence of the AO on NEE throughout the year, not just in winter when the AO is strongest. The AO influence on temperature is stronger than its influence on precipitation, so we expect to see increased respiration and GPP in those regions where the AO exerts the strongest influence on the surface air temperature.

Hypothesis 4: Climate memory allows the winter AO to influence spring NEE

We hypothesize that elements of the land surface have sufficient climate memory such that the winter AO influences variability in spring and early summer NEE. Climate memory occurs when a slowly changing land component integrates noisy, high frequency climate variability into a persistent, low frequency signal. The components of the land system with climate memory include the soil temperature, soil moisture, the snow, and the plants themselves.

To test our hypothesis, we correlated the winter (JFM) AO index with our modeled fluxes at various lag times. Since the AO most strongly influences temperature, we expect the soil to retain the winter AO temperature anomaly, influencing respiration fluxes into spring.

Hypothesis 5: the winter AO influences variability and trends in the timing of spring

We hypothesize that the winter AO, through its influence on temperature and precipitation, influences the timing of spring in the northern hemisphere. Those components of the land system with climate memory (soil temperature and moisture, snow, and plants) control the transition from winter to spring by integrating the noisy climate input throughout the winter. Events that typically mark the start of spring include snowmelt, soil thaw, and plant leaf out or flowering. Plant phenophases (i.e., climate driven growth or senescence events) mark the start and end of the growing season [*Schwartz and Reiter*, 2000; *Chen and Pan*, 2002].

The date of spring depends on the cumulative effects of climate over the entire winter. The date of snowmelt, for example, depends on snow depth, temperature, and cloud cover [*Dye*, 2002; *Stone et al.,* 2002]. Increased precipitation in winter (October-February) increases snow depth and delays snowmelt by increasing the total energy required for melting [*Cutforth et al.,* 1999; *Vaganov et al.,* 1999; *Stone et al.,* 2002]. Warmer temperatures in spring (March-May) advance snow melt by increasing melting and sublimation rates [*Stone et al.,* 2002]. Increased cloudiness in spring (March-May) advances snowmelt by enhancing cloud thermal forcing from absorbed downwelling longwave radiation [*Stone et al.,* 2002].

Past research has identified some regional relationships between the timing of spring and the NAO. The NAO negatively correlates with spring leafing and flowering (positive NAO means earlier spring), indicating the NAO influence on winter temperatures and precipitation influence spring phenology in Europe. Winter temperatures and the JFM NAO statistically explain most of the observed variability in spring phenophases in Europe [*D'Odorico et al.,* 2002; *Menzel*, 2003]. *D'Odorico et al.,* [2002] found that positive AO polarity in winter advanced ice breakup in European rivers and Lakes. However, we hypothesize that the winter AO influences the timing of spring throughout the northern hemisphere, not just in Europe.

Various observations over the last half of the 20th century indicate large-scale climatic trends towards warmer and earlier springs in the northern hemisphere [*Serreze et al.,* 2000]. Bud burst, leaf out, and other plant phenophases have occurred earlier in spring, also indicating a longer growing season [*Menzel and Fabian*, 1999; *Keyser et al.,* 2000; *Menzel*, 2000; *Menzel*, 2003]. Winter and spring temperatures have increased, spring snow depth and snow cover have decreased, and the date of snowmelt has advanced [*Serreze et al.,* 2000]. During the same time period, the AO has tended towards positive polarity during winter [*Thompson et al.,* 2000]. Although the AO pattern dominates the northern hemisphere [*Serreze et al.,* 2000], how the AO influences terrestrial carbon fluxes is unclear [*Reichenau and Esser*, 2003; *Schaefer et al.,* 2002].

Warmer temperatures in early spring have advanced observed leaf unfolding and flowering in Europe and North America since the 1950s [*Menzel and Fabian*, 1999; *Keyser et al.,* 2000; *Menzel*, 2000; *Schwartz and Reiter*, 2000; *Menzel*, 2003]. From 1959-1996 in Europe, the average growing season has increased by 10.8 days [*Menzel and Fabian*, 1999; *Menzel*, 2000]. Since early spring phenophases show the strongest trends, the longer growing seasons are due primarily to earlier starts in spring [*Menzel and Fabian*, 1999; *Menzel*, 2000]. Trends in autumn phenophases are not as clear, with some species advancing and others retreating, but overall show delays of 4.8 days in Europe [*Menzel and Fabian*, 1999; *Menzel*, 2000; *Menzel*, 2003]. The inconsistent autumn trends may result from conflicting temperature influences: higher spring and early summer temperatures advance leaf coloring while higher autumn temperatures delay leaf coloring [*Menzel*, 2003].

Since the 1950s, high latitude winter snow depths have declined and spring snow cover has decreased 10% [*Hartley and Robinson*, 2000; *Serreze et al.,* 2000; *Dye*, 2002; *Stone et al.,* 2002]. Also, the spring temperature and cloud cover have increased [*Stone et al.,* 2002], advancing the date of snowmelt [*Cutforth et al.,* 1999; *Zhou et al.,* 2001; *Dye*, 2002]. Based on station measurements and NOAA snow charts derived from visible reflectances, the Week of Last Snow in the northern hemisphere spring has advanced 9-

15 days and the snow free period has increased 9-19 days for 1972-2000, consistent with observed NDVI and [CO_2] amplitude trends [*Dye*, 2002]. The latitudes between 55-60 degrees show the strongest trends towards earlier snowmelt [*Dye*, 2002] while Siberia shows increased snow depth and delayed snowmelt [*Stone et al.*, 2002]. The spatial pattern of snowmelt trends resembles the AO [*Serreze et al.*, 2000]. The autumn trends are not as clear: NOAA snow charts do not show a strong trend in autumn snow cover [*Dye*, 2002] while station measurements in the U. S. Great Plains show increased autumn snow cover [*Hartley and Robinson*, 2000].

The global mean surface air temperature has risen 0.3-0.6° C since 1960 with largest increases in central Eurasia and Alaska [*Cutforth et al.*, 1999; *Barber et al.*, 2000; *Serreze et al.*, 2000; *Schwartz and Reiter*, 2000; *Shabanov et al.*, 2002]. The temperature trends are widespread, but not universal, with decreases in northeast Canada [*Serreze et al.*, 2000]. Winter, spring, and early summer show the greatest temperature increases, resulting in earlier leaf out and longer growing seasons [*Myneni et al.*, 1997; *Randerson et al.*, 1999; *Vaganov et al.*, 1999; *Barber et al.*, 2000; *Hartley and Robinson*, 2000; *Serreze et al.*, 2000; *Zhou et al.*, 2001; *Robeson*, 2002; *Zhou et al.*, 2003]. Autumn temperature trends are ambiguous: some studies show increases [*Myneni et al.*, 1997; *Randerson et al.*, 1999; *Zhou et al.*, 2001, 2003], some show decreases [*Hartley and Robinson*, 2000; *Schwartz and Reiter*, 2000], and others show no clear trend at all [*Serreze et al.*, 2000].

We hypothesize that the observed trends in the winter AO can help explain the observed trends towards earlier leaf out and snowmelt over large areas in the northern hemisphere. At mid to high northern latitudes, the AO statistically explains 31% of the winter temperature variance [*Serreze et al.,* 2000] and about 40% of the winter temperature trends [*Thompson et al.,* 2000]. Leaf out, snowmelt, and soil thaw all depend on the integrated temperature over the entire winter. If the winter AO trend explains the winter temperature trends, it should also explain the trends towards earlier springs in the northern hemisphere.

To test our hypothesis, we modeled the dates of leaf out, snowmelt, and soil thaw and correlated them with average JFM AO index. We expect that positive AO polarity in winter results in a positive temperature anomaly and an earlier spring, resulting negative correlations between the winter AO and the date of spring. Time constraints limited our analysis to spring events only. We then estimated trends in the date of leaf out, snowmelt, and soil thaw and, using correlations with the winter AO index, calculated the fraction of these trends that are linearly congruent to the AO trend. We expect the AO to statistically explain a significant fraction of the modeled trends in the date of spring in those regions where the AO exerts the strongest influence on temperature.

Hypothesis 6: The winter AO influences variability and trends in the [CO_2] seasonal amplitude

The seasonal variability in observed carbon dioxide concentrations ([CO_2]) is driven by plant growth in the Northern Hemisphere, dropping in spring and summer when plant growth peaks and increasing in autumn and winter when plant growth tapers off [*Keeling et al.,* 1996; *Wu and Lynch*, 2000]. Figure 2 shows the observed seasonal cycle for [CO_2] at Barrow, Alaska (71.3N) and Mauna Loa, Hawaii (19.5N) derived from continuous measurements of [CO_2] with the long-term trend removed [*Conway et al.,* 1994]. The seasonal variability in NEE drives [CO_2]. When NEE is negative in late spring and early summer, [CO_2] decreases as GPP draws CO_2 out of the atmosphere.

[CO_2] increases the rest of the year when NEE is positive and respiration puts CO_2 back into the atmosphere. The minimum [CO_2] occurs in summer and the maximum [CO_2] in late winter or early spring. The [CO_2] seasonal amplitude (defined as annual maximum minus minimum) is 15-20 ppm at high northern latitudes, decreasing to 3 ppm near the equator [*Keeling et al.,* 1996; *Wu and Lynch,* 2000].

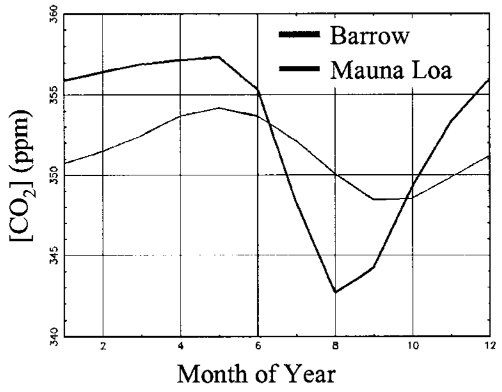

Figure 2. The observed seasonal cycles in atmospheric CO_2 concentration ([CO_2]) at Barrow, Alaska and Mauna Loa, Hawaii increase in winter due to respiration and decrease in spring due to GPP.

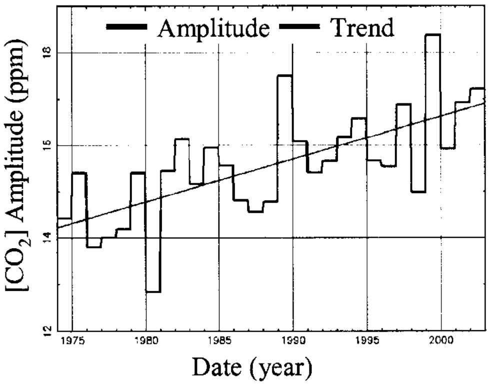

Figure 3. The observed amplitude of the [CO_2] seasonal cycle at Barrow, Alaska (annual maximum minus minimum) shows a statistically significant positive trend.

Since the 1960s, the [CO_2] seasonal amplitude has increased 20% in Hawaii and 40% in the arctic [*Keeling et al.,* 1995; *Keeling et al.,* 1996; *Randerson et al.,* 1999]. The phasing of the [CO_2] seasonal cycle has also advanced seven days globally, indicating an earlier spring [*Keeling et al.,* 1995; *Keeling et al.,* 1996]. Figure 3 illustrates the observed increase in the amplitude of the [CO_2] seasonal cycle as a function of time for Barrow, Alaska with the long-term trend removed [*Conway et al.,* 1994]. Correlations between temperature and regional net carbon flux (obtained by inverting flask measurements with a transport model) indicate enhanced late spring and early summer photosynthesis best reproduces the observed trend in [CO_2] amplitude [*Randerson et al.,* 1999].

Seasonally asymmetric trends in surface CO_2 fluxes can increase the $[CO_2]$ seasonal amplitude. Seasonally asymmetric trends are tendencies that are stronger or even of opposite sign at different times of the year. For example, warmer winters could increase winter respiration [*Zimov et al.,* 1996; *Wu and Lynch*, 2000]. Changes in the timing of peak photosynthesis and respiration rates could change the $[CO_2]$ amplitude even though the annual net annual carbon exchange may not change [*Idso et al.,* 1999; *Wu and Lynch*, 2000; *Lucht et al.,* 2002; *Nemani et al.,* 2002]. Advanced snowmelt in spring could advance peak photosynthesis in early summer [*Chapin et al.,* 1996; *Stone et al.,* 2002]. Lastly, changes in seasonal patterns of atmospheric circulation may shift the source regions observed by flask stations, resulting in a trend in the observed $[CO_2]$ amplitude [*Dargaville et al.,* 2000; *Higuchi et al.,* 2002].

We hypothesize that the winter AO influences inter-annual variability in the $[CO_2]$ seasonal amplitude. Increased winter temperatures for positive AO polarity would increase respiration over a large enough area to affect the buildup of $[CO_2]$ in winter. If the winter AO influences the timing of spring over a large enough area, then it also influences the start of the growing season and the total GPP during spring and early summer, which, in turn, would influence the seasonal drawdown of $[CO_2]$. A positive AO polarity in winter would then simultaneously increase winter build up and spring drawdown.

We also hypothesize that the observed trend towards larger $[CO_2]$ seasonal amplitudes is related to the trend towards positive AO polarity in winter. The trend towards positive AO polarity in winter could produce seasonally asymmetric trends in NEE that might explain the observed trends towards increased $[CO_2]$ amplitude. Trends towards increased GPP in spring would amplify the draw down, resulting in a lower minimum [CO_2]. Likewise, trends towards increased respiration at other times of the year would amplify the [CO_2] buildup, resulting in a higher maximum [CO_2]. Increases in GPP and respiration that occur at the same time tend to cancel each other with no influence on [CO_2] amplitude.

To test our hypotheses, we will correlate the winter respiration and the total spring GPP to the winter AO index. We expect to see positive correlation with winter respiration and with total spring GPP. We will then identify those latitudes that show seasonally asymmetric trends. We will then use correlations with the winter AO and calculate the fraction of these trends that are linearly congruent to the AO trend. We expect to see trends towards increased respiration in winter and increased GPP in spring.

Hypothesis 7: The winter AO trend is related to NDVI trends

NDVI datasets for 1982-2000 with various corrections all show statistically significant positive trends in the northern hemisphere, indicating earlier greening, later falls, and lengthening growing seasons [*Myneni et al.,* 1997; *Los et al.,* 2001; *Tucker et al.,* 2001; *Zhou et al.,* 2001; *Hicke et al.,* 2002a, 2002b; *Shabanov et al.,* 2002; *Slayback et al.,* 2003; *Zhou et al.,* 2003]. The exception is one NDVI dataset that did not correct for sensor drift and calibration [*Slayback et al.,* 2003]. The greatest increases occur in Eurasian boreal zones in March, April, and May. Warming in spring and fall statistically explain the largest fraction of the greening trend [*Tucker et al.,* 2001; *Nemani et al.,* 2002; *Zhou et al.,* 2001; *Slayback et al.,* 2003; *Zhou et al.,* 2003]. The spring NDVI positively correlates with the winter NAO [*Los et al.,* 2001].

Interpretation of the NDVI trends is difficult. Based on individual band reflectances and a radiative transfer model, the increased NDVI in spring can be explained by darker soils from decreased snow cover [*Shabanov et al.,* 2002], which would mask relationships between NDVI and plant phenophases [*Chen and Pan*, 2002]. Also, the monthly or bi-monthly NDVI time resolution is too coarse to detect trends in plant phenophases and the record too short to form strong conclusions [*White et al.,* 1997; *Serreze et al.,* 2000; *Zhou et al.,* 2001; *Chen and Pan*, 2002]. Nevertheless, the NDVI trends are consistent with increasing photosynthetic activity in spring and summer and with the observed increase in the [CO_2] seasonal amplitude [*Ichii et al.,* 2001; *Shabanov et al.,* 2002; *Slayback et al.,* 2003].

We hypothesize that observed trends towards brighter NDVI is related to the trends towards positive AO polarity in winter. If the winter AO trend has advanced the date of spring, then the longer growing season should results in brighter NDVI. To test our hypothesis, we will correlate the winter AO to spring NDVI and calculate the fraction of these trends that are linearly congruent to the AO trend.

3. Methods

3.1 General

To test our various hypotheses, we modeled photosynthesis, respiration, spring phenology, snowmelt, soil thaw, and many other variables using the Simple Biosphere model, Version 2 (SiB2) [*Sellers et al.,* 1996a]. SiB2 is a biophysical model, which means it estimates the biological processes of photosynthesis and respiration and the physical processes of turbulent transport between the land surface and the boundary layer. Biophysical models, such as SiB2, were created to estimate surface fluxes of latent heat, sensible heat, and momentum in General Circulation Models [*Sellers et al.,* 1994; *Sellers et al.,* 1997; *Los*, 1998]. We employed SiB2 in an 'off-line' mode, where we input weather generated by various General Circulation Models to estimate fluxes of latent heat, sensible heat, and, of course, carbon.

SiB2 is a good choice for this type of modeling study. SiB2 produces realistic CO_2 surface fluxes [*Denning et al.,* 1996a; *Baker et al.,* 2003] and, when coupled to a transport model, realistic atmospheric CO_2 concentrations [*Denning et al.,* 1996b]. SiB2 produces realistic surface energy and carbon fluxes at a variety of spatial scales: a single point [*Baker et al.,* 2003], in a mesoscale model [*Denning et al.,* 2003], and a GCM [*Denning et al.,* 1995]. SiB2 has high time resolution and detailed plant physiology to isolate the influences of climate at multiple temporal scales. A highly mechanistic model like SiB2 driven by realistic weather allows us to identify and quantify exactly how climate influences terrestrial CO_2 fluxes.

SiB2 calculates leaf level photosynthesis based on enzyme kinetics and electron transport [*Farquhar et al.,* 1980] with a 10-min time step using the Ball-Berry-Collatz stomatal conductance model [*Ball*, 1988; *Collatz et al.*, 1991, 1992]. The leaf-level photosynthesis is scaled to the canopy level based on satellite imagery [*Sellers et al.*, 1996a]. SiB2 is balanced, which means respiration balances photosynthesis on an annual time scale using the model of *Denning et al.*, [1996] as modified by *Schaefer et al.*, [2002]. SiB2 has 1 canopy layer, which includes the canopy air and the canopy itself [*Sellers et al.*, 1996a]. SiB2 accounts for the effects of snow cover, rainfall interception by the canopy, and aerodynamic turbulence [*Sellers et al.*, 1996a]. SiB2 tracks 12 prognostic variables [*Sellers et al.*, 1994; *Sellers et al.*, 1996a]: canopy, surface, and deep soil temperature; canopy and surface water interception stores; canopy and surface ice/snow interception stores; canopy air space CO_2 concentration, soil moisture; and canopy conductance.

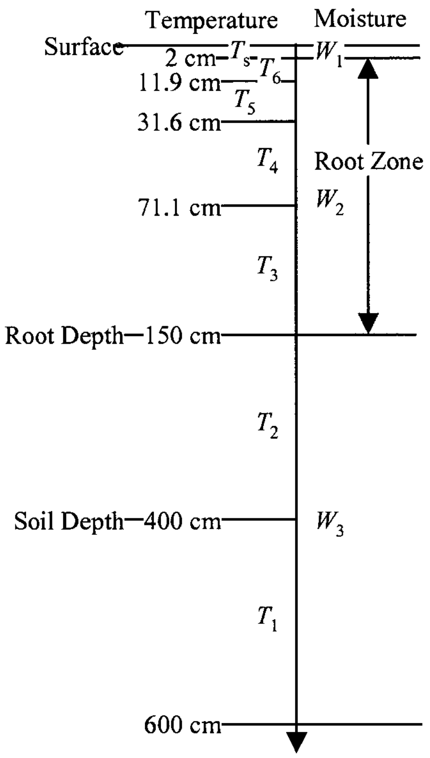

Figure 4. The SiB2 soil model tracks soil temperature and moisture. Root and soil depth are biome specific (typical values shown here).

SiB2 has 3 soil layers for soil moisture (surface layer, root zone, recharge zone) [*Sellers et al.*, 1996a] and seven layers for soil temperature (Figure 4). The soil temperature and moisture layers increase in thickness with depth. Soil hydraulic properties depend on soil texture [*Bonan*, 1996]. Soil thermal properties depend on soil texture and moisture [*Bonan*, 1996] and are recalculated each time step. Input soil texture maps (percent sand, silt, and clay) were interpolated from the International Global Biosphere Program

(IGBP) soil core database. The soil and root depths are biome specific parameters from *Sellers et al.,* [1996b].

3.2 SiB Input

As input, SiB2 requires weather data, NDVI, vegetation cover fraction, vegetation type, and soil type. *Sellers et al.,* [1994, 1996b] describes in detail the vegetation and soil characteristics. We used the *DeFries and Townshend* [1994] global map of 11 vegetation types.

As input weather data, we used either the European Centre for Medium-range Weather Forecasts (ECMWF) Reanalysis [*Gibson et al.,* 1999] or the National Centers for Environmental Prediction (NCEP) reanalysis. The ECMWF reanalysis covers 1978-1993 on a global, 1° by 1° grid. The NCEP reanalysis covers 1958-2002 on a Gaussian, 1.875° by 1.904° grid. Both contain surface temperature, pressure, wind speed, precipitation, visible light, and IR radiation data every 6 hours. Except for visible light, we linearly interpolated between data points to match the 10-minute SiB2 time step. The visible light was scaled by the cosine of the solar zenith angle to conserve energy and assure no light falls on the canopy at night.

The modeled GPP depends on the Leaf Area Index (LAI) estimated from monthly composite maps of NDVI. The monthly composite maps contain the maximum observed NDVI values during the month for each pixel on a 1° by 1° grid from 1982-1998. The NDVI was adjusted for missing data, satellite orbit drift, differing instrument calibrations, sensor degradation, and volcanic aerosols. We used the Fourier-Adjustment, Solar zenith angle corrected, Interpolated Reconstructed (FASIR) NDVI dataset, version 3.04b [*Sellers et al.,* 1994; *Los*, 1998; *Los et al.,* 2000]. Daily values of NDVI are interpolated from monthly composite values, which are arbitrarily assigned to the middle of the month (the actual observation time can be anytime in the month and different for each pixel).

To use the NCEP reanalysis data, we converted the NDVI, biome type, soil type, and other input maps from a 1x1° grid to the NCEP 1.875x 1.904° grid. We used area averaging to convert the FASIR NDVI data, the fraction of vegetation cover map, and the soil texture maps. Area averaging is not appropriate for maps of biome type (the average of biome types 1 and 2 is not 1.5), so we used nearest neighbor technique. The nearest neighbor technique assigns a grid cell on the 1.875x 1.904° grid with the value of the grid cell on the 1x1 grid whose center was nearest the 1.875x 1.904° grid cell center. Each map also used slightly different land masks, so we also used nearest neighbor to fill in missing pixels that did not match the NCEP land mask.

Los et al., [2000] assumed the vegetation cover fraction, f_V, was proportional to the absorbed fraction of photo-synthetically active radiation (*fPAR*):

$$(1) \qquad f_V = \frac{fPAR_{peak}}{fPAR_{\max}} ,$$

where $fPAR_{peak}$ is the observed maximum value of for each grid cell over a specified time period and $fPAR_{\max} = 0.95$ is the theoretical maximum value of *fPAR* [*Sellers et al.,* 1994; *Los*, 1998; *Los et al.,* 2000; *Oleson et al.,* 2000]. We estimated *fPAR* using an average between the simple ratio and NDVI methods [*Los et al.,* 2000]. *Los et al.,* [2000] used annual $fPAR_{peak}$, which varies year-to-year, causing abrupt changes in f_V each January. Using an average $fPAR_{peak}$ for the entire 17-year NDVI record artificially dampens *fPAR* variability in those years exceeding the average. We assumed f_V was constant and used $fPAR_{peak}$ for the entire time period.

3.3 GPP and Respiration in SiB2

General

SiB2 defines NEE as

$$(2) \qquad NEE = R - GPP,$$

where R is ecosystem respiration and GPP is gross primary production (i.e., canopy photosynthesis rate). Photosynthesis removes CO_2 from the atmosphere and respiration returns CO_2 to the atmosphere. A positive NEE indicates a net CO_2 flux into the atmosphere. Breaking R into autotrophic and heterotrophic respiration gives

$$(3) \qquad NEE = R_H + R_R + R_C - GPP,$$

where R_H is heterotrophic respiration, R_R is root autotrophic respiration, and R_C is canopy autotrophic respiration. Heterotrophic respiration is the decay of organic material by microorganisms. Autotrophic respiration is the release of CO_2 during plant maintenance and growth. Defining ground respiration as $R_g = R_H + R_R$ and canopy net assimilation as $A_n = GPP - R_C$, which gives an alternative definition of NEE [*Sellers et al.,* 1996a; *Denning et al.,* 1996a]:

$$(4) \qquad NEE = R_g - A_n.$$

To calculate A_n, SiB2 iterates the CO_2 partial pressure inside the leaf chloroplasts to minimize the difference between an enzyme kinetic and a stomatal conductance photosynthetic model. An enzyme kinetic model estimates A_n based on the chemical reactions of photosynthesis. A stomatal conductance model estimates A_n based on the flow of water and CO_2 into and out of the leaf stomata. The enzyme kinetics model is a "bottom-up" or "inside-out" approach to calculating photosynthesis and the stomatal conductance model is a "top-down" or "outside-in" approach. SiB2 uses the *Farquhar et* *al.,* [1980] enzyme kinetics model and the Ball-Berry-Collatz stomatal conductance model [*Ball*, 1988; *Collatz et al.,* 1991; 1992]. Both models are semi-empirical, meaning both combine theory with empirical relationships based on observations and both give reasonable results. SiB2 assumes the best estimate of GPP is one that minimizes the difference between the top-down and bottom-up models.

Photosynthesis from Enzyme Kinetics

The enzyme kinetics photosynthesis model in SiB assumes that the most limiting resource determines the canopy photosynthesis rate [*Denning et al.,* 1996a; *Sellers et al.,* 1996a; *Sellers et al.,* 1997]:

$$(5) \qquad GPP = Min(W_C, W_E, W_S)$$

where GPP is the canopy Gross Primary Production (mole m^{-2} s^{-1}), W_C is the Rubisco (leaf enzyme or nitrogen) limited rate, and W_E is light limited rate. For C_3 plants, W_S is the carbon compound export limited rate. For C_4 plants, W_S is the PEP-Carboxylase limited rate. The transition between limiting rates is coupled and smooth, not abrupt. To smooth the transition between limiting rates, SiB solves for the smallest roots of two quadratic equations [*Sellers et al.,* 1996a]:

$$(6) \qquad \begin{aligned} \beta_P W_P^2 - W_P(W_C + W_E) + W_E W_C &= 0 \\ \beta_A GPP^2 - GPP(W_P + W_S) + W_P W_S &= 0, \end{aligned}$$

where W_P is the smoothed minimum of Rubisco and export limited rates, and β_P and β_A are coupling coefficients. The coefficients β_P and β_A can range from 1 (no coupling) to 0 (geometric coupling). SiB assumes weak coupling with values that range from 0.8 to 0.98.

Rubisco limited photosynthetic rate

The Rubisco limited canopy photosynthetic rate, W_C, depends on the leaf's enzyme or nitrogen reserves and measures the biochemical processing capacity of the leaf [*Sellers et al.,* 1996a; *Sellers et al.,* 1997]:

$$(7) \qquad W_C = V_{\max 0} S_T S_w S_{PR} \Pi ,$$

where V_{max0} is the unstressed Rubisco catalytic capacity at canopy top, S_T is a canopy temperature scaling factor, S_w is a soil moisture scaling factor, S_{PR} is a photorespiration scaling factor, and Π is the PAR use parameter. Π scales W_C from a single leaf to the entire canopy (see below).

The chemical reactions in photosynthesis generally slow down at extreme high or low temperatures, represented by high and low temperature inhibition functions [*Sellers et al.,* 1996a]. For C3 plants [*Sellers et al.,* 1996a],

$$(8) \qquad S_T = \frac{2.1^{Q_T}}{1 + \exp(S_{HTI}(T_c - T_{HHTI}))},$$

where S_T is the temperature scaling factor, S_{HTI} is the slope of the high temperature inhibition function, T_{HHTI} is the half point temperature for the high temperature inhibition function, Q_T is the temperature response exponent, and T_c is canopy temperature. For C4 plants [*Sellers et al.,* 1996a],

$$(9) \qquad S_T = \frac{2.1^{Q_T}}{[1 + \exp(S_{HTI}(T_c - T_{HHTI}))][1 + \exp(S_{LTI}(T_{HLTI} - T_c))]},$$

where S_{LTI} is the slope of the low temperature inhibition function and T_{HLTI} the half point temperature of the low temperature inhibition function. Note that *Sellers et al.,* [1996a] shows 2.0 rather than 2.1 for both the C_3 and C_4 temperature response functions. Q_T, the temperature response or "Q10" exponent, is defined as

$$(10) \quad Q_T = (T_c - T_{rop})/10,$$

where T_{rop} is the reference or optimal temperature (typically 298.16 K).

Photorespiration is the production of CO_2 by oxidation of Rubisco with O_2 (both CO_2 and O_2 can react with Rubisco). S_{PR} measures the net competition between photorespiration and photosynthesis. For C_3 plants [*Sellers et al.,* 1996a]:

$$(11) \quad S_{PR} = \frac{c_i - \Gamma^*}{c_i + K_c\left(1 + O_2 / K_o\right)},$$

where c_i is partial pressure of CO_2 inside the chloroplasts, O_2 is the oxygen partial pressure inside chloroplasts, K_c is the Michaelis-Menten constant for CO_2 (Pa), K_o is the inhibition constant for O_2 (Pa), and Γ^* is the CO_2 compensation point (Pa). At the CO_2 compensation point, photorespiration equals photosynthesis. C_4 plants pump up c_i, greatly reducing photorespiration, so $S_{PR} = 1.0$. Empirical formulas show how Γ^*, K_c, and K_o vary with T_c:

$$(12) \quad \Gamma^* = 0.5\frac{O_2}{S} \quad S = 2600 \times 0.57^{Q_T} \quad K_o = 30{,}000 \times 1.2^{Q_T} \quad Kc = 30 \times 2.1^{Q_T}$$

where S is Rubisco specificity for CO_2 relative to O_2 and Q_T is the temperature scaling exponent.

PAR Limited photosynthetic rate

The canopy PAR limited photosynthesis rate, W_E, depends on the amount of visible light absorbed by green leaves [*Sellers et al.,* 1996a; *Sellers et al.,* 1997]:

$$(13) \quad W_E = PFDS_{PAR}\Pi,$$

where *PFD* is photon flux density, S_{PAR} is the PAR use efficiency, and Π is the PAR use parameter. The PFD is the flux of photons normal to the leaf surface [*Sellers et al.,* 1996a]:

$$(14) \quad PFD = xI_{top}\frac{G(\mu)}{\mu}\alpha_g ,$$

where x is a conversion factor (mole Joules^{-1}), I_{top} is the PAR intensity incident on the top of the canopy (W m^{-2}), μ is the cosine of the solar zenith angle, $G(\mu)$ is the leaf area projection in the μ direction, and α_g is the absorptance of green leaves. As with W_C, the conversion of light energy into photosynthetic products depends on the competing reactions of CO_2 and O_2 with Rubisco. S_{PAR} scales W_e to account for this competition. For C_3 plants, S_{PAR} is [*Sellers et al.,* 1996a]

$$(15) \quad S_{PAR} = \varepsilon_3\left[\frac{c_i - \Gamma^*}{c_i + 2\Gamma^*}\right],$$

and for C_4 plants, S_{PAR} is [*Sellers et al.,* 1996a]

$$(16) \quad S_{PAR} = \varepsilon_4$$

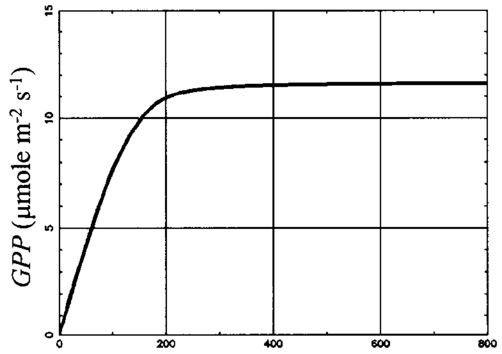

Figure 5. The simulated GPP quickly approaches a maximum value with increasing PAR because the canopy absorbs more light than it can use for photosynthesis.

where ε_3 and ε_4 are quantum efficiencies for CO_2 uptake by C_3 and C_4 plants (mole mole^{-1} for C_3, mole J^{-1} for C4) and Γ* is the CO_2 compensation point (Pa). SiB2 assumes the same quantum efficiency for C_3 and C_4 plants.

W_E controls the simulated GPP only in low light levels, as indicated in Figure 5. W_S or W_C limits GPP at higher light levels. The canopy typically absorbs more light than it can use for photosynthesis, so GPP quickly approaches a maximum value with increasing PAR.

Export or CO₂ limited photosynthetic rate

For C₃ plants, the export of photosynthetic products out of the chloroplast ties up Rubisco and can limit the assimilation rate. For C4 plants, the available CO₂ can limit the photosynthetic rate. The export limited assimilation rate, W_S, is defined as [*Sellers et al.,* 1996a; *Sellers et al.,* 1997]

$$(17) \quad W_S = V_{\max o} S_{Tex} S_w S_{EX} \Pi$$

where S_{EX} is a leaf export scaling factor and S_{Tex} is aan export temperature scaling factor. For C₃ plants, SiB assumes half of the Rubisco is tied up in the generation of photosynthetic products, so $S_{EX} = 1/2$ [*Sellers et al.,* 1996a]. For C₄ plants, S_{EX} depends on the partial pressure of CO₂ in the chloroplast [*Sellers et al.,* 1996a]:

$$(18) \quad S_{EX} = 2x10^4 \frac{C_i}{p},$$

where C_i is the partial pressure of CO₂ in the chloroplast (Pa) and p is atmospheric pressure (Pa).

The export rate generally slows down at extreme high or low temperatures [*Sellers et al.,* 1996a]. SiB represents this as high and low temperature inhibition functions. For C3 plants [*Sellers et al.,* 1996a],

$$(19) \quad S_{Tex} = \frac{1.8^{Q_T}}{1 + \exp(S_{HTI}(T_c - T_{HHTI}))},$$

where S_{Tex} is the export temperature scaling factor, S_{HTI} is the slope of the high temperature inhibition function, T_{HHTI} is the half point temperature for the high temperature inhibition function, Q_T is the temperature response exponent, and T_c is canopy temperature. For C4 plants [*Sellers et al.,* 1996a],

$$(20)\quad S_{Tex} = \frac{1.8^{Q_T}}{[1+\exp(S_{HTI}(T_c - T_{HHTI})][1+\exp(S_{LTI}(T_{HLTI} - T_c)]},$$

where S_{LTI} is the slope of the low temperature inhibition function and T_{HLTI} the half point temperature of the low temperature inhibition function. Note that *Sellers et al.,* [1996a] shows 2.0 rather than 1.8 for both the C_3 and C_4 temperature response functions. Q_T, the temperature response exponent, is defined above.

Canopy Autotrophic Respiration

The canopy autotrophic respiration rate, R_c, depends on the carboxylase content:

$$(21)\quad R_c = S_d V_{\max 0} S_w S_{rsp} \Pi,$$

where S_d is an empirical scaling constant (0.015 for C_3 plants and 0.025 for C_4 plants), V_{max0} is the unstressed Rubisco catalytic capacity at canopy top, S_w is a soil moisture scaling factor, S_{rsp} is a temperature scaling factor, and Π is the PAR use parameter [*Sellers et al.,* 1996a]. Like photosynthesis itself, the conversion of photosynthetic products slows down at extreme temperatures. S_{rsp} accounts for this temperature dependence and is defined as

$$(22)\quad S_{rsp} = \frac{2^{Q_T}}{1+\exp(S_{RD}(T_c - T_{RD})},$$

where S_{RD} is the slope of the temperature inhibition function and T_{RDI} the half point temperature of the temperature inhibition function, and T_c is the canopy temperature [*Sellers et al.,* 1996a]. Q_T is defined above.

GPP and Temperature

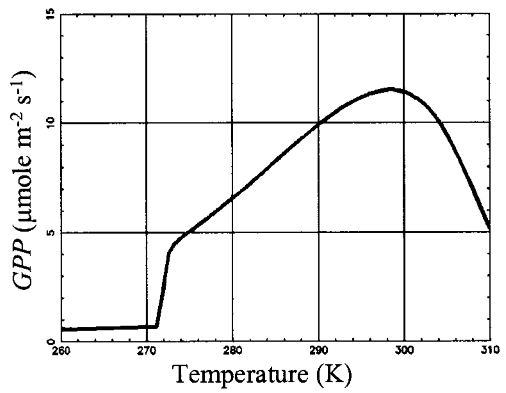

Figure 6. The simulated GPP effectively shuts down below freezing temperatures or at extreme high temperatures.

As illustrated in Figure 6, the simulated GPP shuts down at extreme high and low temperatures, indicating the effects of temperature on GPP are not as complicated as they might appear in the above equations for W_C, W_E, and W_S. When the ground is frozen, the plants cannot extract water from the soil, so GPP shuts down below about 272 K. At high temperatures, photorespiration becomes strong and GPP declines. This results in an optimal temperature for GPP. About this optimal temperature, GPP is relatively insensitive to changes in temperature.

The PAR Use Parameter

The PAR use parameter, Π, scales the *Farquhar et al.,* [1980] model for the photosynthetic rate of a single leaf to an entire canopy [*Sellers et al.,* 1994; *Sellers et al.,* 1996a; *Sellers et al.,* 1997; *Los*, 1998]. Π is the ratio of GPP at the canopy top to the GPP for the entire canopy

$$(23)\quad \Pi \equiv \frac{A}{A_{top}},$$

where A is the GPP of the entire canopy and A_{top} is the GPP at the canopy top [*Sellers et al.,* 1996a].

Photosynthesis, and thus Π, depends on the distribution of nitrogen within the canopy. Plants distribute the available nitrogen (e.g., Rubisco) to make the most of available light for photosynthesis. SiB2 assumes that catalytic capacity of Rubisco at any point within the canopy is proportional to average intensity of Photosynthetically Active Radiation (PAR):

$$(24)\quad \frac{dA}{dL} \propto I(L),$$

where L is the cumulative LAI from the canopy top and $I(L)$ is the relative intensity of PAR as a function of L. Separating terms and integrating from the canopy top gives us the total GPP for the canopy:

$$(25)\quad \int_0^{LAI} dA = A \propto \int_0^{LAI} I(L) dL,$$

where LAI is the total leaf area index. Dividing by the GPP at the canopy top gives us an expression for P (assuming $A_{top} \propto I_{top}$):

$$(26)\quad \frac{A}{A_{top}} = \Pi = \frac{1}{I_{top}} \int_0^{LAI} I(L) dL,$$

where I_{top} is the PAR intensity incident on the top of the canopy.

SiB assumes the average PAR intensity, $I(L)$, decreases exponentially downward from the canopy top according to Beer's law such that

$$(27)\quad \Pi = \frac{1}{I_{top}} \int_0^{LAI} I_{top} G \exp\left[-k_{ext} \frac{G(\mu)}{\mu} \frac{L}{f_V} \right] dL,$$

where G is the greenness fraction, k_{ext} is the extinction coefficient of PAR in the canopy, μ is the cosine of the solar zenith angle, $G(\mu)$ is the time averaged leaf area projection in the μ direction, and f_V is the fraction of vegetation cover. Canceling I_{top} and integrating from 0 to LAI gives

$$(28)\quad \Pi = \frac{f_V G\left(1-\exp\left[-k_{ext}\frac{G(\mu)}{\mu}\frac{LAI}{f_V}\right]\right)}{k_{ext}\,G(\mu)/\mu}.$$

Noting that the numerator is f_{PAR}, the fraction of PAR absorbed by green leaves within the canopy, and the denominator is k, the time–mean, radiation weighted PAR extinction coefficient [*Sellers et al.,* 1996a], gives

$$(29)\quad \Pi = \frac{f_{PAR}}{k}.$$

Π is effectively a remotely sensed measure of the vegetative state of the canopy since *LAI, G,* f_V, and K_{ext} are all derived from the input NDVI and $G(\mu)$ and μ depend only on the Earth-Sun geometry [*Sellers et al.,* 1996b]. As shown in Figure 7, the simulated GPP increases linearly with NDVI and then levels off at a maximum value defined by the maximum *LAI.* The *LAI* increases exponentially with NDVI to a biome specific maximum value based on observed values of *LAI* [*Sellers et al.,* 1996b].

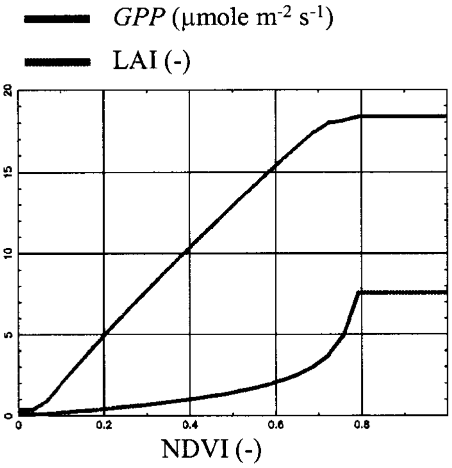

Figure 7. The simulated GPP increases linearly with NDVI and then levels off when the LAI reaches a biome dependent maximum value.

Photosynthesis Soil Moisture Scaling Factor

Opening the leaf stomata to absorb CO_2 also allows water to escape from the plant, creating a vacuum that sucks up additional water out of the soil. Plants tend to seek an optimal balance between photosynthesis and water loss. When water loss exceeds the ability of a plant to extract water from the soil, photosynthesis shuts down and the plant "wilts" due to drought stress. SiB2 accounts for drought stress by modeling a plant's ability to extract water out of the soil [*Sellers et al.,* 1996a]:

$$(30) \quad S_w = \frac{1}{1+\exp(0.02(\psi_c - \psi_s w_2^{-B}))},$$

where S_w is the GPP soil moisture scaling factor, ψ_c is the critical half point or optimal soil water potential (200 m for all biome types), ψ_s is the soil water potential at saturation (m), w_2 is the soil water fraction of saturation in the root zone soil layer, and B is an empirical constant. Figure 8 illustrates that the simulated GPP in SiB2 abruptly shuts down when the soil moisture falls below the wilting point.

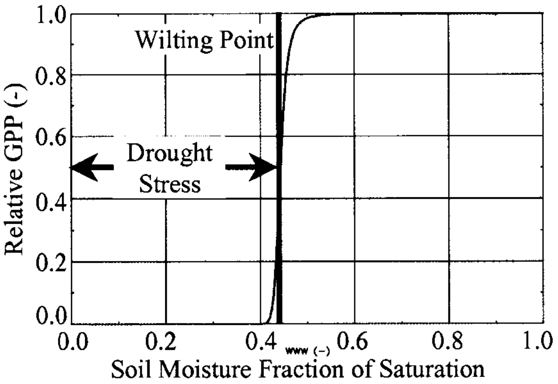

Figure 8. Simulated drought stress occurs when the root zone soil moisture falls below the plant's wilting point. The wilting point depends on the soil texture (percent sand and clay).

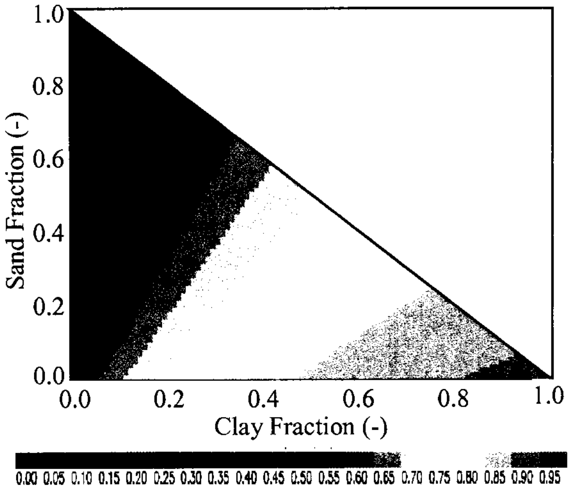

Figure 9. The wilting point increases with hydrogen bonding between the water and the soil particles. The wilting point decreases with increased sand and increases with increased clay. The white area results from the fact that the sand plus clay fractions must not exceed one.

Hydrogen bonding between the soil particles and the water determine the wilting point. Increased hydrogen bonding requires more work to extract soil water, resulting in a higher wilting point. Thus ψ_s and B, which control the wilting point, depend on soil texture [*Klapp and Hornberger*, 1978]. Figure 9 shows the wilting point as a function of sand and clay fraction. Sand, which consists primarily of quartz, has low hydrogen bonding while clay, which consists of minerals, has the highest. Thus, higher sand content decreases the wilting point and higher clay content increases it. Clay has a stronger influence on the wilting point than sand.

Photosynthesis from Stomatal Conductance

The stomatal conductance model in SiB2 uses the semi-empirical Ball-Berry-Collatz equation relating photosynthesis and leaf stomatal conductance [*Ball*, 1988; *Collatz et al.,* 1991, 1992; *Sellers et al.,* 1996a; *Sellers et al.,* 1997; *Denning et al.,* 1996a]:

$$(31) \quad g_s = m \frac{A_{ntop}}{c_s} h_s p + b \,,$$

where A_{ntop} is the net leaf assimilation rate at the top of the canopy, g_s is the leaf stomatal conductance (mole m^{-2} s^{-1}), p is atmospheric pressure, m is an empirical coefficient from observations (9 for C_3 plants, 4 for C_4 plants, and 6 for conifers), b is the minimum possible value for g_s (0.01 for C_3 plants and 0.04 for C_4 plants), c_s is the CO_2 partial pressure at the leaf surface (Pa), and h_s is the relative humidity at the leaf surface.

To obtain the overall conductance for the entire canopy, integrate g_s with respect to LAI over the entire canopy:

$$(32) \quad g_C = \int_0^{LAI} g_s dL = m \frac{A_n}{c_s} h_s p + bLAI \,,$$

where g_c is the canopy conductance, A_n is the canopy net CO_2 assimilation, L is cumulative LAI from the top of the canopy, and LAI is total leaf Area Index [*Sellers et al.,* 1994; *Sellers et al.,* 1996b; *Sellers et al.,* 1997]. The simulated A_n increases as the canopy air space humidity increases and evaporative water loss through the leaf stomata (transpiration) decreases (Figure 10). The lower rate of transpiration allows the stomata to open wider, allowing more CO_2 to diffuse into the leaf.

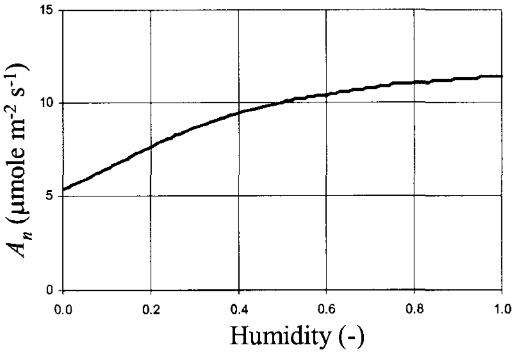

Figure 10. The simulated A_n increases with humidity because of reduced water loss through the leaf stomata.

Respiration

For our study, we adapted the respiration model of *Denning et al.,* [1996a], where the instantaneous value of R_g depends on soil temperature and moisture:

$$(33) \quad R_g = R^* R_f ,$$

where R^* is a combined soil temperature and moisture scaling factor and R_f is the respiration factor. Following *Raich et al.,* [1991], $R^* = f_T(T) f_W(W)$, where f_T is a temperature response function, T is temperature, f_W is a soil moisture response function, and W is the soil moisture fraction of saturation. We calculate R^* separately for each of six soil layers and one layer of overlying litter.

As shown in Figure 11, the simulated R_g increases exponentially with soil temperature [*Raich and Schlesinger*, 1992]:

$$(34) \quad f_T = Q_{10}^{\left(\frac{T_s - T_{ref}}{10}\right)} ,$$

where Q_{10} is the temperature response factor, T_s is the soil temperature and T_{ref} is a reference temperature (298.15 K). A Q_{10} of 1 indicates respiration does not respond to temperature. SiB2 assumes a Q_{10} of 2.4 [*Raich and Schlesinger*, 1992].

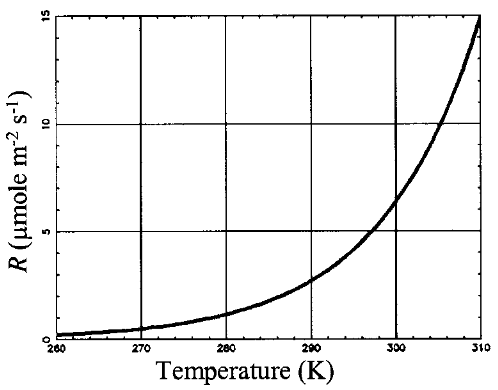

Figure 11. The simulated ground respiration increases exponentially with soil temperature.

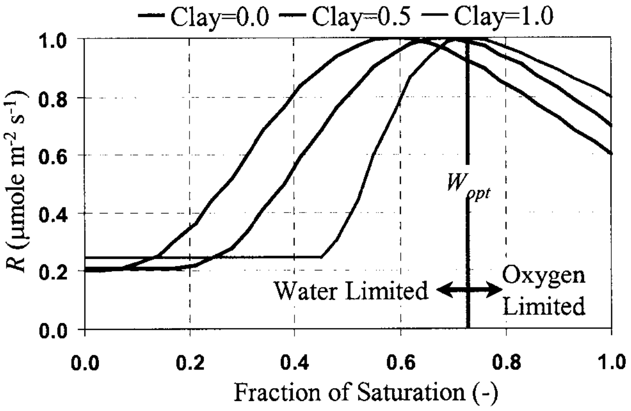

Figure 12. The simulated ground respiration increases with soil moisture to an optimal value, W_{opt}, that depends on the amount of clay in the soil. Water limits microbial growth in drier soils and oxygen availability in wetter soils.

As shown in Figure 12, the simulated R_g increases with soil moisture to an optimal value, then decreases [*Raich et al.*, 1991]:

$$(35) \qquad f_W = 0.2 + R_{sat}^{B} \quad \text{where } B = \left(\frac{w^{skew} - w_{opt}^{skew}}{1 - w_{opt}^{skew}} \right)^{2}$$

where f_w is the soil water content scaling factor, B is the wetness exponent, w_{opt} is the optimal soil wetness for respiration, *Skew* is the skewness exponent, and R_{sat} determines the respiration rate at soil water saturation [*Denning et al.*, 1996a]. *Wopt*, *Skew*, and R_{Sat} depend on the soil texture based on empirical studies of soil decomposition [*Raich et al.*, 1991]. *Wopt* occurs when the soil volume is at least 15% air [*Raich et al.*, 1991]. Too much water and the microbes do not have sufficient air to oxidize organic matter. Too much air (not enough water) and the microbe population drops and soil respiration decreases. W_{opt} varies between 0.6 and 0.7, depending on clay fraction.

f_w never drops below 0.2 because SiB pixels are large enough that some locations always have enough water for respiration and because some respiration occurs even under dry conditions. As the clay fraction increases, f_w is skewed to the right because increased clay suppresses respiration until the wetness reaches a critical value. The skewness exponent, *Skew*, models this shift to higher wetness values as the clay fraction increases. R_{Sat} assures that Moist falls between 60-80% at soil water saturation.

SiB2 is a balanced model, which means that respiration equals photosynthesis over a specified time period. We chose a 1-year residence time so that the carbon cycle at every model grid cell is nearly in balance, but that perturbations in photosynthesis in one year are felt over the following year as perturbations in ecosystem respiration. Flux tower observations indicate that NEE is nearly balanced [*Baker et al.*, 2003]. In a balanced, steady-state ecosystem, variability in respiration results from variability in the amount of the most labile carbon with the shortest turnover times, such as leaf litter and fine roots.

We parameterized respiration by releasing carbon accumulated by photosynthesis over one year, weighted by the temperature and soil moisture response functions. The total A_n over one year represents the size of the respiring carbon pool and R_f is the respiration rate that balances annual A_n when adjusted for soil temperature and water content:

$$(36) \quad R_f = \frac{\sum_{1\text{ year}} A_n}{\sum_{1\text{ year}} R^*}.$$

The fraction of accumulated carbon in the litter layer increases with the annual total accumulated carbon [*Denning et al.,* 1996]. The remaining accumulated soil carbon is divided among the six soil layers based on the fraction of total roots in each layer. We assume the root density decreases exponentially with depth with biome specific profiles [*Jackson et al.,* 1996]. We calculated a "rolling" R_f each month based on the previous 12 months of A_n and R^*.

A serious technical issue arises when initializing the magnitudes of respiring carbon pools on a global grid. Two approaches used in the past are 1) "spinning up" from a state of zero carbon [e.g., *Potter et al.,* 1993], and 2) extrapolating from representative field studies [e.g., *Craig et al.,* 1998]. Spin up requires long integration times, because some of the soil carbon pools are very long-lived. *Randerson et al.,* [1997] spun up the CASA model for 5000 simulated years before analyzing any results. Spin up has the advantage that ecosystem respiration and photosynthesis are everywhere balanced with respect to climate forcing, but is computationally prohibitive for our model (which uses a 10-min time step). Extrapolation is computationally efficient and allows for the possibilities of time-mean sources and sinks, but it is impossible to establish the veracity of global fields of biogeochemical pools defined everywhere from a few dozen field studies. *Craig et al.,* [1998] used extrapolation and produced regional net sources and sinks of CO_2 in excess of 5 GtC/yr, which seems unreasonable.

3.4 Statistics

We tested each hypothesis using various combinations of basic statistical techniques, such as, correlations, regressions, and trends [*Devore*, 1995]. Before calculating correlations and other statistics, we first removed long-term trends and then the seasonal variability. Since trends are stronger in some seasons than others, we removed trends month-by-month (the January trend, the February trend, etc). We calculated the mean seasonal variation from global maps of monthly averages by averaging all Januaries, Februaries, etc. This resulted in 12 global maps (one for each month) representing the mean seasonal variation. Subtracting mean seasonal variation maps from monthly average maps produced monthly anomaly maps:

$$(37) \quad X' = \overline{X} - \widetilde{X},$$

where X' is the monthly anomaly for variable X, $\overline{X}$ is the de-trended monthly mean of X, and $\widetilde{X}$ is the mean or climatological seasonal variation of X. From the anomaly maps, we produced maps of standard deviation, correlation, and other statistical parameters. Multiplying by grid cell area (which varies with latitude) and adding all land pixels produced total global land fluxes as a function of time.

We omitted trends, correlations, and regressions failing a single-tail student T-test at 95% significance [*Devore*, 1995]. The degrees of freedom for the T-test were based on the number of months, assuming each month was independent. For the statistics of spring events, the degrees of freedom were based on the number of years.

Many of the hypotheses involve relating trends between variables. To quantify the fraction of a trend in variable X due to a trend in variable Y, we used the congruent trend fraction:

$$(38) \quad f_x = \left| r \frac{t_y}{t_x} \right|,$$

where f_x is the congruent trend fraction, r is the regression coefficient between X and Y, t_x is the trend in X, and t_y is the trend in Y [*Thompson et al.,* 2000]. When f_x is zero, none of the trend X results from the trend in Y; when f_x is 1, the Y trend completely drives the X

trend. The congruent trend is statistically significant only where r, t_x, and t_y are all statistically significant.

Many of the hypotheses are based on the concept of climate memory. In much of our analysis, we tested how strongly a signal from variable Y persisted in variable X. Climate memory is typically defined as the e-folding time of its correlation function (the correlation of X with Y at various lag times). An alternative definition is the number of months until the lagged correlation function fails a statistical significance test. Data points in the lagged time series between X and Y that do not overlap reduce the degrees of freedom for the statistical significance test.

4. The effect of climate on inter-annual variability of terrestrial CO_2 fluxes

4.1 Introduction and Methods

In this chapter, we quantify how strongly various climate factors influence the inter-annual variability of NEE and identify the causes for regional differences. We then relate the NEE fluxes to atmospheric phenomena known to influence regional climate. We based our analysis on a SiB simulation using the ECMWF reanalysis and the FASIR NDVI data on a global, 1° by 1° latitude/longitude grid. ECMWF data were available for 1978 through 1993 and NDVI data for 1983 through 1999. Overlap between these two datasets limited the analysis to 1983 through 1993 (11 years). All the analysis in Chapter 3 is based on this 11-year simulation.

Table 1: Climate factors, SiB2 variables, and associated reference values

Climate Factor	Group	SiB2 Variable	Reference Value
Humidity	*GPP*	Leaf surface relative humidity	1
Light	*GPP*	PAR incident on canopy top	200 W m^{-2}
Leaf Area Index	*GPP*	Leaf Area Index	LAI_{max}
Temperature	*GPP*	Canopy temperature	298.15 K
Precipitation	*GPP*	Root zone soil water fraction	1
Temperature	*R*	Root zone soil temperature	298 K
Precipitation	*R*	Root zone soil water fraction	W_{opt}
Soil Carbon	*R*	Respiration factor	R_{fmean}

Four climate variables influence NEE in SiB2: temperature, precipitation, relative humidity, and incident light. We grouped them into those that affect *GPP* and those that affect *R* (Table 1). We listed precipitation and temperature twice because they affect both *GPP* and *R*. We chose SiB2 variables to represent each climate factor. These SiB2 variables change with the input weather data (which represents boundary layer values above the canopy), but also respond to changes in *GPP* and *R* and depend on the physical characteristics of the canopy and soil. For example, leaf surface humidity depends on plant transpiration, boundary layer humidity, and sensible heat flux. The influence of precipitation on *GPP* is limited to root zone soil moisture stress (i.e., drought stress).

GPP and *R* also depend on the amount of biomass. LAI represents the above ground biomass and is prescribed via the input NDVI. The rolling R_f represents the effect of short-term variation in below ground biomass due to variations in *GPP*. We neglected the influence of LAI on autotrophic canopy respiration (R_C), since it rarely exceeds 5% of *R* and exerts only a 0.3% influence on NEE variability.

To quantify how climate influences NEE variability, we calculated reference rates for *GPP* and *R* for each climate variable and compared them to the actual rate. We defined a climate variable influence as:

$$(39) \quad E_i = |GPP_i - GPP| \text{ or } E_i = |R_i - R|,$$

where E_i is the influence and GPP_i and R_i are reference rates for the i^{th} climate variable. When a climate variable does not influence NEE, $E_i = 0$. For example, if *GPP* is Rubisco (nitrogen) limited and the light level increases, E_{PAR}=0 since increased light would not affect *GPP*. The absolute value ensures non-negative monthly averages of E_i. All E_i were calculated each time step and have units of flux.

To calculate the reference rate (GPP_i or R_i) for each E_i, we kept all inputs the same and changed the i^{th} climate factor to a reference value as listed in Table 1. As humidity decreases, stomata close to minimize water loss, reducing *GPP* (i.e., humidity stress), so we chose the optimal humidity value of 1.0. For LAI, we chose the maximum possible LAI for each biome [*Sellers et al.,* 1996b]. For precipitation influence on *GPP*, we chose fully saturated soil ($W = 1.0$). For precipitation influence on *R*, we chose the optimal soil water content for maximum heterotrophic respiration, W_{opt} [*Raich et al.,* 1991]. For temperature influence on *GPP* and *R*, we chose reference values as identified in *Sellers et al.,* [1996a]. For *PAR* we chose a typical saturated value (the canopy usually absorbs more light than it can use for photosynthesis). For soil carbon, we chose an average respiration factor, R_{fmean}, based on the mean seasonal variation of A_n and R^* (defined above).

To assure E_i scales properly with *GPP* or *R*, (i.e., E_i is small when *GPP* is small and large when *GPP* is large), we calculated weighted monthly averages:

$$(40) \quad \overline{E_i} = \frac{\overline{GPP \cdot E_i}}{\overline{GPP}} \text{ or } \overline{E_i} = \frac{\overline{R \cdot E_i}}{\overline{R}},$$

where the overbar represents a monthly average. The weighted monthly average influence, $\overline{E_i}$, measures the sensitivity of *GPP* and *R* (and thus NEE) to changes in the i^{th} climate variable.

4.2 NEE Variability

The simulated, global land-surface NEE (GtC year^{-1}) shows a strong seasonal variation driven by vegetation in the northern hemisphere (Figure 13). The northern hemisphere has more land and vegetation than the southern hemisphere and dominates the global NEE seasonal cycle. NEE is most strongly negative during the northern hemisphere summer when global *GPP* is greatest. NEE is most strongly positive in northern hemisphere fall when assimilation drops off and global *R* dominates. The secondary minimum in November results from the surge in global *GPP* in the southern hemisphere spring. The NEE averages to zero over many years. However, small changes in *GPP* and *R* each year result in inter-annual NEE variability of about ± 2 GtC year^{-1}.

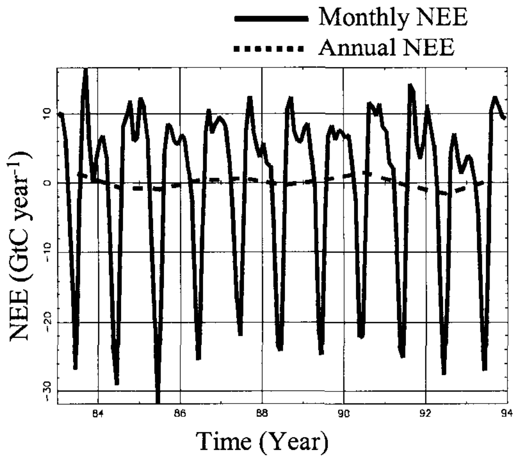

Figure 13. The Northern Hemisphere (NH) controls the seasonal changes in the simulated global NEE. Negative NEE spikes every June represent NH summer (*GPP* dominates NEE). The positive peak every September represents NH fall (respiration dominates NEE). The secondary minimum in November represents Southern Hemisphere (SH) spring. The annual NEE is near zero, but varies slightly year to year.

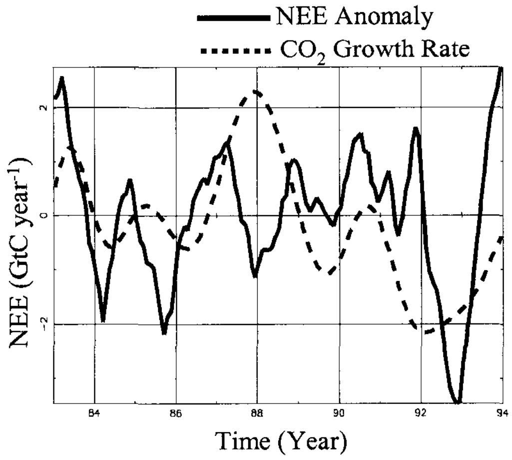

Figure 14. A 12-month running mean of the simulated global NEE anomalies captures the salient features and variability seen in anomalies of the measured global CO2 growth rate.

The simulated, global NEE anomaly (GtC year^{-1}) as a function of time (Figure 14) captures the variability of the measured global CO_2 growth rate extrapolated from flask measurements [*Conway et al.,* 1994]. The simulated NEE standard deviation (1.3 GtC year^{-1}) compares well with *Conway et al.,* [1994] (1.1 GtC year^{-1}) and *Houghton* [2000] (1.0 GtC year^{-1}). The peaks and valleys roughly line up, but a 12-month running mean NEE shows only a weak correlation of 0.27 with the observed CO_2 growth rate. The simulated NEE lags behind the observed CO_2 growth rate by 2-3 months because we did not include transport from the terrestrial sources to the flask measurement sites. Accounting for transport lag only increases the correlation to 0.3 because the observed CO_2 growth rate accounts for variability in ocean fluxes, biomass burning, and fossil fuel emissions while we do not. Still, the simulated NEE anomaly agrees fairly well with the global land flux estimates of *McGuire et al.,* [2001] using several biogeochemical models, *Bousquet et al.,* [2000] from inversion of flask measurements with a transport model, and *Kaduk and Heimann* [1997] from the Mona Loa record.

Some error in our simulated NEE may result from inaccuracies in NDVI estimates for tropical forests, which cover only 9% of the land surface, but account for 30% of global NEE. Spatial and temporal interpolation of NDVI data to account for persistent cloud cover over tropical forests artificially smooth LAI estimates, making it more difficult to predict year-to-year variations [*Los et al.,* 2000]. The CO_2 growth rate may not accurately account for land fluxes because the flask measurements sample predominantly marine rather than terrestrial air. Assuming a uniform 1-year turnover time introduces error into our NEE estimates since different biome types actually have different turnover times. Different turnover times for different biome types would change the timing of respiration anomalies, although the overall respiration variability would not change. Other sources of error include approximations in SiB2.

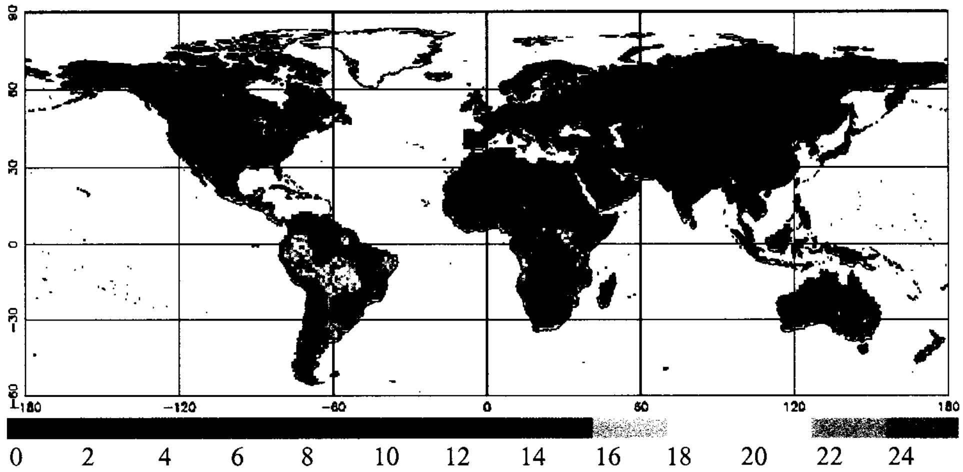

Figure 15. A map of simulated NEE standard deviation ($\mu g\ C\ m^{-2}\ s^{-1}$) indicates grasslands of South America and Africa have the greatest inter-annual variability. The anomaly in South America results from drought stress.

A map of simulated NEE standard deviations (Figure 15) show that tropical grasslands in South America and Africa have the highest inter-annual variability followed by northern extra-tropical forests. Equatorial rain forests have fairly low variability except for the western half of the Amazon basin. The large South American anomaly results from precipitation variability from El Niño-Southern Oscillation (ENSO) and potential problems with the ECMWF precipitation data (see below). Deserts are highly variable relative to their seasonal amplitude, but low *GPP* results in low NEE standard deviations.

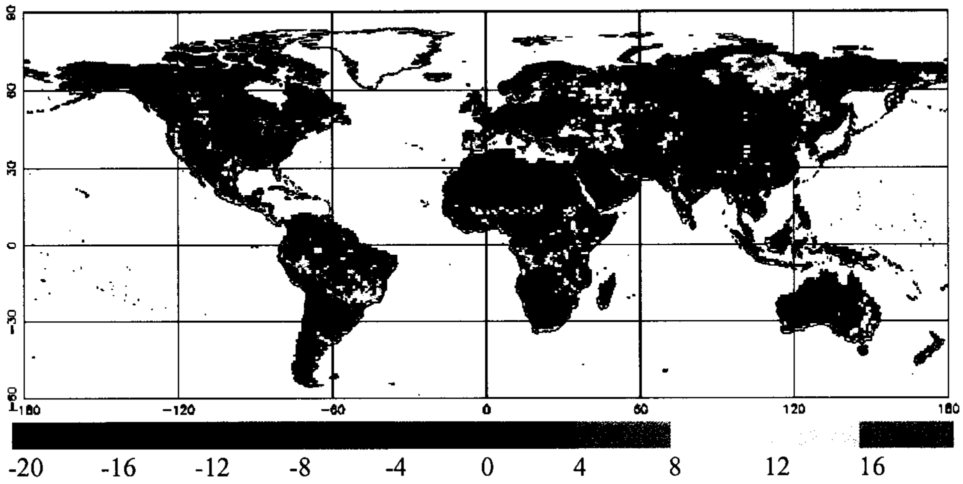

Figure 16. Typical simulated NEE anomalies (μg C m^{-2} s^{-1}) for July 1984 show a pattern of alternating positive and negative regions across the northern hemisphere. These regional anomalies tend to cancel such that the tropics dominate global NEE inter-annual variability.

Variability in the Northern extra-tropics is not as spatially uniform as implied in Figure 15. A typical map of simulated NEE anomalies for July 1984 (Figure 16) shows a pattern of alternating positive and negative regions across the northern hemisphere. The amplitudes of these simulated NEE anomalies range from 0.2 to 0.4 GtC yr^{-1} and are comparable to annual net carbon fluxes estimated from inversions of CO_2 flask measurements [e.g., *Bousquet et al.,* 2000; *Pacala et al.,* 2001]. The anomaly periods of 2-3 years are consistent with the 100% inter-annual variability seen by *Pacala et al.,* [2001] in their estimates of the North American carbon sink. These regional anomalies tend to cancel, negating the effect of much greater land area in the northern hemisphere.

While the northern hemisphere dominates the global NEE seasonal cycle, the tropics dominate global NEE inter-annual variability.

4.3 Climate Influences

NEE anomalies depend on the relative magnitude of *GPP* and *R* anomalies because both respond in similar ways to climate and tend to cancel each other. For example, for a given soil water content, both *GPP* and *R* tend to increase with temperature. A climate anomaly will produce an NEE anomaly if either *GPP* or *R* responds more vigorously to climate variability. The relative magnitude of *GPP* and *R* variance measures how strongly they influence NEE inter-annual variability:

$$(41) \quad f_{GPP} = \sigma^2_{GPP} \Big/ (\sigma^2_{GPP} + \sigma^2_R) \text{ or } f_R = \sigma^2_R \Big/ (\sigma^2_{GPP} + \sigma^2_R),$$

where f_{GPP} and f_R are the relative influences of *GPP* and *R* on NEE inter-annual variability, σ_{GPP} and σ_R are the standard deviations of *GPP* and *R*, and σ^2_{GPP} and σ^2_R are the variances of *GPP* and *R*. When $f_R = 0$, respiration has no influence on NEE inter-annual variability; when $f_R = 1$, respiration totally controls NEE variability (by definition, $f_{GPP} = 1 - f_R$).

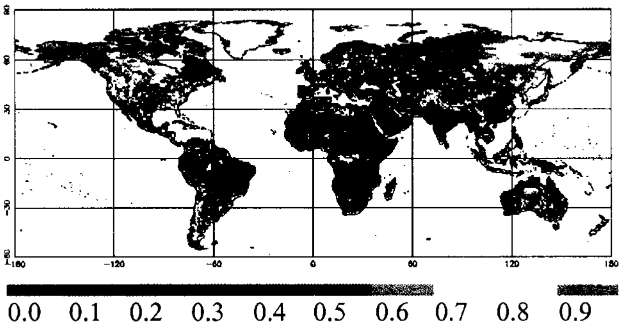

Figure 17. A map of the relative influence of respiration on simulated NEE inter-annual variability (0 means no influence, 1 means total control) indicates respiration dominates in high latitudes. GPP and respiration exert roughly equal influence in the tropics. The relative influences of respiration and GPP are based on the relative magnitudes of their variances.

R dominates simulated NEE variability at high latitudes (Figure 17) while *GPP* and *R* exert roughly equal influences in the highly variable tropical grasslands. Although *GPP* variability almost totally controls the deserts, these regions have such low *GPP* they do not significantly affect the global NEE inter-annual variability. Overall, *R* accounts for 59% and *GPP* for 41% of the global NEE inter-annual variability.

Isolating the causes for these regional differences is difficult because the climate variables are coupled and do not vary independently of one another. Feedback between climate variables often limits NEE variability. For example, increasing canopy temperature increases *GPP*, but also decreases relative humidity (which decreases *GPP*). Comparing relative magnitudes of $\overline{E_i}$ variance accounts for such cancellation and feedback between climate factors. The total influence of the *GPP* E_i group on NEE variability cannot exceed the relative influence of *GPP* itself such that

$$(42) \quad f_i = \frac{\sigma_i^2}{\sum \sigma_i^2} f_{GPP} \text{ or } f_i = \frac{\sigma_i^2}{\sum \sigma_i^2} f_R ,$$

where f_i is the inter-annual influence of the i^{th} climate factor and σ_i^2 the variance of $\overline{E_i}$. When $f_i = 0$, the climate factor has no influence and when $f_i = 1$, the climate factor totally controls NEE inter-annual variability. By definition, the sum of all f_i for both the *R* and *GPP* groups equals one ($\sum f_i = 1$). Maps of f_i show strong regional differences in the influence of climate on simulated NEE variability (Figure 18).

Precipitation control of *GPP* (Figure 18a) and *R* (Figure 18b) dominate throughout the tropics. The *GPP* and *R* precipitation influence patterns do not significantly overlap. The demarcation lies roughly where the average soil moisture equals W_{opt}. This division is especially clear in regions with a strong spatial gradient in soil moisture (e.g., sub-Saharan Africa and South America). The soil moisture influence on *GPP* represents drought stress. In semi-arid and desert regions with drier soils

(a) Precipitation Influence on GPP (b) Precipitation Influence on Respiration

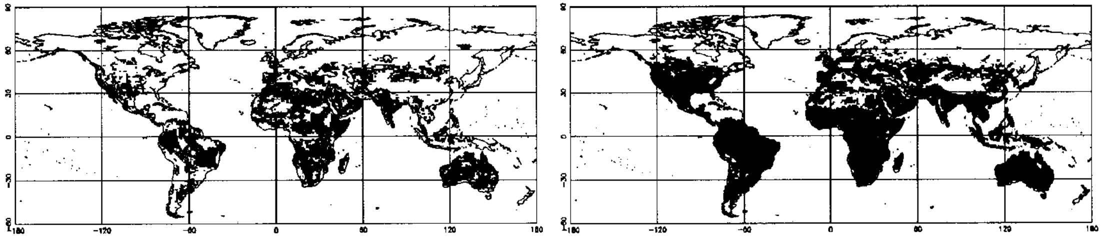

(c) Temperature Influence on GPP (d) Temperature Influence on Respiration

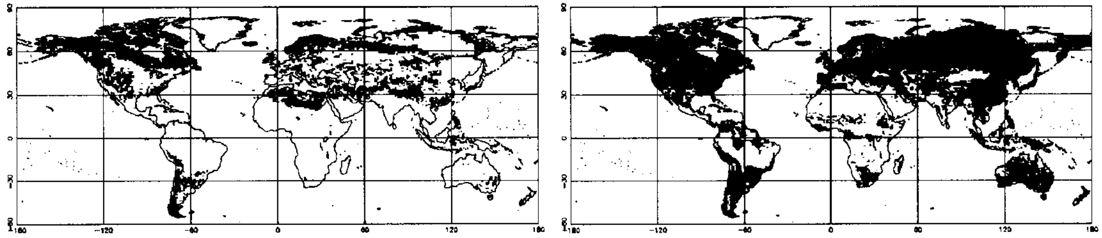

(e) Leaf Area Index Influence (f) Soil Carbon Influence

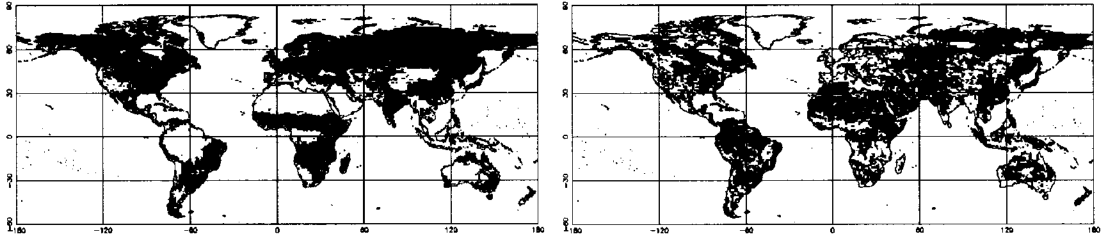

(g) Humidity Influence (h) Light Influence

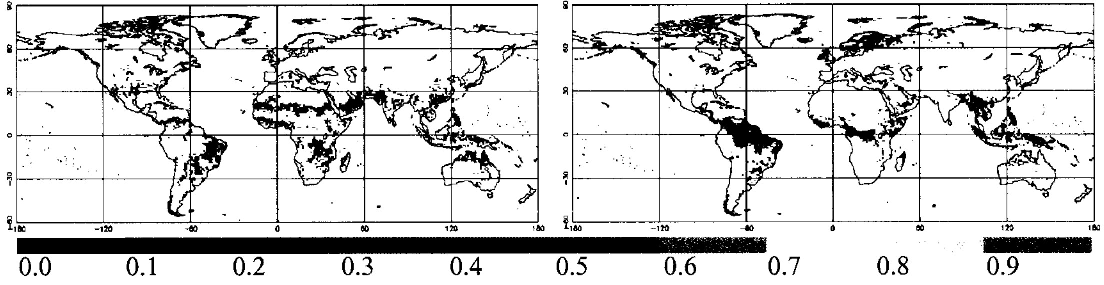

Figure 18. Relative influences of climate on the simulated NEE inter-annual variability based on relative magnitudes of variance indicate precipitation dominates in the tropics and temperature at mid and high latitudes. LAI influence represents climate influences during plant growth. PAR influences NEE variability only in regions of extensive rainfall. Soil carbon has the greatest influence in the tropics. Humidity exerts a weak influence. An value of 0 means no influence, 1 means total control. We omitted values less than 5%.

($W < W_{opt}$), precipitation control of *GPP* dominates because respiration can occur even in very dry soils while *GPP* ceases below minimum soil water content. In nearly saturated soils ($W > W_{opt}$), precipitation changes affect respiration, but do not induce drought stress, so precipitation control of *R* dominates. *Tian et al.,* [1998] saw a similar dependency in their simulation of NEE in the Amazon basin.

The large NEE anomaly in South America (Figure 15) may result from problems with the ECMWF precipitation data as well as naturally occurring drought stress. Spatial patterns of precipitation differ between datasets derived from rain gauge data and those from reanalysis using a model [*Costa and Foley*, 1998]. Our simulated anomaly differs slightly from that simulated by *Tian et al.,* [1998] because they used precipitation based on rain gauge data. The precipitation data from the ECMWF reanalysis is diagnostic and unconstrained by rain gauge measurements. The spectral representation of topography in ECMWF produces false undulations in the land surface, creating potentially suspect precipitation anomalies in South America [*Costa and Foley*, 1998]. Bright NDVI data may indicate plant growth, but the ECMWF may systematically put the rain somewhere else, resulting in drought stress.

Temperature influence on respiration dominates NEE variability at high latitudes (Figure 18d). The temperature response function for *R* is exponential, so small soil temperature anomalies can produce large *R* anomalies, especially during peak temperatures in the summer. By contrast, *GPP* is relatively insensitive to temperature except at extreme high and low temperatures (Figure 18c). The resulting temperature influence on *GPP* is very small and reflects variability in temperature extremes at high latitudes, high altitudes, and deserts. Essentially, *R* goes up and down with temperature relative to a more stable *GPP*.

LAI influences NEE inter-annual variability in tropical grasslands, high-latitude forests and tundra (Figure 18e). The LAI influence represents the indirect effect of climate (precipitation, temperature, snow cover, etc.) on plant growth, probably when the ecosystem is most sensitive, such as spring [*Houghton*, 2000]. In general, snow cover influences LAI in the high northern latitudes, temperature in the mid-latitudes, and a combination of precipitation and temperature in the tropics [*Los et al.,* 2001].

Soil carbon has a fairly evenly distributed influence on NEE inter-annual variability, peaking at the equator and decreasing towards the poles (Figure 18f). Like LAI, soil carbon represents the indirect effects of climate on soil organic matter due to *GPP* anomalies. The resulting soil carbon anomalies last a year because of the assumed 1-year turnover time in the rolling respiration factor. Consequently, regions where *GPP* dominates NEE variability also show a strong soil carbon influence.

Humidity shows a weak, but fairly uniform influence on NEE inter-annual variability (Figure 18g). Transpiration during photosynthesis generally keeps the leaf surface humidity near saturation, making it insensitive to changes in ECMWF humidity (defined in the boundary layer above the canopy). Humidity influences *GPP* only when high sensible heat flux mixes relatively dry boundary layer air down into the canopy, reducing the humidity at the leaf surface and causing humidity stress.

Although globally weak, PAR shows a fairly strong regional influence in equatorial tropical forests where persistent cloud cover reduces the light available for plant growth (Figure 18h). In SiB2, photosynthesis is light-limited only at low light levels in the early morning and late evening (PAR below about 100 W m^{-2}). At other times, nitrogen or export capacity limit *GPP*. The length of time each day that *GPP* is light-limited determines the overall influence of PAR. Precipitation anomalies change cloud cover and incident PAR, which determines the time each day when *GPP* is light-limited.

Because of the regional cancellation in the northern hemisphere, precipitation in the tropics dominates the simulated global NEE inter-annual variability seen in Figure 14. Precipitation influence on *GPP* and *R* combined account for 44% of the global NEE variability (precipitation influence on *GPP* accounts for 32% while precipitation influence on *R* accounts for 12%). Variability in LAI and soil carbon combined account for 35% of global NEE variability (23% and 12% respectively). Overall humidity and PAR influences on global NEE variability are very weak (2% and 3% respectively). Temperature accounts for 16% of the global NEE inter-annual variability. The temperature influence on *GPP* is weak (1% globally). Despite dominating the northern hemisphere, regional cancellation reduces the global influence of temperature on respiration to 15% of the simulated global NEE variability. Having quantified these influences, we examined in detail two climatic phenomena known to affect inter-annual variability in temperature and precipitation: the AO and ENSO.

4.4 The Arctic Oscillation and NEE Variability

The AO is characterized by a north-south dipole in the strength of the zonal wind between 35°N and 55°N [*Thompson and Wallace*, 2000; *Thompson and Wallace*, 2001]. Positive AO polarity has stronger westerly winds north of 45°N and weaker winds south of 45°N, which favors increased advection of relatively warm oceanic air deep into continental interiors. Negative AO polarity has weaker mean zonal flow and more blocking, pulling cold Arctic air masses down into continental interiors. Positive AO polarity produces positive temperature anomalies over land; negative polarity produces negative anomalies. Since the AO primarily influences the northern hemisphere and since 50% of all northern hemisphere NEE anomalies occur in summer, we focused our analysis on June-July-August (JJA).

(a) JJA Temperature-AO Correlations

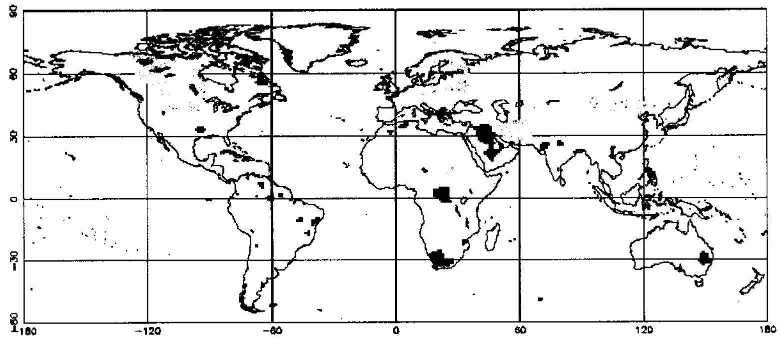

(b) JJA Soil Moisture-AO Correlations

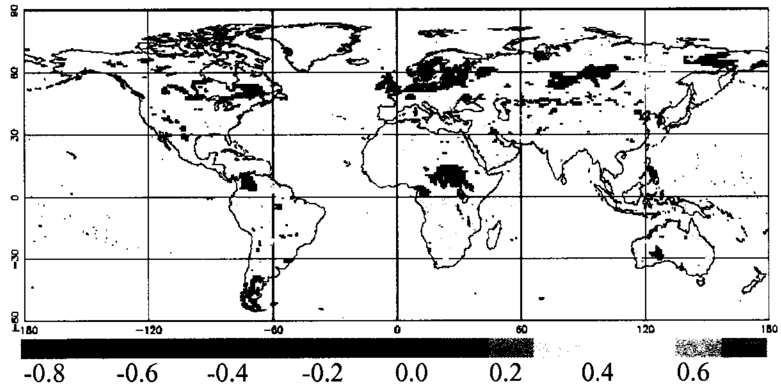

Figure 19. The Arctic Oscillation (AO) advects warm oceanic air into continental interiors, resulting in positive correlations with NCEP air temperature and negative correlations with simulated soil moisture in northern Europe, central Canada and central Asia. We focused on June-July-August (JJA) because 50% of all northern hemisphere NEE anomalies occur in the summer. Southern hemisphere correlations probably do not reflect direct AO influence.

Figure 19 shows summer (JJA) correlations of air temperature from the NCEP reanalysis and simulated soil moisture with the AO index. Figure 20 shows JJA correlations of simulated *GPP*, *R*, and NEE with the AO index. The AO index, *GPP*, and temperature data show positive trends for 1983-93 [*Los*, 1998; *Thompson et al.*, 2000], which we removed prior to correlation. We omitted correlations failing the t-test at 95% significance [*Devore*, 1995]. The degrees of freedom for the t-test are based on the total number of summer months in our simulation (assuming each month is independent). Warm air advection associated with positive AO polarity shows up as positive temperature correlations in northern Europe, Canada, and central Asia. The reduced blocking associated with positive AO polarity deceases rainfall in the same regions, resulting in negative soil moisture correlations.

(a) JJA NEE-AO Correlation

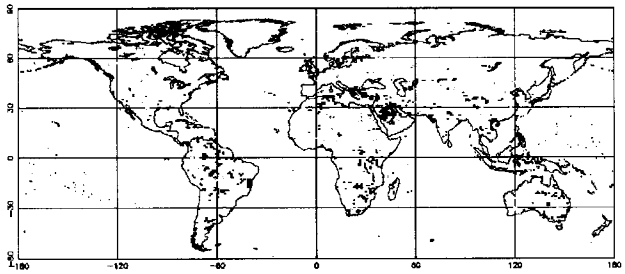

(b) JJA Respiration-AO Correlation

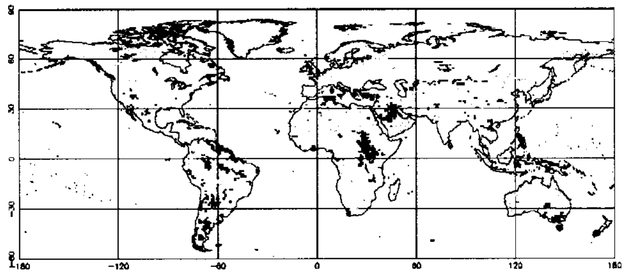

(c) JJA GPP-AO Correlation

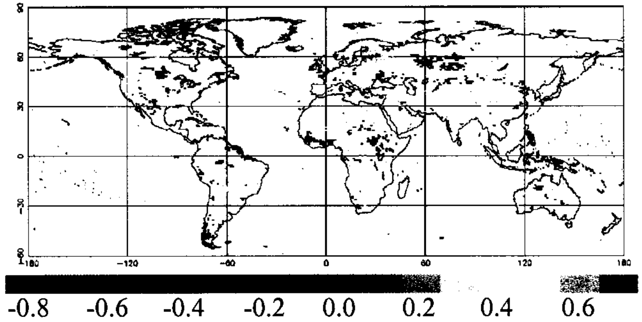

Figure 20. Simulated respiration and GPP anomalies often cancel, resulting in weak correlations between the AO Index and the simulated NEE. The strongest AO signal is in Northern Europe. Southern hemisphere correlations probably do not reflect direct AO influence.

Figure 20 indicates the AO signal is strongest in northern Europe for *GPP* and *R*, but competing effects and cancellation result in weak AO correlations with simulated NEE. As seen in Figure 18, several climate factors control NEE variability in Northern Europe: temperature (via *GPP* and *R*), LAI, precipitation (via *R*), and humidity. Decreased *R* due to reduced soil moisture partially cancels increased *R* due to higher temperatures. Decreased *GPP* due to increased humidity stress partially cancels increased *GPP* due to warmer temperatures. The result is modest positive AO correlations with *R* and *GPP*. While both *GPP* and *R* increase with temperature, *R* responds more vigorously. The GPP anomalies partially cancel the *R* anomalies, resulting in weak positive NEE correlations. Similar cancellation occurs in Canada and central Asia resulting in even weaker NEE correlations with the AO.

Correlations scattered throughout the southern hemisphere are probably random associations and do not reflect direct influence by the AO.

Overall, temperature effects from the AO dominate over precipitation effects. The limited spatial extent of the AO influence combined with cancellation effects result in a very weak AO signal in the NEE variability in summer. The AO can explain part of the strong temperature influence across the northern hemisphere and the Northern Europe portion of the simulated spatial pattern for NEE, but not the 2-3 year cycle in NEE variability.

4.5 ENSO and NEE Variability

El Niño-Southern Oscillation (ENSO) is characterized by weaker or stronger trade winds in the equatorial Pacific. Weaker trade winds (El Niño) cut off cold-water upwelling off of South America and shift the Pacific warm water pool from off Asia eastward to the central Pacific. Strong trade winds (La Niña) push the Pacific warm pool westward towards Australia. El Niño and La Niña are the extremes of alternating sea level pressures between east and west Pacific known as the Southern Oscillation. The Pacific warm pool moving with ENSO has a domino effect, shifting rainfall and temperature patterns around the globe [*Green et al.,* 1997]. ENSO has a period of two to seven years. Our simulation covered two El Niño events and part of a third (1982-83, 1986-87, and 1991-92) and two La Niña events (1984-85, 1988-89).

Figure 21 shows correlations of NCEP air temperature and simulated soil moisture with a Southern Oscillation Index (SOI) based on the sea level pressure difference between Tahiti and Darwin for 1983-93. We removed trends and omitted correlations failing the t-test at 95% significance. Negative SOI corresponds to El Niño;

positive SOI corresponds to La Niña. Negative correlations mean increases during El Niño; positive correlations mean decreases during El Niño.

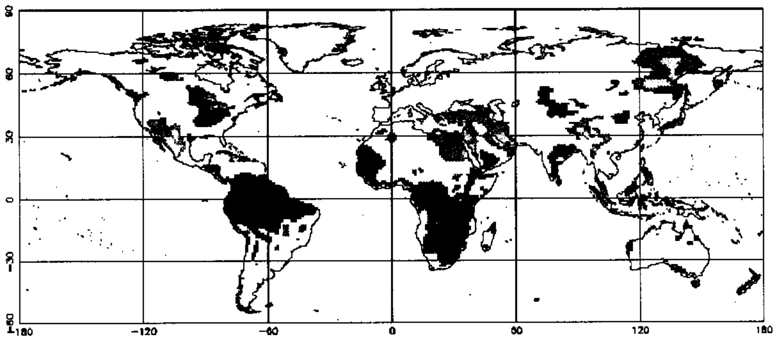
(a) Temperature-ENSO Correlations

(b) Soil Moisture-ENSO Correlations

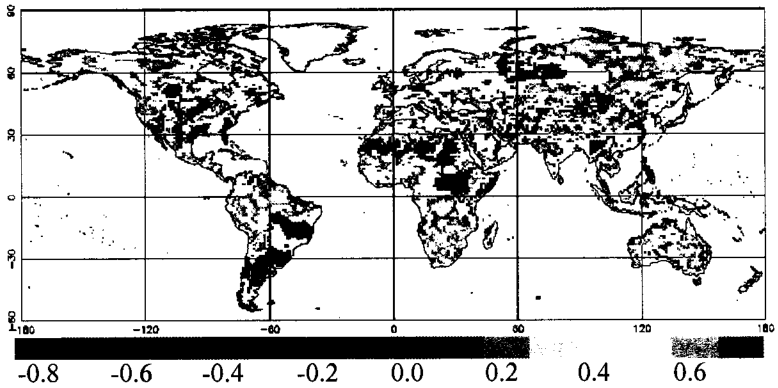

Figure 21. Correlations between the Southern Oscillation Index and NCEP air temperature and simulated soil moisture indicate ENSO strongly influences global precipitation patterns, especially in the tropics.

Rainfall patterns throughout the tropics shift as the Pacific warm pool moves east and west with ENSO. For example, rainfall (and thus soil moisture) in Australia drops during El Niño as the Pacific warm pool moves to the east, resulting in positive SOI correlations. Decreased rainfall reduces cloud cover, increases solar heating, and reduces evaporative cooling [*Kaduk and Heimann*, 1997], which increases temperature and produces negative SOI correlations. Temperature is fairly constant in the tropics, so although the correlations appear strong, the effect is small. In East Russia, reduced cloud cover associated with reduced precipitation during El Niño increases radiative cooling, decreasing temperatures and producing positive SOI correlations. In summary, ENSO primarily affects global precipitation and soil moisture patterns and weakly influences temperature.

(a) NEE-ENSO Correlation

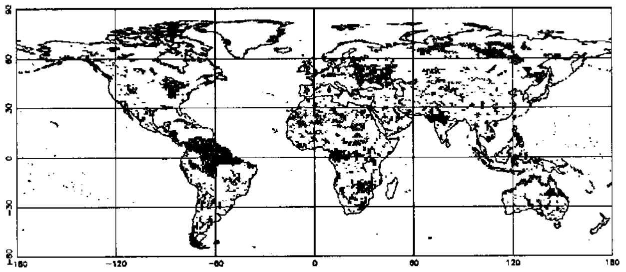

(b) Respiration- ENSO Correlation

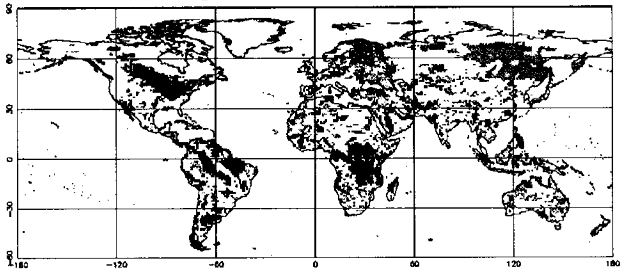

(c) GPP-ENSO Correlation

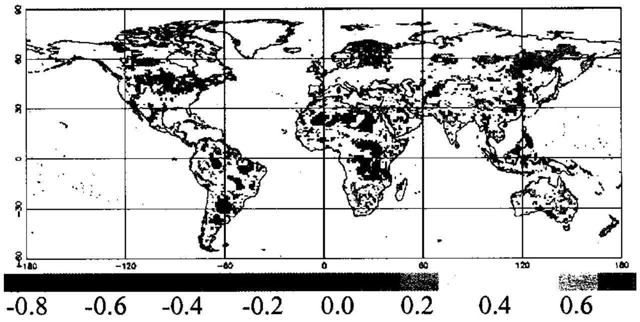

Figure 22. Correlations with a Southern Oscillation Index indicate ENSO influences simulated NEE variability primarily in the tropics, consistent with expected shifts in precipitation.

The effects of shifting rainfall patterns on simulated *GPP* and *R* can cancel (Figure 22). For example, in Australia and India, both *R* and *GPP* show positive correlations with SOI (both decrease as precipitation drops during El Niño). Precipitation controls NEE variability for Australia and India (Figures 18a and 18b). Areas controlled by drought stress show negative NEE correlations ($R > GPP$ during El Niño). Areas controlled by soil moisture for respiration show positive NEE correlations ($R < GPP$ during El Niño). Zero NEE correlations indicate the *R* and *GPP* anomalies cancel.

The large NEE anomaly in South America (Figure 15) results from drought stress due to rainfall shifting with ENSO. The soil water content relative to the optimum for respiration, W_{opt}, drives the spatial pattern of this anomaly. The average soil water content exceeds W_{opt} in the Amazon basin and decreases southward and westward to less than W_{opt} in the highlands of central and western South America. During El Niño, rainfall shifts from the Amazon basin and central South America to the west and southeast. The soil water in the Amazon basin decreases and respiration increases, but *GPP* is not affected, resulting negative correlations for *R* and NEE, but weak correlations for GPP. In the central South American highlands, the soil water is less than W_{opt}, so decreased rain during El Niño reduces *R* and introduces drought stress, resulting in positive *R* and *GPP* correlations. Drought stress coupled with possible problems with the ECMWF precipitation data (described above) produce a highly variable NEE anomaly, but partial cancellation between *GPP* and *R* weakens the NEE correlation with ENSO.

The ENSO influence above 30°N is weak. Temperature variability due to ENSO shows up as a strong correlation with *R* in east Russia. The high values of LAI influence on NEE variability (Figure 18g) and corresponding high soil moisture correlations indicate ENSO influences snow cover, melting times, and spring plant growth [*Kaduk and Heimann*, 1997, *Los et al.,* 2001] in Europe and Canada. This may partly explain the simulated NEE anomaly pattern in the northern hemisphere. However, ENSO does not explain the strong temperature influence across the northern hemisphere or the 2-3 year cycle in NEE variability.

Overall, ENSO primarily affects NEE variability in the tropics through changes in precipitation, explaining much of the NEE variability simulated in South America, Africa, and Asia. While our correlations are statistically significant at 95% assuming each month is independent, our simulation covers only three ENSO cycles. Our results are consistent with that expected from ENSO, but a more rigorous analysis requires simulations of several decades.

4.6 Conclusions

The global NEE from our simulation captured the salient features of the observed global CO_2 growth rate. The detailed process information and high time resolution in SiB2 allowed us to isolate and quantify the influences of climate on global and regional inter-annual variability of NEE. Further, using remotely sensed LAI we estimated the overall influence of plant biomass on GPP variability. Assuming a 1-year turnover time we estimated the effect of below ground biomass on respiration variability. Using biome specific turnover times would improve the timing of respiration anomalies. Adding an ocean model would improve the match with the observed CO_2 growth rate. Explicitly tracking various carbon and nitrogen pools would isolate the effects of land use, growing season length, nitrogen availability, and other factors that influence NEE inter-annual variability.

The tropical grasslands in South America and Africa show the highest NEE variability. The large South American NEE anomaly is driven by shifting precipitation with ENSO, but may also result, in part, from ECMWF precipitation errors. The simulated NEE in the northern hemisphere shows a pattern of alternating positive and negative anomalies with periods of 2-3 years and amplitudes consistent with inversions of CO_2 flask measurements. The alternating anomalies tend to cancel such that the tropics control global NEE inter-annual variability while the northern hemisphere controls the global NEE seasonal cycle.

Due to cancellation and competing effects, no single climate variable controls global or regional NEE inter-annual variability. Precipitation exerts the greatest influence (44% of global NEE variability), followed by LAI (23%), temperature (16%), and soil carbon (12%). Humidity and available light do not strongly influence global NEE variability. Climate influences have strong regional differences: temperature influence on respiration dominates in the extra-tropics while precipitation influence on GPP and R dominates in the tropics. For regions controlled by precipitation the soil water content relative to W_{opt} determines whether GPP or R controls NEE variability. In dry soils ($W < W_{opt}$), GPP dominates; in wet soils ($W > W_{opt}$), R dominates.

The influence of ENSO on NEE variability is consistent with that expected for shifting precipitation patterns in the tropics, especially for the large South American anomaly. A definitive assessment requires a longer time record, since our simulation covered only 3 ENSO cycles. Except in northern Europe, temperature advection by the AO does not significantly influence NEE variability in summer. Neither the AO nor ENSO fully explain the temperature influence on respiration or the simulated NEE anomaly pattern in the northern hemisphere.

5. The winter Arctic Oscillation, the timing of spring, and carbon fluxes in the northern hemisphere

5.1 Introduction and Methods

In this chapter, we assess the AO influence on variability of spring carbon fluxes and on long-term trends towards warmer and earlier springs. We included a short review of available observations and any previous research relating the AO to the timing of spring. We based our analysis on a SiB simulation using the NCEP reanalysis and the FASIR NDVI data on a global 1.875x 1.904° grid. All analysis in Chapter 4 is based on this 45-year simulation.

We modeled three events typically used to define the start of spring: leaf out, snowmelt, and soil thaw. For each we identified a representative variable and calculated the date when that variable crossed a threshold value. Soil thaw occurred when the topsoil layer in SiB (7 cm depth) permanently exceeded 0° C. Snowmelt occurred when the fractional snow cover fell below 25%, which roughly corresponds to the end of spring runoff [*Cutforth et al.,* 1999].

The timing of leaf out (defined as the start of leaf development in the spring) depends primarily on temperature. After senescence in autumn, tree buds enter a state of dormancy. After sufficient chilling by exposure to cold temperatures, dormancy ends and the buds grow in response to warming in spring. When the buds have received a critical amount of cumulative thermal energy, they burst and leaf out [*Cannell and Smith*, 1983, 1986; *Hunter and Lechowicz*, 1992; *Kramer*, 1994; *White et al.,* 1997; *Menzel and Fabian*, 1999; *Vaganov et al.,* 1999; *Beaubien and Freeland*, 2000; *Menzel*, 2000; *Los et al.,* 2001; *Chen and Pan*, 2002; *Menzel*, 2003].

Available models of leaf out are empirical and vary widely in complexity and in how they represent cumulative chilling and warming [*Hunter and Lechowicz*, 1992; *Kramer*, 1994; *Chuine*, 2000]. Comparisons between models indicate the thermal time model performs well and is adequate for predicting budburst [*Hunter and Lechowicz*, 1992; *White et al.,* 1997; *Tanja et al.,* 2003]. The thermal time model assumes a constant amount of chilling each year and represents bud warming as a cumulative sum of growing degree days from a fixed start date:

$$(43) \quad S = \sum_{\text{January 1}}^{S=S^*} GDD \quad GDD = \begin{cases} 0 & T < T_{base} \\ (T - T_{base})\Delta t & T \geq T_{base} \end{cases},$$

where S is the cumulative thermal forcing, S^* is the critical cumulative thermal forcing for leaf out, GDD is growing degree day, T is the NCEP surface air temperature, T_{base} is the base temperature, and Δt is the model time step in days [*Cannell and Smith*, 1983; *Chuine*, 2000]. Leaf out occurs on the date when S exceeds S^*.

S^* decreases exponentially with increased chilling in fall and winter:

$$(44) \quad S^* = a + be^{rC},$$

where C is the cumulative chilling days, a is the thermal time asymptote when the plant is fully chilled, b is the thermal response slope, and r is the chilling response slope ($r < 0$) [*Cannell and Smith*, 1983; *Murray et al.,* 1989; *Nikolov and Zeller*, 2003]. We assumed chilling occurs only below the base temperature:

$$(45) \quad C = \sum_{\text{November 1}}^{\text{April 30}} CD \quad CD = \begin{cases} 1 & T_d < T_{base} \\ 0 & T_d \geq T_{base} \end{cases},$$

where CD is chilling day and T_d is the daily average NCEP surface air temperature [*Cannell and Smith*, 1983, 1986; *Hunter and Lechowicz*, 1992; *Murray et al.,* 1989; *Kaduk and Heimann*, 1996; *Chuine*, 2000; *Nikolov and Zeller*, 2003].

Kaduk and Heimann [1996] used NDVI data to estimate biome specific values of *a*, *b*, and *r* by ensuring the estimated leaf out date corresponds to the date when the interpolated NDVI crosses a threshold value. We could not be sure that their values would apply to the FASIR NDVI. Soil reflectivity masks the relationship between NDVI and plant phenophases [*Chen and Pan*, 2002], making our choice of threshold value and interpolation technique somewhat arbitrary.

Instead, we calculated an average S^* curve from S^* curves using empirical values of *a*, *b*, and *r* for 15 species of trees and shrubs [*Murray et al.,* 1989; *Cannell and Smith*, 1983]. We assumed a start date of January 1 for *S* and November 1 for *C* [*Murray et al.,* 1989; *Cannell and Smith*, 1983]. We chose a stop date of April 30 for *C* because we found longer time periods did not change S^*.

The choice of T_{base} is more important at high latitudes than in the temperate regions. In temperate regions (south of 55°N) T_{base} and S^* compensate for each other: lowering T_{base} lowers *C* and increases S^* such that leaf out occurs at nearly the same time. For vast regions at high latitudes, S^* lies near its asymptotic limit, essentially independent of *C* and thus T_{base}. However, *S*, *GDD*, and leaf out still depend on T_{base}. We used the same T_{base} of 5 °C *Murray et al.,* [1989] and *Cannell and Smith* [1983] used to empirically estimate *a*, *b*, and *r*.

C did not vary substantially from year-to-year, so we calculated a map of S^* that did not vary with time (Figure 23). At high latitudes, the chilling is very deep such that S^* lies near its asymptotic limit of 62 °C day. Near the equator, where *C* approaches zero, we placed an upper limit on S^* of 200 °C day.

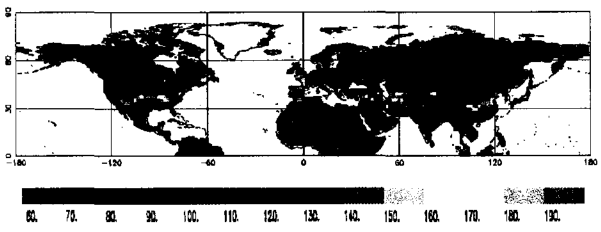

Figure 23. The 1958-2002 mean value of S^*, the critical thermal time to leaf-out (°C day), shows little spatial variability except for a sharp increase near 30N. Chilling days are calculated from November through April using NCEP surface air temperature with a base temperature of 5 °C using an empirical relationship derived from observed dates of leaf out.

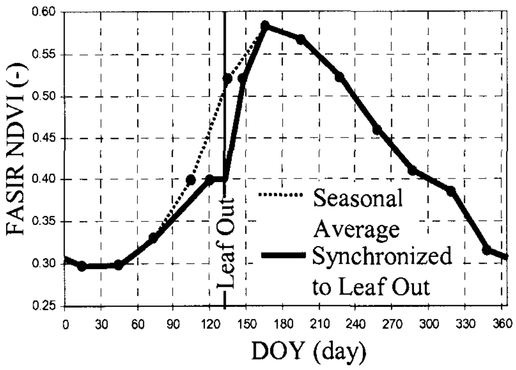

Figure 24. To obtain inter-annual variability in estimated LAI, we synchronized the interpolation of the seasonal average FASIR NDVI data with the estimated date of leaf out. This sample is taken from (30E, 55N) for 1958.

The NCEP data were available from 1958-2002 (45 years) while the NDVI dataset covered only 1982-98 (17 years). For 1982-1998, we used the actual NDVI data and for 1958-1981 and 1999-2002 we used an average seasonal cycle of NDVI. Normally, SiB2 uses linear interpolation to estimate daily values of NDVI from the monthly composite values. However, an average seasonal cycle for NDVI would produce the same values of LAI each year, regardless of the timing of spring. Consequently, we synchronized the NDVI interpolation to our estimated date of leaf out. We assumed the maximum NDVI for the month prior to leaf out occurred at the end of the month. For the month of leaf out, the NDVI stays constant at the previous month's value until the estimated date of leaf out. We then interpolated to next NDVI value over a two-week green-up period after leaf out. Figure 24 illustrates the interpolation of observed NDVI values for a randomly chosen pixel at mid-latitudes (30E, 55N) for 1958. This simple synchronization between leaf out and NDVI was sufficient for our study, but using the actual dates for each NDVI value [*White et al.*, 1997] or more sophisticated curve fitting techniques [*Potter et al.*, 1999; *Chen and Pan*, 2002; *Shabanov et al.*, 2002] would result in smoother NDVI curves.

5.2 Results

(a) Leaf-Out

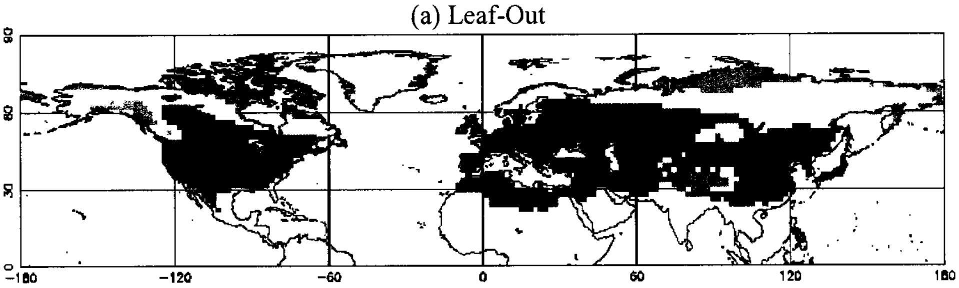

(b) Snowmelt

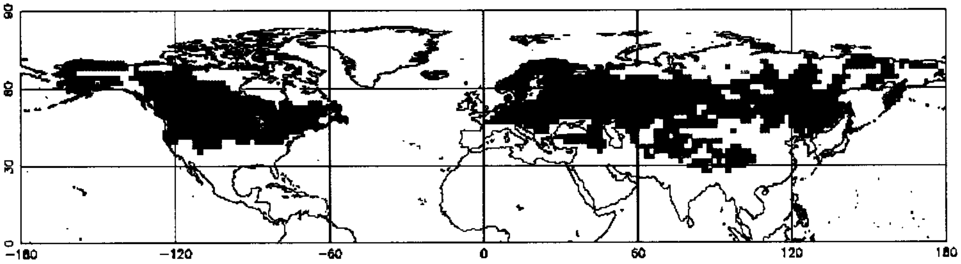

(c) Soil Thaw

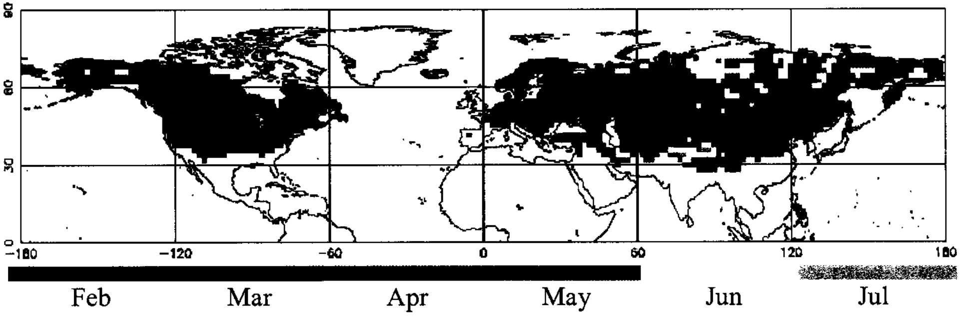

Figure 25. The mean month of simulated leaf-out (a), occurs after snowmelt (b) and soil thaw (c). Snowmelt and soil thaw occur at nearly the same time except at the highest latitudes. Below the southern margins at 30-40N latitude, the spring event is ill-defined or never occurs.

The 45-year mean values of simulated leaf out, snowmelt, and soil thaw (Figure 25) show that leaf out occurs after snowmelt and soil thaw, and all occur later at higher latitudes and altitudes. Above 60°N latitude, snowmelt tends to occur after soil thaw because SiB2 allows patchy snow to persist longer than observed. South of the southern margin, spring is either undefined or does not occur (e.g., it never snows in the tropics, so snowmelt never occurs). Along the southern margin, the specific event may occur some years, but not others, resulting in questionable February mean values. For example, average snowmelt dates in February represent erratic or intermittent snows in January or March (it snows in some years, but not others).

Large-scale data to validate our leaf out model is extremely scarce. The average S^* curve is based on temperate tree and shrub species from Europe, so the uncertainty in estimated leaf out increases with distance from Europe. Our estimated leaf out dates at high latitudes, where S^* becomes independent of T_{base}, are particularly uncertain. The literature references hundreds of phenological studies, but most focus on one or two species at a specific location. A global leaf out model needs global datasets of observed leaf out for many species for development and validation.

As expected from a model based on temperature, our predicted leaf out occurs about a week after spring in Europe estimated from observed temperatures [*Jaagus et al.,* 2003]. Our estimated leaf out is about one week earlier than observed birch leaf out in Europe [*Ahas et al.,* 2002]. The estimated leaf out is several weeks earlier than leaf out for the continental United States estimated from NDVI [*White et al.,* 1997]. Nevertheless, the estimated leaf out at all latitudes is consistent with the timing of spring increases in the FASIR NDVI.

Except along the southern margin, simulated leaf out, snowmelt, and soil thaw show similar spatial patterns of variability, as represented by standard deviation (Figure 26). Variability is highest where the definition of spring is questionable. Leaf out is well defined everywhere and shows fairly uniform variability ranging from ±5-14 days. Intermittent, late season snows along the southern margin and in Siberia produce patches of variability in snowmelt in excess of ±20 days. Along the southern margin, the soil freezes in some years, but not in others, resulting in variability of soil thaw ranging from ±14-21 days.

(a) Leaf-Out

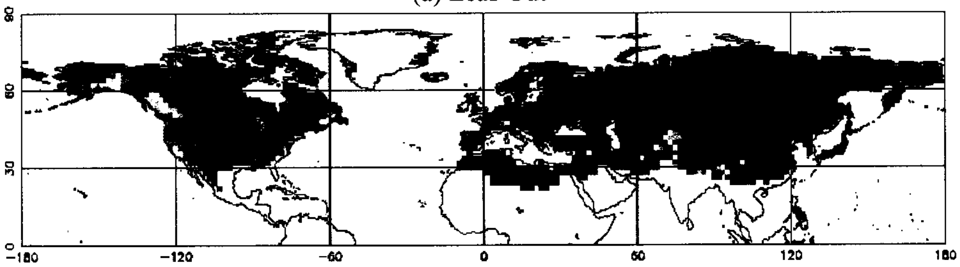

(b) Snowmelt

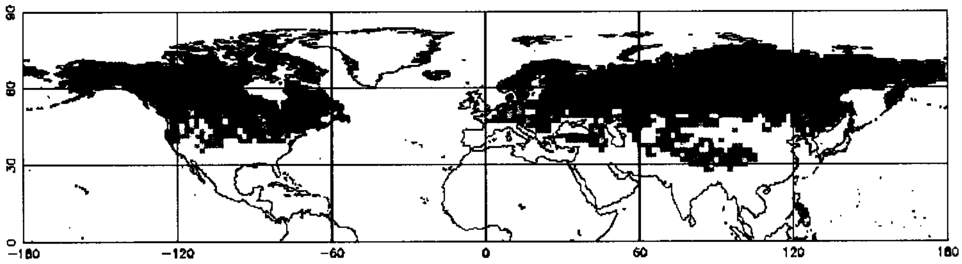

(c) Soil Thaw

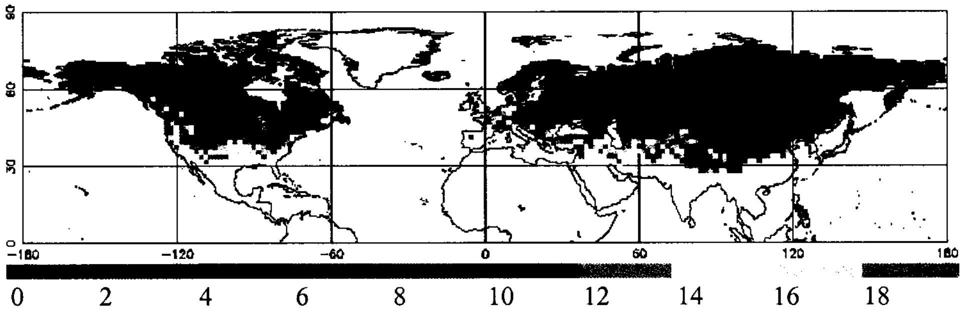

Figure 26. Standard deviations (day) of simulated leaf-out (a), snowmelt (b), soil thaw (c) show similar spatial patterns. The high variability patches in snowmelt result from intermittent snowfall.

AO-spring Correlations

To relate the winter AO to the timing of spring, we correlated the average AO index for JFM with the simulated date of leaf out, snowmelt, and soil thaw (Figure 27). Negative correlations indicate a spring advance (i.e., earlier spring) for positive AO polarity during JFM. Leaf out, which depends entirely on temperature, is well defined everywhere and bears the strongest resemblance to the AO temperature influence. Snowmelt and soil thaw do not occur south of the snow line (~40° N) in the southeast

United States, Northern Africa, and the Middle East and thus do not show the strong correlations with the AO as seen for leaf out.

(a) Leaf-Out

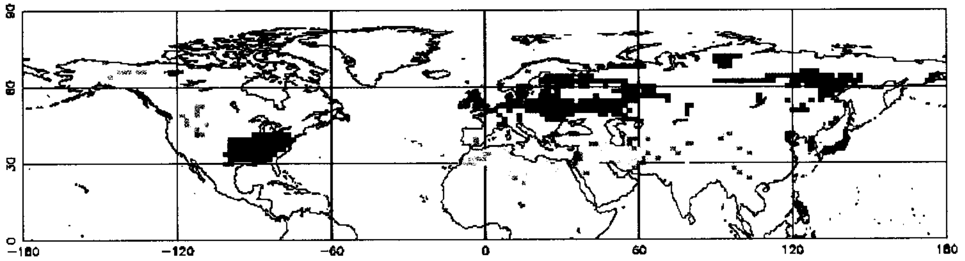

(b) Snowmelt

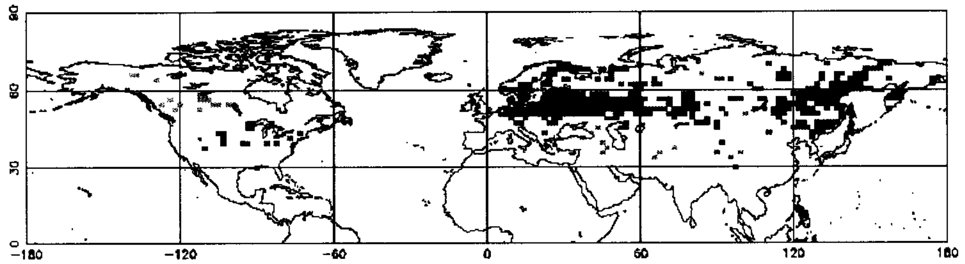

(c) Soil Thaw

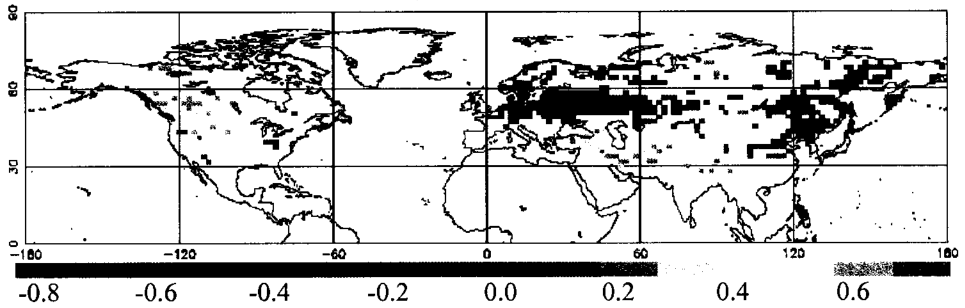

Figure 27. Correlations between the average January-February-March (JFM) AO index and simulated leaf-out (a), snowmelt (b), and soil thaw (c) all reflect the spatial pattern AO of temperature influence. Snowmelt and soil thaw do not correlate with the AO in the SE United States because they do not occur there. We omitted correlations failing the T-test at 95% significance.

Correlations with the winter AO increase with the climate memory of the variable defining spring. Strong climate memory integrates the conditions for the entire winter, effectively filtering the noisy climate signal from the AO (which has a characteristic time scale of 7-10 days). Snowmelt represents the integrated effects of snowfall vs. temperature for the entire winter season: increased snowfall delays snowmelt, while increased temperature advances snowmelt. Temperature effects dominate, but partial cancellation due to increased snow produces weaker correlations north of 55N latitude.

Soil thaw and snowmelt have nearly identical spatial correlation patterns because of the insulating effects of snow: the soil won't thaw until the snow melts.

(a) Canopy air temperature, T_{base}= 0° C (b) NCEP air temperature, T_{base}= 0° C

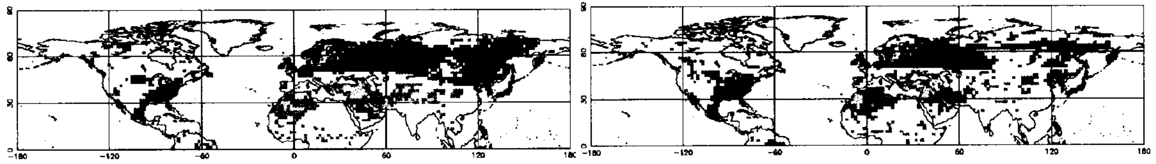

(c) Canopy air temperature, T_{base}= 5° C (d) NCEP air temperature, T_{base}= 5° C

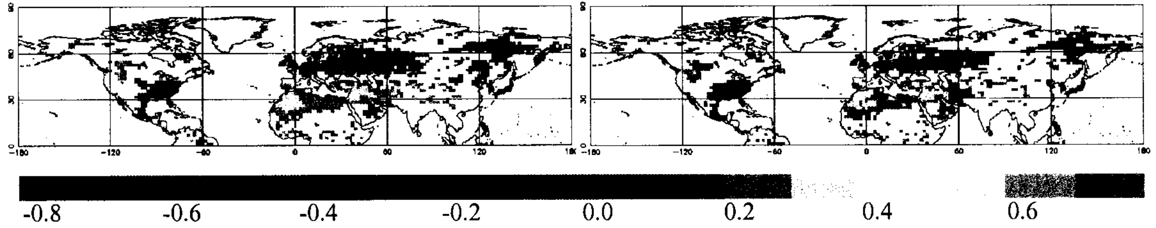

Figure 28. Correlations between the JFM AO index and simulated leaf out date for various combinations of temperature and T_{base} indicate climate memory determines the strength of the relationship with the winter AO. The thermal time to leaf out, S^*, was assumed constant at 100 ° C day. We omitted correlations failing the T-test at 95% significance.

The climate memory of the leaf out model depends on your choice of temperature, T_{base} and S^*. Figure 28 shows correlations between the JFM AO index and the simulated date of leaf out for various combinations of temperature and T_{base} assuming a constant S^* of 100 °C day. Figure 28a has the strongest climate memory and Figure 28d the weakest. Using the prognostic canopy air space temperature from SiB, which has a slightly longer climate memory than the NCEP surface air temperature, also produces stronger correlations with the JFM AO. A lower T_{base} or a higher S^* increases the number of days included in the thermal sum, increasing its climate memory, resulting in stronger correlations. Figure 28d has stronger correlations with the AO than Figure 27a because it was based on a larger value of S^* (100 °C day vs. 65-75 °C day). Some models use soil rather than air temperature [*White et al.*, 1997; *Tanja et al.*, 2003], although the influence of soil temperature on leaf out is small [*Cannell and Smith*, 1983]. Leaf out based on soil temperature correlates stronger with the AO than one based on air temperature because the heat capacity of soil is much greater than that of air, resulting in a greater thermal inertia and a longer climate memory (see below). Although the spatial pattern does not change, any choice of temperature, T_{base} and S^* that increases the climate memory of the leaf out model strengthens the correlations between estimated leaf out and the winter AO.

(a) Leaf-Out

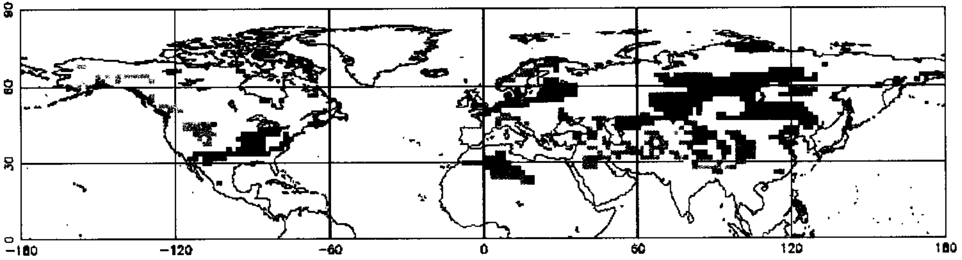

(b) Snowmelt

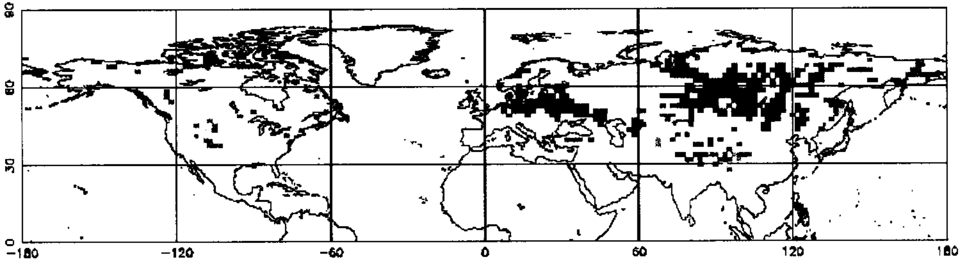

(c) Soil Thaw

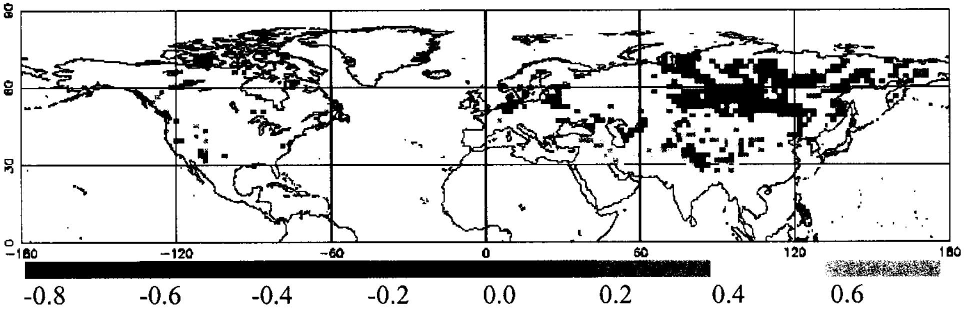

Figure 29. Simulated trends (day year^{-1}) in leaf-out (a), snowmelt (b), soil thaw (c) are generally negative and consistent with observations. The largest advances occur where the AO reduces precipitation and increases temperature. The trends are only statistically significant in regions where the variability is low. We omitted trends failing the T-test at 95% significance.

Spring Trends

Simulated trends in leaf out, snowmelt, and soil thaw (Figure 29) are consistent with observations. Positive trends indicate a delay in spring and negative trends indicate an advance. Estimated trends in leaf out are similar to observed trends in Europe [*Menzel and Fabian*, 1999; *Menzel*, 2000; *Ahas et al.,* 2002; *Scheifinger et al.,* 2002; *Menzel*, 2003] and North America [*Keyser et al.,* 2000; *Schwartz and Reiter*, 2000]. The snowmelt trends are consistent with the 0.3-0.5 days year^{-1} with peaks between 55-60N derived from NOAA snow charts [*Dye*, 2002]. The modeled snowmelt trends did not reflect observed delays in Siberia [*Stone et al.,* 2002].

The strongest trends occur in those regions that experience increased temperatures and neutral or decreased precipitation due to the AO. Snowmelt and soil do not show any trends in the southeast United States (as one might expect from a trend in the AO) because they are ill defined or do not occur there. For snowmelt, the southern margin shows large, statistically significant trends in Eurasia in spite of the huge variability in spring. However, these trends are suspect because our definition of snowmelt may not apply (it may not snow every year). The positive trends (later springs) along the southern margin for leaf out and soil thaw are consistent with lower temperatures due to the AO.

Comparing the simulated trends with the mean values (Figures 25 and 29) indicates the strongest trends primarily lie in regions where the mean date of spring occurs in April, May, and early June. These regions also correspond to regions of maximum trends in NDVI. The NDVI trends persist all year rather than peaking in spring only, suggesting the longer growing seasons promote the growth of woody plants with darker visible reflectances.

As expected, leaf out, snowmelt, and soil thaw trends correspond with the trends in surface air temperature from the NCEP data [*Serreze et al.,* 2000]. Which causes which is more difficult to determine, however. The air temperature trends may result from the snow-temperature feedback amplifying a relatively weak temperature signal [*Cutforth et al.,* 1999; *Hartley and Robinson*, 2000; *Serreze et al.,* 2000; *Shabanov et al.,* 2002; *Stone et al.,* 2002]. Warmer temperatures reduce snow cover, decreasing solar albedo, and increasing the absorbed solar radiation, which, in turn, increases air temperature. However, our simulation is diagnostic in nature with a weak snow-temperature feedback, so we could not accurately test its strength.

Comparing the simulated trends with the standard deviations (Figures 25 and 26) indicates the trends coincide with regions of relatively low variability in date of spring. This highlights the difficulty in identifying statistically significant trends from a noisy signal. Other regions in the high northern latitudes may, in fact, be experiencing trends towards earlier springs, but our 45-year simulation is too short to detect them.

To quantify the influence of the AO on spring trends, we defined the congruent trend as the fraction of the trend in spring due to the trend in the JFM AO index:

$$(46) \quad x = \left| r \frac{t_{ao}}{t_{spring}} \right|,$$

where x is the congruent trend, r is the regression coefficient between the JFM AO and spring (day per AO unit), t_{ao} is the trend in the average JFM index (AO unit per year), and t_{spring} is the trend in leaf out, snowmelt, or soil thaw (day per year) [*Thompson et al.,* 2000]. The congruent trend is statistically significant only where r, t_{ao}, and t_{spring} are all statistically significant (the overlap between Figure 27 and Figure 29). This limits where we can quantify the AO influence on the simulated trends to the eastern United States and northern Europe (Figure 30). In the eastern United States, the AO influence on leaf out trends varies between 40-70% (snowmelt and soil thaw are undefined). In northern Europe, the AO influence on leaf out, snowmelt, and soil thaw vary between 20-70%.

Evaluating broader regions requires longer simulations to increase the statistical significance of the estimated spring trends.

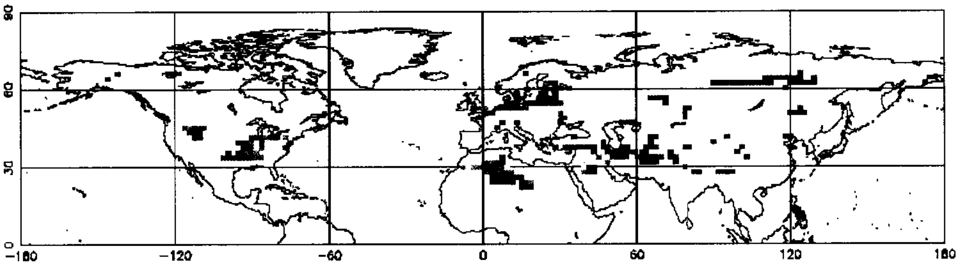
(b) Leaf out and JFM AO

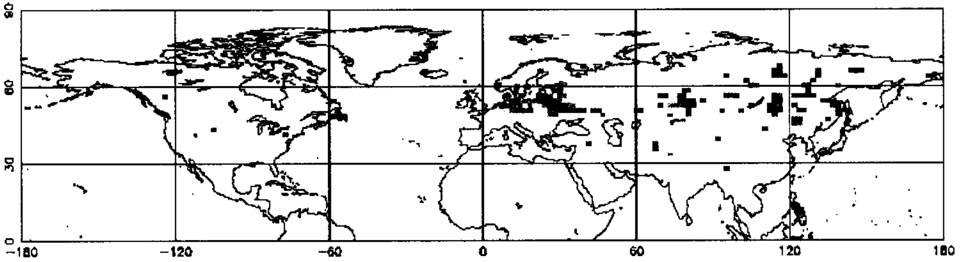
(c) Snow Melt and JFM AO

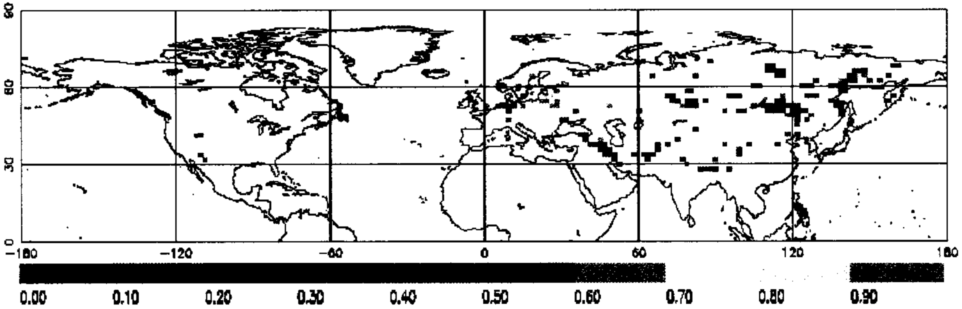
(c) Soil Thaw and JFM AO

Figure 30. The fraction of simulated leaf out (a), snowmelt (b), and soil thaw (c), trends congruent with the JFM AO trend is high where the AO has the strongest influence on temperature. Congruent trends are statistically significant only when the AO trend, the spring trend, and the correlation between spring and the AO are statistically significant.

Gross Primary Productivity

The winter AO can influence GPP directly through temperature control of enzyme kinetics, and indirectly by modulating the growing season length. The direct influence of the AO on simulated GPP appears very strong in March, for example, as illustrated by the strong correlations in Figure 31a. However, in March, much of Northern Hemisphere still lies in the grip of winter. Needleleaf, evergreen trees can photosynthesize even in winter [*Zimov et al.*, 1999], so SiB2 estimates a very small, but non-zero GPP that correlates well with the AO. Regression coefficients (Figure 31b) clearly indicate that although the correlations are strong, the magnitude of the direct AO influence is very small except in those areas where spring occurs in March. Although the AO exists all year [*Thompson and Wallace*, 2000], the direct influence of the AO on GPP is highest in winter when the AO is strongest. The spatial extent of direct AO influence expands southward in the fall as the AO builds up strength and contracts northward in the spring as it weakens.

(a) March AO and March GPP Correlations

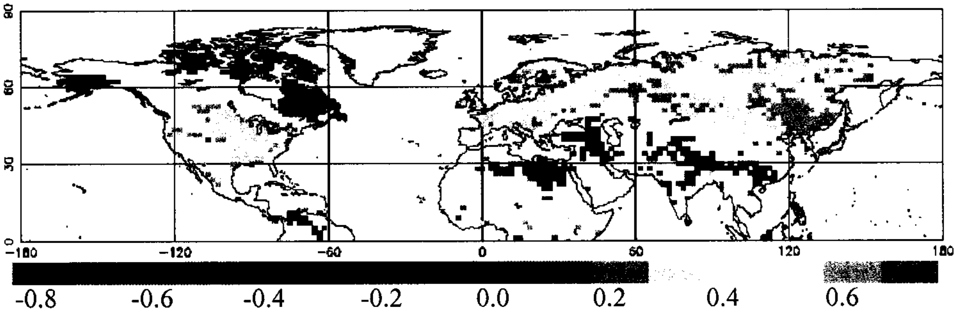

(b) March AO and March GPP Regressions (μmole m^{-2} s^{-1} AO-unit^{-1})

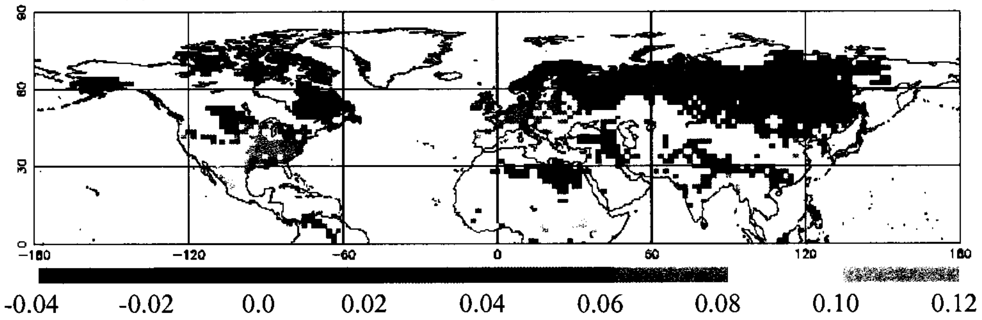

Figure 31. The March AO influences the simulated March GPP in where the AO influences temperature, as indicated by strong correlations in (a). The regression coefficients (b) indicate that although the correlations are strong, the magnitude of the AO influence is very small except in those areas where spring occurs in March. We omitted correlations and regressions failing the T-test at 95% significance.

The indirect influence of the winter AO on GPP through its control on the timing of spring is much greater than its direct influence through temperature. By influencing the timing of spring, the winter AO controls the start of the growing season. Earlier

(d) Jan-Jun GPP Correlations to JFM AO

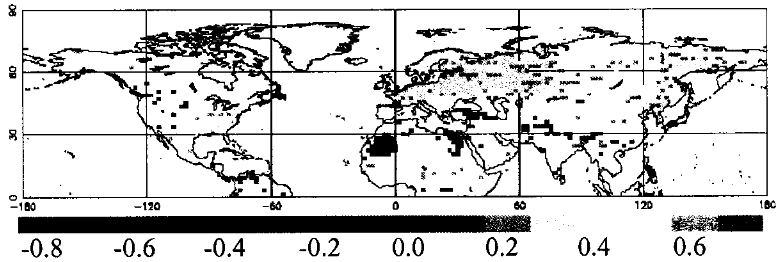

(a) Jan-Jun GPP Trends

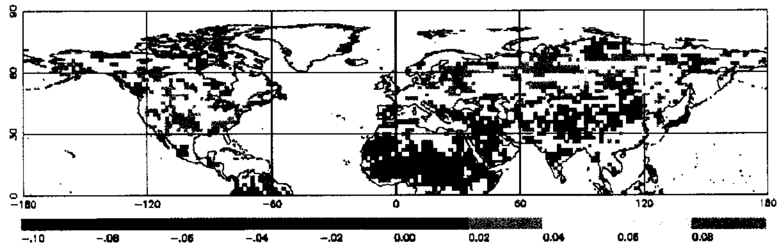

(c) Jan-Jun GPP trends Congruent to AO trend

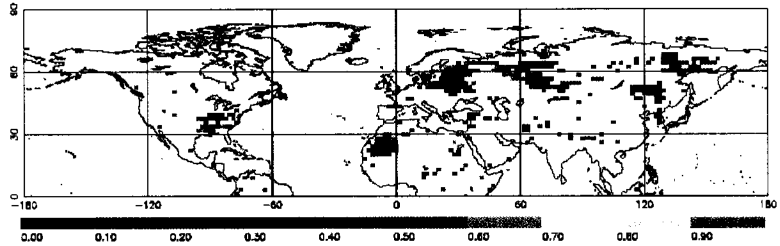

Figure 32. The total simulated GPP from January through June positively correlates with the average January-February-March AO index (a). Simulated Jan-Jun GPP trends (micromoles m^{-2} s^{-1} $year^{-1}$) show strong regional differences (b), but trends congruent with the JFM AO trend are consistent with the AO influence on temperature. We omitted values failing the T-test at 95% significance.

springs due to positive AO polarity in winter result in longer growing seasons and greater total GPP. The average JFM AO index correlates with total simulated GPP from January through June (Jan-Jun) where the winter AO most strongly influences winter temperature, and thus the timing of spring (Figure 32a). Using total annual GPP (full growing season) produces a similar spatial pattern (not shown), but much weaker correlations because the JFM AO influences the start, but not the end of the growing season. This indicates the drawdown period for [CO_2] in spring and early summer is modulated by the winter AO through its influence on the timing of spring.

The simulated trends in Jan-Jun GPP show some strong regional differences (Figure 32b), only some of which we can attribute to the AO. The large positive trends in western North America, for example, result from a long-term trend in annual precipitation unrelated to the AO (Respiration also shows a positive trend in the same region which cancels the GPP trend resulting in no trend in NEE). The fraction of Jan-Jun GPP trends congruent with the JFM AO trend (Figure 32c) indicate that the AO statistically accounts for 30-70% of the GPP trends in those regions where the AO exerts a strong influence on temperature and the timing of spring.

Respiration

Because soil has a large heat capacity, it retains the winter AO temperature signal, thus influencing spring and early summer respiration. Positive AO polarity in winter produces a positive soil temperature anomaly. Soil respiration increases with temperature, resulting in positive correlations with the AO. Correlations between the February AO index and simulated soil respiration (Figure 33) show a strong positive relationship in Eurasia and North America, consistent with the AO influence on temperature.

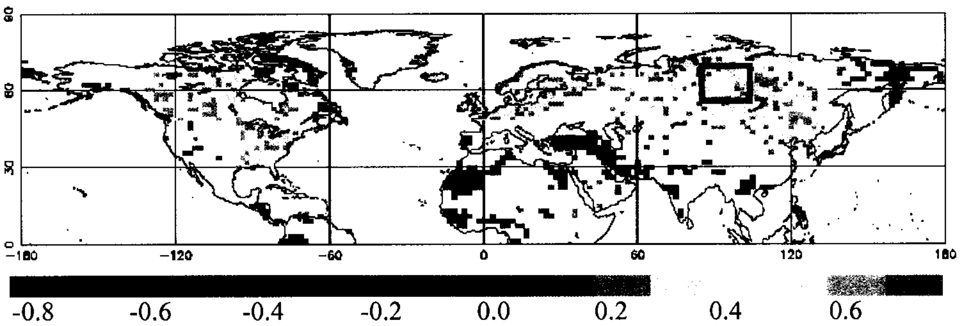

Figure 33: Correlations between the January AO index and simulated January respiration reflect the influence of the AO on temperature. We omitted correlations failing the T-test at 95% significance. The blue box is the area used in Figure 34.

The AO signal in simulated soil temperature persists for many months. Lagged correlations between the February AO and simulated soil temperatures in Siberia (Figure 34a) peak later at deeper depths as the AO-induced soil temperature anomaly sinks into the soil over a period of several months. The shallow soil layer temperatures are more responsive to atmospheric temperature forcing, so the correlations start strong and drop off within three months. The correlations for the middle soil layers start weak and increase as the AO driven temperature anomaly penetrates deeper into the soil. The lagged correlations persist longer at deeper depths because in SiB, soil layer thickness increases with depth and deeper layers have greater heat capacity. After four months, the winter AO temperature anomaly has reached the deepest soil layer in SiB (4 m). Although no longer felt at the surface, the AO soil temperature anomaly persists in the deepest soil layer for about 10 months. Correlations using December, January, or March AO indices give similar results (not shown).

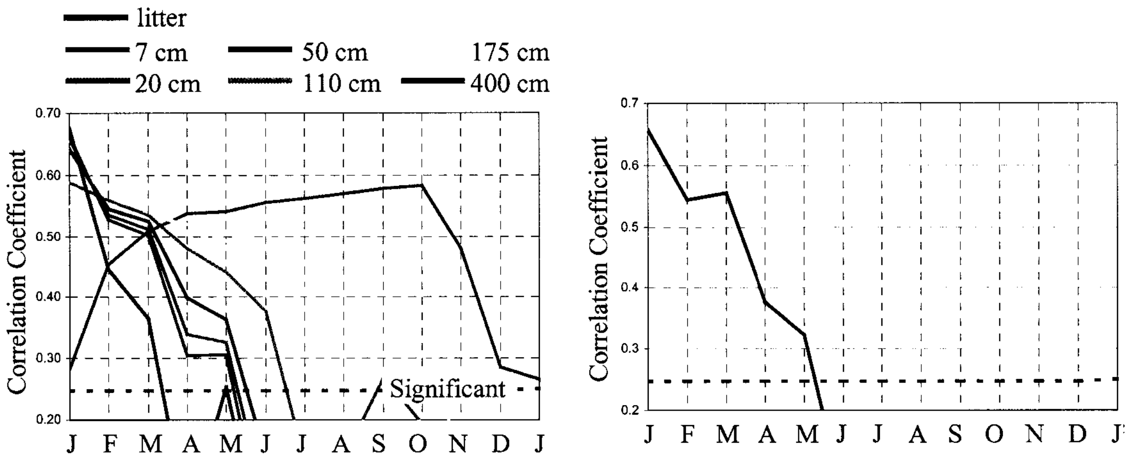

(a) Feb AO and Soil Temperature

(b) Feb AO and Respiration

Figure 34. Correlations between the February AO index and simulated soil temperature in Siberia (a) peak later at deeper depths, as the AO-induced temperature anomaly sinks into the soil. Correlations between the February AO index and simulated respiration in Siberia (b) drop off as the soil temperature anomaly sinks below the soil carbon. The AO temperature anomaly persists at depth, but its effect on respiration drops off by May.

SiB assumes root density, and thus soil carbon, decreases exponentially with depth [*Jackson et al.,* 1996], so the AO influence on respiration fades with time as the AO-induced temperature anomaly sinks below the soil carbon. Lagged correlations between the February AO index and simulated soil respiration in Siberia (Figure 34b) drop off completely by May because most of the soil carbon lies near the surface (95% in the top 1 m of soil). Comparing Figures 34a and 34b, we see that respiration correlations closely follow temperature correlations for the top 2 soil layers, which contain the bulk of the soil carbon. Although winter AO temperature anomalies may persist at depth well into summer, the effect on respiration is limited to spring and early summer.

NEE and [CO$_2$] Amplitude

Our simulation does show seasonally asymmetric trends in NEE which could help explain the [CO$_2$] amplitude trend (Figure 35). Summer (June, July, and August or JJA) shows large positive trends in NEE due almost entirely to trends towards increased respiration in August. Spring (March April, and May or MAM) shows large decreases in NEE due to increased GPP. Fall (September, October, and November or SON) show no significant trends. Winter (December, January, and February or DJF) shows increased NEE north of 55N and decreased NEE south of 55N due to changes in respiration.

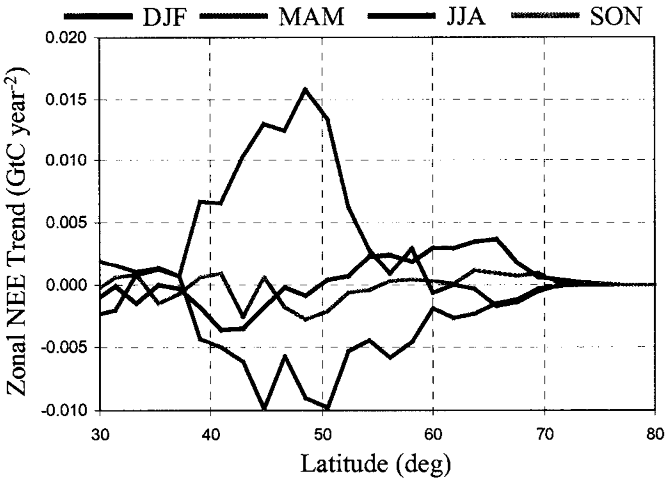

Figure 35. The simulated, total zonal NEE shows strong seasonally asymmetric trends between 40-55N. The December-January-February trends result from changes in respiration due to the AO. The negative trends in March-April-May (MAM) result from increased GPP due to earlier springs due to the AO. The positive trends in June-July-August (JJA) result from increased respiration not associated with the AO.

The trends in the DJF AO can statistically explain 50-70% of the trends in simulated DJF NEE in Siberia. Increased temperatures due to positive DJF AO polarity increase respiration, and thus NEE, resulting in positive correlations with simulated NEE across Eurasia (Figure 36a). The DJF NEE trends are generally positive throughout the northern hemisphere, consistent with increased [CO$_2$] amplitude.

(a) DJF AO to NEE Correlations

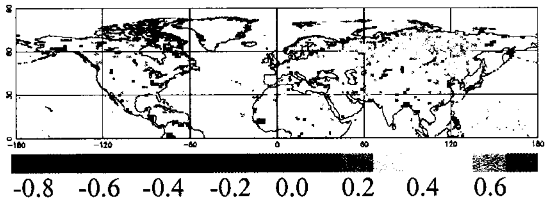

(b) DJF NEE trends (μmole m^{-2} s^{-1} $year^{-1}$)

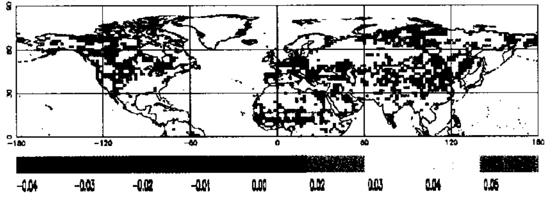

(c) DJF NEE trends Congruent to JJA AO

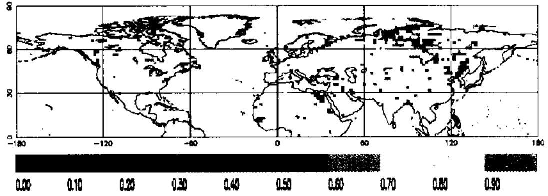

Figure 36. Increased temperatures due to positive AO polarity in December, January, and February (JFM) increase winter respiration, resulting in positive correlations with simulated DJF NEE across Eurasia (a). Trends in simulated DJF NEE (μmoles m^{-2} s^{-1} $year^{-1}$) are generally positive throughout the northern hemisphere (b). The DJF AO can statistically explain DJF NEE trends in Siberia (c). We omitted trends and correlations failing the T-test at 95% significance.

(a) Leaf out to MAM NEE Correlations

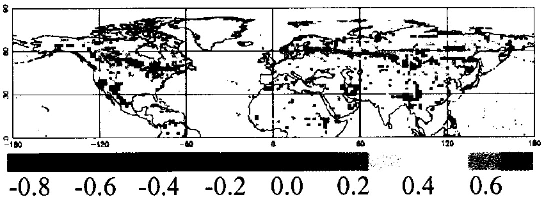

(b) MAM NEE trends (μmole m^{-2} s^{-1} $year^{-1}$)

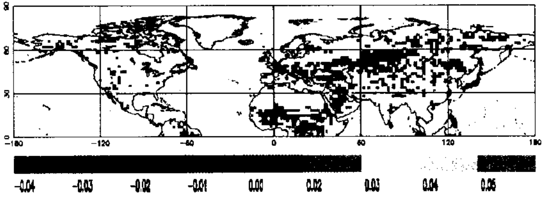

(c) MAM NEE trends Congruent to Leaf out

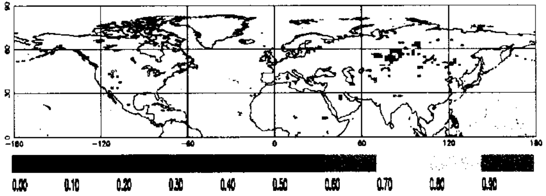

Figure 37. The simulated NEE for March, April, and May (MAM) correlates with leaf out in those regions where spring occurs in May (a), while the NEE trends (μmoles m^{-2} s^{-1} $year^{-1}$) occur primarily in those regions where spring occurs in March and April (b). Leaf out can explain the MAM NEE trends in central Asia (c). We omitted trends and correlations failing the T-test at 95% significance.

The simulated MAM NEE correlates well with the date of leaf out in those regions where leaf out occurs primarily in May (Figure 37). Increases in respiration that occur simultaneously with leaf out tend to cancel the increases in GPP, resulting in weaker correlations in those regions where spring occurs in March and April. The trends in MAM NEE are generally negative (consistent with increased GPP due to earlier spring) and are strongest in those regions where spring occurs in March and April. As explained above, these regions do not show statistically significant trends in leaf out. Nevertheless, trends in leaf out associated with trends in the winter AO can explain trends in MAM NEE in central Asia.

(a) August AO to NEE Correlations

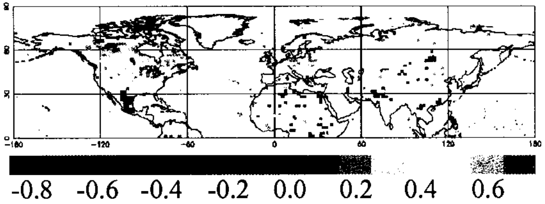

(b) August NEE trends (μmole m^{-2} s^{-1} $year^{-1}$)

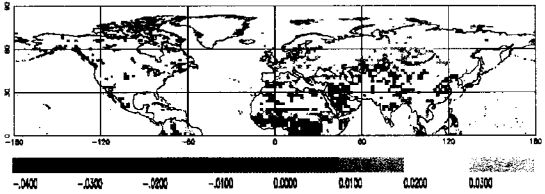

(c) August NEE trends Congruent to Aug AO

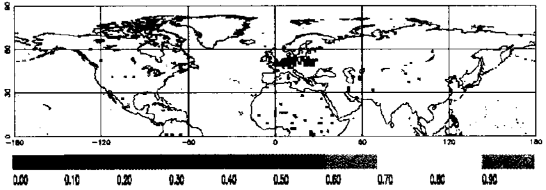

Figure 38. Simulated NEE in August correlates with the August AO index in North America and Europe (a), while the NEE trends (μmoles m^{-2} s^{-1} $year^{-1}$) occur primarily in Eurasia (b). The AO can statistically explain only the NEE trends in Europe (c). We omitted trends and correlations failing the T-test at 95% significance.

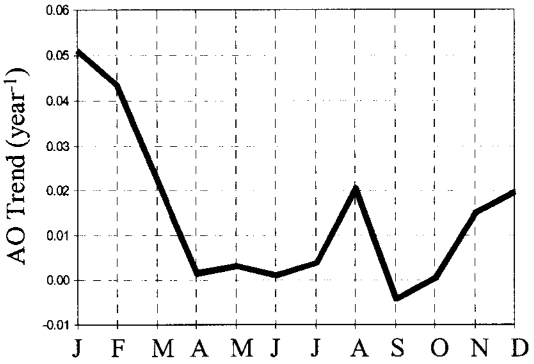

Figure 39. The AO index shows a statistically significant trend in August, although the strongest trends are in winter.

The August AO does influence NEE, but the trends in respiration appear unrelated to the AO. The August AO influences the surface air temperature in North America, but its influence in Eurasia is limited to small regions near the Atlantic coast. Figure 38 shows that the August AO correlates well with the simulated NEE in North America, but very weakly in Eurasia. Positive AO polarity produces positive temperature anomalies in North America, increasing respiration and resulting in positive NEE anomalies (Correlations with surface air temperature and respiration have very similar magnitudes and spatial patterns). As shown in Figure 39, the August AO index has a statistically significant, positive trend (about 40% of the winter AO trend). However, the temperature trends, which closely match the NEE trends in Figure 38b, are not consistent with that expected from a positive trend in the August AO.

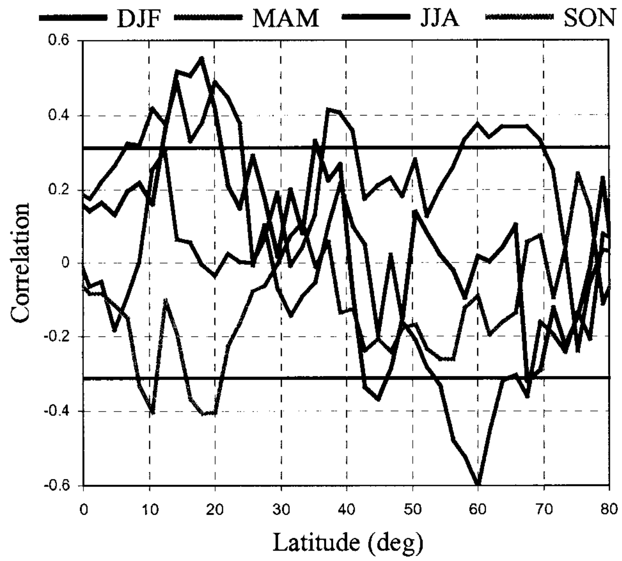

Figure 40. The correlations between simulated, total zonal NEE and the observed Barrow [CO2] seasonal amplitudes from flasks are consistent with an AO influence in spring (MAM), but not summer (JJA). The black horizontal lines indicate statistical significance.

Correlations between simulated, zonal total NEE and observed [CO_2] amplitudes based on flask measurements are consistent with the seasonally asymmetric trends in NEE (Figure 40). While many of the flask sites show trends towards increased seasonal [CO_2] amplitudes, only the Barrow, Alaska site had a sufficiently long enough record (1972-2002) to pass a statistical significance test. Correlations with DJF total zonal NEE were not statistically significant, so we could draw no firm conclusion about how the winter fluxes influence the [CO_2] amplitude at Barrow. Negative correlations in MAM zonal NEE at about 60N latitude indicate that increased GPP in spring (negative NEE anomalies) increases the [CO_2] amplitude at Barrow. Positive correlations with JJA zonal NEE indicate increased respiration in summer results in increased [CO_2] amplitude at Barrow.

Our results indicate that variability in NEE due to the AO can explain some of the variability in the [CO_2] amplitude. The NEE shows seasonally asymmetric trends consistent with the observed trend in the [CO_2] amplitude. The trends in MAM NEE can be attributed to the trend towards earlier springs due to the trend in the winter AO. The trends towards increased DJF NEE result from the winter AO trend, but the flask record is too short to make a statistically significant link with the [CO_2] amplitude trend. The respiration increases in August contribute to the observed variability and trends in the [CO_2] amplitude, but are not strongly associated with the August AO trend.

Our results support the *Idso et al.,* [1999] theory that seasonally asymmetric fluxes can change the [CO_2] seasonal cycle. We found that the timing of maximum and minimum NEE showed little, if any, inter-annual variation and trends, indicating that the timing peak photosynthesis did not change and cannot explain the amplitude trends, as proposed by *Chapin et al.,* [1996] and *Stone et al.,* [2002]. We did not include a transport model in our simulations, but our analysis indirectly supports the shifting source region theory proposed by *Dargaville et al.,* [2000] by linking some of the amplitude change to a trend in winter circulation. The [CO_2] seasonal cycle has climate memory because it integrates the cumulative NEE throughout the year. Consequently, the source region for the [CO_2] seasonal cycle may encompass most of the northern hemisphere, much larger than the source region for a single flask measurement. Evaluating shifting source regions requires a detailed analysis of NEE using a transport model.

AO and NDVI

Observed NDVI trends from the FASIR dataset show a consistent spatial pattern all year round (Figure 41), although the trends in spring (March, April, and May or MAM) are approximately double the annual average. As seen with the trends in leaf out, the NDVI trends are statistically significant only in regions of relatively low variability. The winter AO index correlates with the MAM NDVI in Europe, where the AO has the strongest influence on temperature and the timing of spring (Figure 42a). Positive AO polarity results in earlier spring and positive NDVI anomalies. As one might expect, the MAM NDVI also strongly correlate with the simulated date of spring throughout the northern hemisphere (Figure 42b). Earlier springs result in positive NDVI anomalies and, thus negative correlations.

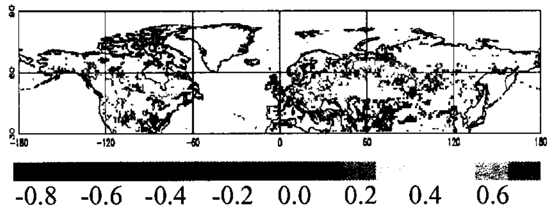

Figure 41. Observed NDVI trends (NDVI unit year^{-1} x 100) from the FASIR dataset show a consistent spatial pattern all year round. Trends in spring (March-April-May) are approximately double the annual average. Trends failing the T-test at 95% significance are omitted.

(a) JFM AO to MAM NDVI Correlations

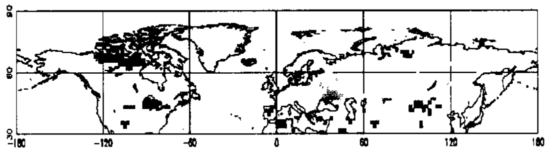

(b) Leaf Out to MAM NDVI Correlations

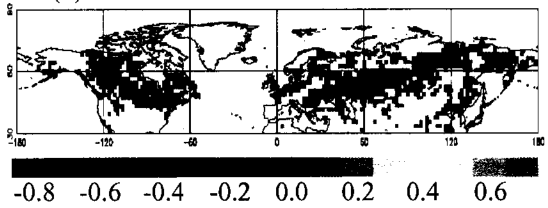

Figure 42. The MAM FASIR NDVI correlates with the JFM AO index (a) and with the simulated date of leaf out (b), but the AO and leaf out trends are not statistically significant. Correlations failing the T-test at 95% significance are omitted.

Unfortunately, the NDVI time series is not long enough to statistically assess how much of the NDVI trends result from the trend in the winter AO. The JFM AO does not have a statistically significant trend over the 17-year time period covered by the FASIR NDVI (1982-1998). The simulated leaf out shows some statistically significant trends, but at far fewer points than seen in Figure 29. Without statistically significant trends, we could not estimate congruent trend fractions with either the JFM AO or the date of leaf out. Our analysis, therefore, is inconclusive.

5.3 Conclusions

The winter AO directly influences GPP and R through its influence on air temperature. The soil retains the temperature signal of the winter AO for many months, influencing respiration fluxes well into spring. By controlling the start of the growing season, the AO influences the total GPP during spring and early summer, the drawdown period for [CO_2].

Our modeling results indicate that the trend in the winter AO can help explain observed trends towards earlier leaf out and snowmelt. The modeled leaf out and snowmelt trends are consistent with observed trends. The trends are also consistent with the NDVI trends. The AO shows a statistically significant influence on spring trends in the eastern United States and northern Europe. Increased GPP due to earlier springs increases the amplitude of the NEE seasonal cycle, partially explaining the increase in [CO_2] amplitude.

We found that the components of the terrestrial biosphere with climate memory (plant buds, snow pack, and soil temperature) integrate the noisy AO signal over time to control the transition from winter to spring. In general, positive AO polarity during winter results in positive winter temperature anomalies and earlier springs. The climate memory of plant buds, snow pack, and soil temperature will also respond to a trend in climate: a trend towards positive AO polarity produces a trend towards warmer temperatures and earlier springs.

Our analysis also indicates that the observed springtime trends can be partially explained by changes in circulation rather than as direct effects of global warming. Although the exact mechanism is not fully understood, the winter AO trend itself may result from global warming, stratospheric ozone loss, or both [*Hartmann et al.,* 2000; *Hoerling et al.,* 2001; *Shindell et al.,* 2002]. Alternatively, the winter AO trend may result from natural variability of the atmosphere on a century time scale. Indeed, our modeled trends were statistically significant only in regions of relatively low variability. Although our modeled spring trends generally agree with observations, the observed trends are no larger than inter-decadal variability [*White et al.,* 1999; *Serreze et al.,* 2000]. Trends in spring may reflect natural climate variability rather than climate change [*Hartley and Robinson*, 2000].

Our analysis raises new questions concerning the interaction between large-scale circulation phenomena and the terrestrial biosphere. For example, could the trend in winter AO explain observed trends in autumn phenophases? What is the joint influence of the AO and El Nino-Southern Oscillation (ENSO) on the trends in the northern hemisphere? ENSO statistically explains 16% of the winter temperature variance (about half that of the AO) and has drifted towards a negative index, warming northern North America [*Hartley and Robinson*, 2000; *Serreze et al.,* 2000] and advancing spring phenophases in central Canada [*Cutforth et al.,* 1999; *Beaubien and Freeland*, 2000]. ENSO correlates with [CO_2] [*Braswell et al.,* 1997] and with NDVI [*Los et al.,* 2001; *Shabanov et al.,* 2002]. Long simulations such as ours using a highly mechanistic model driven by reanalysis weather provide an excellent tool for analyzing long-term interactions between the atmospheric circulation and the terrestrial biosphere.

6. Conclusions and Discussion

6.1 Conclusions

Hypothesis 1: the climate influence on NEE has strong regional differences.

We hypothesized that climate influences on NEE inter-annual variability have strong regional differences. We found that temperature influence on respiration dominates NEE inter-annual variability in the extra-tropics while precipitation influence on *GPP* and *R* dominates in the tropics. In tropical regions with drier soils, precipitation control of photosynthesis (i.e., drought stress) dominates. In nearly saturated soils, precipitation control of respiration dominates. The demarcation between precipitation control of *GPP* and *R* is the line where the average soil moisture is near W_{opt}, the optimal soil moisture for respiration.

Hypothesis 2: ENSO influences NEE in the tropics

We hypothesized that ENSO influences NEE in the tropics. We found that the influence of ENSO on NEE inter-annual variability is consistent with that expected for shifting precipitation patterns in the tropics. The short time period of our simulation (11 years) precludes any definitive assessment.

Hypothesis 3: the AO influences NEE in the high northern latitudes

We hypothesized that the Arctic Oscillation (AO) influences NEE inter-annual variability in the high northern latitudes. We found that the AO shows a fairly strong influence on autumn, winter, and spring NEE through its influence on temperature. Positive AO polarity indicates positive temperature anomalies, increased respiration, and thus positive NEE anomalies. The positive temperature anomalies produce positive GPP anomalies and negative NEE anomalies in those regions where spring occurs in March and April. The influence of the AO on summer NEE is minimal except for North America in August.

Hypothesis 4: Climate memory allows the winter AO to influence spring NEE

We hypothesized that elements of the land surface have sufficient climate memory such that the winter AO influences variability in spring and early summer NEE. The winter AO temperature signal persists for many months in the soil, but its' influence on respiration drops off by May as the AO temperature anomaly sinks below the soil carbon. We also found that the winter AO influences the total amount of GPP in spring and early summer through its influence on the timing of spring. Positive AO polarity results in earlier springs and greater total GPP.

Hypothesis 5: the winter AO influences variability and trends in the timing of spring

We hypothesized that the winter AO, through its influence on temperature and precipitation, influences the timing of spring in the northern hemisphere. We found that those elements of the land system with climate memory (plant buds, snow pack, and soil temperature) integrate the noisy AO signal over time to control the transition from winter to spring. The winter AO influences the timing of spring in those regions where the AO exerts the strongest influence on temperature: Eurasia and southeast United States. Leaf out, snowmelt, and soil thaw all show the same patterns of influence with the strength of the correlations increasing with increased climate memory. The winter AO does not explain variability in the date of spring in the boreal regions of North America.

We hypothesized that the trend in the winter AO are related to observed trends towards earlier leaf out and snowmelt over large areas in the northern hemisphere. We found that the modeled trends in leaf out, snowmelt, and soil thaw are consistent with observations. The trends toward earlier spring in southeast United States and Europe appear statistically related to the trend towards positive AO polarity in winter.

Hypothesis 6: The winter AO influences variability and trends in the [CO_2] seasonal amplitude

We hypothesized that winter AO influences inter-annual variability in the [CO_2] seasonal amplitude by simultaneously increasing winter respiration and spring GPP, thus resulting in a greater [CO_2] seasonal amplitude. We found that positive AO polarity result in positive temperature anomalies that increase the winter buildup of atmospheric CO_2 by increasing respiration and increase spring drawdown by increasing GPP, particularly in March. We also found that positive AO polarity in winter advances the start of the growing season, increasing total GPP in spring and early summer and thus the total atmospheric CO_2 drawdown.

We hypothesized that seasonally asymmetric trends in NEE caused by the trend in the winter AO towards positive polarity is related to the observed trend towards larger [CO_2] seasonal amplitudes. We found that the climate trends in the NCEP reanalysis do produce seasonally asymmetric trends in NEE. The winter trends towards increased respiration are consistent with increased temperatures due to the AO. The strong trends towards increased respiration in August are not related to the August trend towards positive AO polarity. The trends towards increased GPP in spring are partially explained by the trends in the winter AO, both directly, through temperature, and indirectly by advancing the start of the growing season.

Hypothesis 7: The winter AO trend is related to NDVI trends

We hypothesized that observed trends towards brighter NDVI is related to the trend towards positive AO polarity in winter. The NDVI is strongly correlated with the date of spring. However, Our analysis is inconclusive because the NDVI time record is too short to estimate statistically significant trends in either the AO or the date of leaf out.

6.2 Discussion

A highly mechanistic model like SiB2 driven by realistic weather is a useful tool in analyzing the relationship between climate and NEE inter-annual variability. The process information in SiB2 allows us to understand the exact mechanisms whereby climate variability influences NEE variability. We can isolate exactly how large-scale atmospheric phenomena influence NEE.

Climate memory is important in understanding the seasonal dynamics that drive the global carbon cycle. Those elements of the land system with climate memory (soil, snow, and plants) control the transition between seasons, and thus the global carbon cycle. The indirect influence of the AO on NEE variability through climatic memory is as great or greater than the direct influence through temperature and precipitation. Climatic memory is a useful paradigm for understanding how climate variability influences seasonal dynamics of the carbon cycle.

6.3 Future Research

The long simulations created for this research represent a great resource for the study of NEE variability at a variety of time scales. We focused on how a synoptic scale phenomenon (the AO) can influence NEE on seasonal and decadal time scales. We answered a small subset of questions concerning the interplay between climate dynamics and the global carbon cycle. Many other questions remain unanswered or even unasked.

Other Atmospheric Phenomena

Many atmospheric phenomena in addition to the AO and ENSO have strong regional influences on climate, which would, in turn, influence NEE. Future research could investigate the relationship between these phenomena and NEE. For example, the Pacific-North America pattern also influences climate in North American and should be studied for its effect on NEE. Future research should explain why the Madden-Julian Oscillation, which influences precipitation and temperatures in the tropics, correlates strongly with spring NEE in the northern hemisphere. Understanding how these and other climate phenomena influence NEE provide a strong theoretical basis to explain the observed variability in the missing carbon sink.

Future research should attempt to explain the strong correlations when NEE lag the [CO_2] growth rate by two years. Similar correlations are observed when the [CO_2] amplitude and NDVI lag temperature by two years [*Keeling et al.*, 1995; *Keeling et al.*, 1996; *Idso et al.*, 1999; *Los et al.*, 2001].

Seasonal dynamics

Many questions about how climatic memory influences seasonal dynamics remain unanswered. For instance, the spring variability and trends are not fully explained. Future research should include an analysis of how ENSO and other atmospheric phenomena influence the timing of spring in the northern hemisphere, especially in North America. We have not addressed the transition from autumn to winter. Future research should include an analysis of fall events, which show mixed trends indicating strong regional differences.

Model Improvements

Our analysis has identified several model improvements that should improve our estimates of NEE. Using observed leaf out for many more species than just the 15 species of trees and bushes in Europe would improve our estimated date of leaf out. Incorporating more detailed biogeochemistry would provide better estimates of respiration. Including the effects of land use change, CO_2 fertilization, and nitrogen deposition would improve the ability of SiB2 to locate and understand the mechanisms behind the missing carbon sink.

Detailed Comparison with Observations

A logical follow-on study would compare our modeled results directly to observations. The observations should include snowmelt dates, leaf out dates, soil temperatures, $[CO_2]$ amplitudes, and NEE from flux towers. The reanalysis is optimally consistent with observations, but nothing beats comparisons with actual data.

Expansion

Future research should expand the scope of our analysis to include other factors that influence the global carbon cycle. Including a model of ocean fluxes would allow direct comparison between land and ocean flux variability to test the fundamental assumption that the ocean fluxes are not as variable as the land fluxes. Adding atmospheric transport would allow direct comparison between modeled and observed $[CO_2]$ and a more thorough assessment of the $[CO_2]$ amplitude trend.

7. References

Ahas, R., A. Aasa, A. Menzel, V. G. Fedotova, and H. Scheifinger, Changes in European spring phenology, International Journal of Climatology, 22, 1727-1738, 2002.

Baker, I.T., A.S. Denning, N. Hanan, L. Prihodko, P. L. Vidale, K. Davis and P. Bakwin, Simulated and observed fluxes of sensible and latent heat and CO2 at the WLEF-TV Tower using SiB2.5, Global Change Biology, Submitted, 2003.

Ball, J. T., An analysis of stomatal conductance, Ph.D. Thesis, Stanford University, 1988.

Barber, V. A., G. P. Juday, and B. P. Finney, Reduced growth of Alaskan white spruce in the twentieth century from temperature-induced drought stress, Nature, 405(6787), 668-673, 2000.

Beaubien, E. G., and H. J. Freeland, Spring phenology trends in Alberta, Canada: links to ocean temperature, International Journal of Biometeorology, 44, 53-59, 2000.

Bonan, Gordon B., A Land Surface Model (LSM Version 1.0) for Ecological, Hydrological, and Atmospheric Studies: Technical Description and Users Guide, NCAR Technical Note NCAR/TN-417+STR, Boulder Colorado, 1996.

Bousquet, P, P. Peylin, P. Ciais, C. Le Quere, P. Friedlingstein, and P.Tans, Regional changes in carbon dioxide fluxes of land and oceans since 1980, Science, 290(5495), 1342-1346, 2000.

Braswell, B. H., D. S. Schimel, E. Linder, and B. Moore, The response of global terrestrial ecosystems to interannual temperature variability, Science, 278(5339), 870-872, 1997.

Cannell, M. G. R., and R. I. Smith, Thermal time, chill days, and prediction of budburst in picea sitchensis, Journal of Applied Ecology, 20, 951-963, 1983.

Cannell, M. G. R. and R. I. Smith, Climatic warming, spring budburst, and frost damage on trees, Journal of Applied Ecology, 23, 177-191, 1986.

Chapin, F. S., S. A. Zimov, G. R. Shaver, and S. E. Hobbie, CO2 fluctuation at high latitudes, Nature, 383(6601), 585-586, 1996.

Chen, X. Q., and W. F. Pan, Relationships among phenological growing season, time-integrated normalized difference vegetation index and climate forcing in the temperate region of eastern China, International Journal of Climatology, 22(14), 1781-1792, 2002.

Chuine, I., A unified model for budburst of trees, Journal of Theoretical Biology, 207, 337-347, 2000.

Clapp, Roger B.; Hornberger, George M., Empirical Equations for Some Soil Hydraulic Properties, Water Resources Research, 14(4), 601-604, 1978.

Collatz, G. J., J. T. Ball, C. Grivet, and J. A. Berry, Physiological and Environmental Regulation of Stomatal Conductance, Photosynthesis, and Transpiration: A Model that Includes a Laminar Boundary Layer, Agricultural and Forest Meteorology, 54, 107-136, 1991.

Collatz, G. J., M. Ribascarbo, and J. A. Berry, Coupled Photosynthesis-Stomatal Conductance Model for Leaves of C4 Plants, Australian Journal of Plant Physiology, 19(5), 519-538, 1992.

Conway, T. J., P. P. Tans, L. S. Waterman, K. W. Thoning, D. R. Kitzis, K. A. Masarie, and N. Zhang, Evidence for Interannual Variability of the Carbon Cycle from the National Oceanic and Atmospheric Administration/Climate Monitoring and Diagnostics Laboratory Global Air Sampling Network, Journal of Geophysical Research, 99(D11), 22,831-22,855, 1994.

Costa, M. H., and J. A. Foley, A Comparison of Precipitation Datasets for the Amazon Basin, Geophysical Research Letters, 25(2), 155-158, 1998.

Craig, S. G., K. J. Holmén, G. B. Bonan, and P. J. Rasch, Atmospheric CO2 simulated by the National Center for Atmospheric Research Community Climate Model. 1. Mean fields and seasonal cycles, Journal of Geophysical Research, 13213-13235, 1998.

Cutforth, H. W., B. G. McConkey, R. J. Woodvine, D. G. Smith, P. G. Jefferson, and O. O. Akinremi, Climate change in the semiarid prairie of southwestern Saskatchewan: Late winter-early spring, Canadian Journal of Plant Science, 79(3), 343-350, 1999.

D'Odorico, P., J. Yoo, and S. Jaeger, Changing seasons: an effect of the North Atlantic Oscillation?, Journal of Climate, 15, 435-445, 2002.

Dargaville, R. J., R. M. Law, and F. Pribac, Implications of interannual variability in atmospheric circulation on modeled CO2 concentrations and source estimates, Global Biogeochemical Cycles, 14(3), 931-943, 2000.

Defries, R. S. and J. R. G. Townshend, NDVI-derived land cover classification at a global scale, International Journal of Remote Sensing, 15(17), 3567-3586, 1994.

Denning, Scott A., Investigations of the Transport, Sources, and Sinks of Atmospheric CO2 Using a General Circulation Model, Colorado State University, (564), 1995.

Denning, A. S., G. J. Collatz, C. Zhang, D. A. Randall, J. A. Berry, P. J. Sellers, G. D. Colello, and D. A. Dazlich, Simulations of Terrestrial Carbon Metabolism and Atmospheric CO2 in a General Circulation Model Part 1 Surface Carbon Fluxes, Tellus, 48, 521-542, 1996.

Denning, A. Scott; Randall, David A.; Collatz, G. James; Sellers, Piers J., Simulations of Terrestrial Carbon Metabolism and Atmospheric CO2 in a General Circulation Model Part 2: Simulated CO2 Concentrations, Tellus, 48, 543-567, 1996.

Denning AS, Nicholls M, Prihodko L, Baker I, Vidale PL, Davis K, Bakwin P, Simulated variations in atmospheric CO2 over a Wisconsin forest using a coupled ecosystem-atmosphere model, Global Change Biology, 9(9), 1241-1250, 2003.

Devore, J. L., Probability and Statistics for Engineering and the Sciences, Duxbury Press, 1995.

Dickinson, R. E., How coupling of the Atmosphere to ocean and Land Helps Determine the Timescales of Inter-annual Variability of Climate, Journal of Geophysical Research, 105(D15), 20,115-20,119, 2000.

Dye, D. G., Variability and trends in the annual snow-cover cycle in Northern Hemisphere land areas, Hydrological Processes, 16(15), 3065-3077, 2002.

Farquhar, G. D., S. von Caemmerer, and J. A. Berry, A Biochemical Model of Photosynthetic CO2 Assimilation in Leaves of C3 Species, Planta, 149, 78-90, 1980.

Fung, I., Variable Carbon Sinks, Science, 290, 1313, 2000.

Gibson, J. K., S. Uppala, P. Kållberg, M. Fiorino, A. Hernandez, K. Onogi, and X. Li, ECMWF 40-year Re-Analysis (ERA-40) - Archive Plans, European Centre For Medium-Range Weather Forecasts, 1999.

Goetz, S. J., S. D. Prince, J. Small, and A. C. R. Gleason, Interannual Variability of Global Terrestrial Primary Production: Results of a Model Driven with Satellite Onservations, Journal of Geophysical Research, 105(D15), 20,077-20,091, 2000.

Green, P.M., D. M. Legler, C. J. Miranda V, and J. J. O'Brien, The North American Climate Patterns Associated with El Nino-Southern Oscillation, Center for Ocean-Atmospheric Prediction Studies, Project Report Series 97-1, 1997.

Hartley, S., and D. A. Robinson, A shift in winter season timing in the Northern Plains of the USA as indicated by temporal analysis of heating degree days, International Journal of Climatology, 20(4), 365-379, 2000.

Hartmann, D. L., J. M. Wallace, V. Limpasuvan, D. W. J. Thompson, and J. R. Holton, Can ozone depletion and global warming interact to produce rapid climate change?, Proceeding of the National Academy of Sciences of the United States of America, 97(4), 1412-1417, 2000.

Hicke, J. A., G. P. Asner, J. T. Randerson, C. Tucker, S. Los, R. Birdsey, J. C. Jenkins, C. Field, and E. Holland, Satellite-derived increases in net primary productivity across North America, 1982-1998, Geophysical Research Letters, 29(10), 1427, 2002.

Hicke, J. A., G. P. Asner, J. T. Randerson, C. Tucker, S. Los, R. Birdsey, J. C. Jenkins, and C. Field, Trends in North American net primary productivity derived from satellite observations, 1982-1998, Global Biogeochemical Cycles, 16(2), art. no. 1019, 2002.

Higuchi, K., S. Murayama, and S. Taguchi, Quasi-decadal variation of the atmospheric CO2 seasonal cycle due to atmospheric circulation changes: 1979-1998, Geophysical Research Letters, 29(8), art. no. 1173, 2002.

Hoerling, M. P., J. W. Hurrell, and T. Xu, Tropical origins for recent North Atlantic climate change, Science, 292, 90-92, 2001.

Houghton, R. A., Interannual variability in the global carbon cycle, Journal of Geophysical Research, 105(D15), 20121-20130, 2000.

Houghton, R. A., E. A. Davidson, and G. M. Woodwell, Missing sinks, feedbacks, and understanding the role of terrestrial ecosystems in the global carbon balance, Global Biogeochemical Cycles, 12(1), 25-34, 1998.

Hunter, A. F., and M. J. Lechowicz, Predicting the timing of budburst in temperate trees, Journal of Applied Ecology, 29(3), 597-604, 1992.

Ichii, K., Y. Matsui, Y. Yamaguchi, and K. Ogawa, Comparison of Global Net Primary Production Trends Obtained From Satellite-Based Normalized Difference Vegetation Index and Carbon Cycle Model, Global Biogeochemical Cycles, 15(2), 351-363, 2001.

Idso, C. D., S. B. Idso, and R. C. Balling, The relationship between near-surface air temperature over land and the annual amplitude of the atmosphere's seasonal CO2 cycle, Environmental and Experimental Botany, 41(1), 31-37, 1999.

Jaagus, J., J. Truu, R. Ahas, and A. Aasa, Spatial and Temporal variability of climatic seasons on the East European Plain in relation to large-scale atmospheric circulation, Climate Research, 23, 111-129, 2003.

Jackson, R. B., J. Canadell, J. R. Ehleringer, H. A. Mooney, O. E. Sala, and E. D. Schulze, A global analysis of root distributions for terrestrial biomes, Oecologia, 108, 389-411, 1996.

Kaduk, J., and M. Heimann, A prognostic phenology scheme for global terrestrial carbon cycle models, Climate Research, 6(1), 1-19, 1996.

Kaduk, J. and M. Heimann, Assessing the Climate Sensitivity of the Global Terrestrial Carbon Cycle Model SILVAN, Physics and Chemistry of the Earth, 1997.

Keeling, C. D., T. P. Whorf, M. Wahlen, and J. Vanderplicht, Interannual extremes in the rate of rise of atmospheric carbon-dioxide since 1980, Nature, 375(6533), 666-670, 1995.

Keeling, C. D., J. F. S. Chin, and T. P. Whorf , Increased activity of northern vegetation inferred from atmospheric CO2 measurements, Nature, 382(6587), 146-149, 1996.

Keyser, A. R., J. S. Kimball, R. R. Nemani, and S. W. Running, Simulating the effects of climate change on the carbon balance of North American high-latitude forests, Global Change Biology, 6, 185-195, 2000.

Kramer, K., Selecting a model to predict the onset of growth of Fagus sylvatica, Journal of Applied Ecology, 31, 172-181, 1994.

Le Quéré, C., J. C. Orr, P. Monfray, O. Aumont, and G. Madec, Interannual variability of the ocean sink of CO2 from 1979 through 1997, Global Biogeochemical Cycles, 14(4), 1247-1265, 2000.

Lloyd, J., Current perspectives on the terrestrial carbon cycle, Tellus Series B: Chemical and Physical Meteorology, 51(2), 336-342, 1999.

Los, S. O., Linkages Between Global Vegetation and Climate: An Analysis Based on NOAA Advanced Very High Resolution Radiometer Data, Goddard Space Flight Center-1998-206852, 1998.

Los, S. O., G. J. Collatz, P. J. Sellers, C. M. Malmstrom, N. H. Pollack, R. S. DeFries, C. J. Tucker, L. Bounoua, M. T. Parris, and D. A. Dazlich, A global 9-year biophysical land surface dataset from NOAA AVHRR data, Journal of Hydrometeorology, 1(2), 183-199, 2000.

Los, S. O., G. J. Collatz, L. Bounoua, P. J. Sellers, and C. J. Tucker, Global Interannual Variations in Sea Surface Temperature and Land-Surface Vegetation, Air Temperature, and Precipitation, Journal of Climate, 14(7), 1535-1549, 2001.

Lucht, W., I. C. Prentice, R. B. Myneni, S. Sitch, P. Friedlingstein, W. Cramer, P. Bousquet, W. Buermann, and B. Smith, Climatic control of the high-latitude vegetation greening trend and Pinatubo effect, Science, 296(5573), 1687-1689, 2002.

McGuire, A. D., S. Sitch, J. S. Clein, R. Dargaville, G. Esser, J. Foley, M. Heimann, F. Foos, J. Kaplin, D. W. Kicklighter, R. A. Meier, J. M. Melillo, B. Moore III, I. C. Prentice, N. Ramankutty, T. Reichenau, A. Schloss, H. Tian, L. J. Williams, and U. Wittenburg, Carbon balance of the terrestrial biosphere in the twentieth century: Analyses of CO2 climate and land use effects with four process-based ecosystem models, Global Biogeochemical Cycles, 15(1), 183-206, 2001.

Menzel, A., Trends in phenological phases in Europe between 1951 and 1996, International Journal of Biometeorology, 44(2), 76-81, 2000.

Menzel, A., Plant phenological anomalies in Germany and their relation to air temperature and NAO, Climatic Change, 57(3), 243-263, 2003.

Menzel, A, and P. Fabian, Growing season extended in Europe, Nature, 397(6721), 659-659, 1999.

Murray, M. B., M. G. R. Cannell, and R. I. Smith, Date of budburst of fifteen tree species in Britain following climatic warming, Journal of Applied Ecology, 26, 693-700, 1989.

Myneni, R. B., Keeling, C. D., Tucker, C. J., Asrar, G., and Nemani, R. R., Increased plant growth in the northern high latitudes from 1981 to 1991, Nature, 386(6626), 698-702, 1997.

Nemani, R. M. White, P. Thornton, K. Nishida, S. Reddy, J. Jenkins, and S. Running, Recent trends in hydrologic balance have enhanced the terrestrial carbon sink in the United States, Geophysical Research Letters, 29(10), art. no. 1468, 2002.

Nikolov, N., and K. F. Zeller, Modeing coupled interactions of carbon, water, and ozone exchange between terrestrial ecosystems and the atmosphere I: Model description, Environmental Pollution, 124, 231-246, 2003.

Oleson, K. W.; Emery, W. J.; Maslanik, J. A., Evaluating land surface parameters in the Biosphere-Atmosphere Transfer Schems using remotely sensed data sets, Journal of Geophysical Research, 105(D6), 7275-7293, 2000.

Pacala, S. W., G. C. Hurtt, D. Baker, P. Peylin, R. A. Houghton, R. A. Birdsey, L. Heath, E. T. Sundquist, R. F. Stallard, P. Ciais, P. Moorcroft, J. P. Caspersen, E. Shevliakova, B. Moore, G. Kohlmaier, E. Holland, M. Gloor, M. E. Harmon, S. M. Fan, J. L. Sarmiento, C. L. Goodale, D. Schimel, and C. B. Field, Consistent land-and ocean-based U. S. carbon sink estimates, Science, 292, 2316-2320, 2001.

Potter, C. S., J. T. Randerson, C. B. Field, P. A. Matson, P. M. Vitousek, H. A. Mooney, and S. A. Klooster, Terrestrial ecosystem production: A process-oriented model based on global satellite and surface data, Global Biogeochemical Cycles, 7, 811-842, 1993.

Potter, C. S., S. Klooster, and V. Brooks, Interannual variability in terrestrial net primary production: Exploration of trends and controls on regional to global scales, Ecosystems, 2(1), 36-48, 1999.

Prince, S. D., S. N. Goward, S. Goetz, and K. Czajkowski, Interannual Atmosphere-Biosphere Variation: Implications for Observation and Modeling, Journal of Geophysical Research, 105(D15), 20,055-20,063, 2000.

Raich, J. W., and W. H. Schlesinger, The global carbon dioxide flux in soil respiration and its relationship to vegetation and climate, Tellus Series B: Chemical and Physical Meteorology, 44, 81-99, 1992.

Raich, J. W., E. B. Rastetter, J. M. Melillo, D. W. Kicklighter, P. A. Steudler, and B. J. Peterson, Potential Net Primary Prodution in South America: Application of a Global Model, Ecological Applications, 1(4), 399-429, 1991.

Randerson, J.T., M.V. Thompson, T.J. Conway, I.Y. Fung, and C.B. Field, The contribution of terrestrial sources and sinks to trends in the seasonal cycle of atmospheric carbon dioxide., Global Biogeochemical Cycles, 11, 535-560, 1997.

Randerson, J. T., Field, C. B., Fung, I. Y., and Tans, P. P., Increases in early season ecosystem uptake explain recent changes in the seasonal cycle of atmospheric CO2 at high northern latitudes, Geophysical Research Letters, 26(17), 2765-2768, 1999.

Rayner, P. J., and R. M. Law, The interannual variability of the global carbon cycle, Tellus Series B: Chemical and Physical Meteorology, 51(2), 210-212, 1999.

Reichenau, T. G., and G. Esser, Is interannual fluctuations of atmospheric CO2 dominated by combined effect of ENSO and volcanic aerosols, Global Biogeochemical Cycles, 17(4), 1094, doi: 10.1029/2002GB002025, 2003.

Robeson, S. M., Increasing growing-season length in Illinois during the 20th century, Climatic Change, 52(1-2), 219-238 , 2002.

Sarmiento, J. L., Atmospheric CO2 Stalled, Nature, 356, 697-698, 1993.

Schaefer, K., A. S. Denning, N. Suits, J. Kaduk, I. Baker, S. Los, and L. Prihodko, Effect of climate on interannual variability of terrestrial CO2 fluxes, Global Biogeochemical Cycles, 16(4), art. no. 1102, 2002.

Scheifinger, H., A. Menzel, E. Koch, C. Peter, and R. Ahas, Atmospheric mechanisms governing the spatial and temporal variability of phenological phases in central Europe, International Journal of Climatology, 11, 1739-1755, 2002.

Schwartz, M. D., AND B. E. Reiter, Changes in North American spring, International Journal of Climatology, 20(8), 929-932, 2000.

Sellers, P. J., C. J. Tucker, G. J. Collatz, S. O. Los, C. O. Justice, D. A. Dazlich, and D. A. Randall, A global 1° by 1° NDVI data set for climate studies, part II: The generation of global fields of terrestrial biophysical parameters from NDVI, International Journal of Remote Sensing, 15(17), 3519-3545, 1994.

Sellers, P. J., D. A. Randall, G. J. Collatz, J. A. Berry, C. B. Field, D. A. Dazlich, C. Zhang, G. D. Collelo, and L. Bounoua, A Revised Land Surface Parameterization of GCMs, Part I: Model Formulation, Journal of Climate, 9(4), 676-705, 1996.

Sellers, P. J., S. O. Los, C. J. Tucker, C. O. Justice, D. A. Dazlich, G. J. Collatz, and D. A. Randall, A Revised Land Surface Parameterization of GCMs, Part II: The Generation of Global Fields of Terrestrial Biophysical Parameters from Satellite Data, Journal of Climate, 9(4), 706-737, 1996.

Serreze, M. C., J. E. Walsh, F. S. Chapin, T. Osterkamp, M. Dyurgerov, V. Romanovsky, W. C. Oechel, J. Morison, T. Zhang, and R. G. Barry, Observational evidence of recent change in the northern high-latitude environment, Climatic Change, 46(1-2), 159-207, 2000.

Shabanov, N. V., L. M. Zhou, Y. Knyazikhin, R. B. Myneni, and C. J. Tucker, Analysis of interannual changes in northern vegetation activity observed in AVHRR data from 1981 to 1994, IEEE Transactions on Geoscience and Remote Sensing, 40(1), 115-130, 2002.

Shindell, D. T., R. L. Miller, G. A. Schmidt, and L. Pandolfo, Simulation of recent northern winter climate trends by greenhouse-gas forcing, Nature, 399(6735), 452-455, 1999.

Slayback, D. A., J. E. Pinzon, S. O. Los, and C. J. Tucker, Northern hemisphere photosynthetic trends 1982-99, Global Change Biology, 9(1), 1-15, 2003.

Stone, R. S., E. G. Dutton, J. M. Harris, and D. Longenecker, Earlier spring snowmelt in northern Alaska as an indicator of climate change, Journal of Geophysical Research: Atmospheres, 107(D10), art. no. 4089, 2002.

Tanja, S., F. Berninger, T. Vesala, T. Markkanen, P. Hari, A. Makela, H. Ilvesniemi, H. Hanninen, E. Nikinmaa, T. Huttula, T. Laurila, M. Aurela, A. Grelle, A. Lindroth, A. Arneth, O. Shibistova, and J. Lloyd, Air temperature triggers the recovery of evergreen boreal forest photosynthesis in spring, Global Change Biology, 9(10), 1410-1426, 2003.

Tans, P. P. and D. W. R. Wallace, Carbon Cycle Research After Kyoto, Tellus Series B: Chemical and Physical Meteorology, 51, 562-571, 1999.

Thompson, D. W. J. and J. M. Wallace, Annular Modes in the Extratropical Circulation. Part I: Month-to-Month Variability, Journal of Climate, 13, 1000-1016, 2000.

Thompson, D. W. J. and J. M. Wallace, Regional Climate Impacts of the Northern Hemisphere Annular Mode, Science, 293, 85-89, 2001.

Thompson, D. W. J., J. M. Wallace, and G. Hegerl, Annular Modes in the Extratropical Circulation. Part II: trends, Journal of Climate, 13, 1018-1036, 2000.

Tian, H. J. M. Melillo, D. W., Kicklighter, A. D. McGuire, J. V. K. Helfrich III, B. Moore, III, and C. J. Vorosmarty, Effect of interannual climate variability on carbon storage in Amazonian ecosystems, Nature, 396, 664-667, 1998.

Trolier, M., W. C. White, P. P. Tans, K. A. Masarie, and P. A. Gemery, Monitoring the Isotopic Composition of Atmnospheric CO2: Measurements from the NOAA Global Air Sampling Network, Journal of Geophysical Research, 101(D20), 25,897-25,916, 1996.

Tucker, C. J., D. A. Slayback, J.E. Pinzon, S. O. Los, R. B. Myneni, and M. G. Taylor, Higher northern latitude normalized difference vegetation index and growing season trends from 1982 to 199, International Journal of Biometeorology, 45(4), 184-190, 2001.

Vaganov, E. A., M. K. Hughes, A. V. Kirdyanov, F. H. Schweingruber, and P. P. Silkin, Influence of snowfall and melt timing on tree growth in subarctic Eurasia, Nature, 400(6740), 149-151, 1999.

White, M. A., P. E. Thornton, and S. W. Running, A continental phenology model for monitoring vegetation responses to interannual climatic variability, Global Biogeochemical Cycles, 11(2), 217-234, 1997.

White, M. A., S. W. Running, and P. E. Thornton, The impact of growing season length variability on carbon assimilation and evapotranspiration over 88 years in the eastern US deciduous forest, International Journal of Biometeorology, 42, 139-145, 1999.

Wu, W.L., and A. H. Lynch, Response of the seasonal carbon cycle in high latitudes to climate anomalies, Journal of Geophysical Research: Atmospheres, 105(D18), 22897-22908, 2000.

Zhou, L. M., C. J. Tucker, R. K. Kaufmann, D. Slayback, N. V. Shabanov, and R. B. Myneni, Variations in northern vegetation activity inferred from satellite data of vegetation index during 1981 to 1999, Journal of Geophysical Research: Atmospheres, 106(D17), 20,069-20,083, 2001.

Zhou, L., R. K. Kaufmann, Y. Tian, R. B. Myneni, and C. J. Tucker, Relation between interannual variations in satellite measures of northern forest greenness and climate between 1982 and 1999, Journal of Geophysical Research: Atmospheres, 108(D1), art. no. 4004, 2003.

Zimov, S. A., S. P. Davidov, Y. V. Voropaev, S. F. Prosiannikov, I. P. Semiletov, M. G. Chapin, and F. S. Chapin, Siberian CO2 efflux in winter as a CO2 source and cause of seasonality in atmospheric CO2, Climatic Change, 33(1), 111-120, 1996.

Zimov, S. A., S. P. Davidov, G. M. Zimova, A. I. Davidova, F. S. Chapin, M. C. Chapin, and J. F. Reynolds, Contribution of disturbance to increasing seasonal amplitude of atmospheric CO2, Science, 284(5422), 1973-1976, 1999.